

NORTHWESTERN UNIVERSITY

Towards a Quantitative and Objective Assessment of Renal Oxygenation  
Through Magnetic Resonance Imaging

A DISSERTATION

SUBMITTED TO THE GRADUATE SCHOOL  
IN PARTIAL FULFILLMENT OF THE REQUIREMENTS

for the degree

DOCTOR OF PHILOSOPHY

Field of Biomedical Engineering

By

Jon Thacker

EVANSTON, ILLINOIS

December 2016

## ABSTRACT

Towards a Quantitative and Objective Assessment of Renal Oxygenation Through  
Magnetic Resonance Imaging

Jon Thacker

Even though renal blood flow accounts for nearly a quarter of cardiac output, the renal medulla operates in an environment with a scant supply of oxygen. The reason for this apparent discrepancy is thought to be threefold. Blood flow to the outer medulla is less than 50% of that received by the cortex. Secondly, countercurrent shunting of oxygen occurs between the arterial and venous system in the vasa recta, significantly reducing the amount of delivered oxygen. Lastly, oxygen consumption is quite high in this region, primarily due to sodium reabsorption in the medullary thick ascending limbs. Active tubular transport processes account for around 80% of renal oxygen consumption and are highly sodium load-dependent. Operating in this environment subjects the renal medulla to an increased risk of hypoxic damage, making it particularly sensitive to intermittent periods of hypoperfusion or hemodilution.

Renal hypoxia has been implicated in acute kidney injury and in the initiation and progression of chronic kidney disease. Starting targeted treatment early can slow disease

progression, reduce complications and improve quality of life. Understanding renal oxygenation may be critical in understanding the progression of chronic kidney disease as well.

Magnetic Resonance Imaging (MRI) sequences based on the blood oxygen level-dependent (BOLD) contrast mechanism have previously been used for following changes in renal oxygenation. However, these measurements are sensitive to other confounding factors in addition to oxygenation. Additionally, renal BOLD MRI studies are prone to bias due to inherent difficulties in segmenting renal tissue. There is a need for an objective, quantitative, and non-invasive measure of renal oxygenation.

In this work, methods to increase the clinical utility of BOLD MRI in assessing renal oxygenation are investigated. We explore the use of BOLD MRI data from the entire parenchyma to reduce the subjectivity in analyzing renal BOLD MR images. To remove the extra confounding factors influencing BOLD MRI changes, a statistical model is presented that provides an estimate of  $PO_2$  derived from BOLD MRI data. An invasive method for refining and calibrating the model is investigated that has the ability to independently measure blood and tissue  $PO_2$ . Finally an alternative technique for acquiring BOLD MRI data that is not influenced by a subject's hydration level is presented.

These findings provide methods that can estimate renal oxygenation, while controlling confounding factors, along with an objective analysis of the parametric maps, and may provide for widespread utility in pre-clinical and clinical settings.

## Acknowledgements

This is the work of many people and it certainly would not have been possible without their support and contributions. I would like to thank my advisor, Pottumarthi Prasad for his guidance and support. I thank him for his insights and for guiding me through academia. I am grateful to have worked with him and the rest of the lab members, past and present. I am especially thankful to Huan Tan, Lu-ping Li, Tammy Franklin, Ioannis Koktzoglou, Shivraman Giri and Wei Lei. I am also thankful for my thesis committee members Robert Linsenmeier, Timothy Carroll and Todd Parrish. I am also very grateful for the efforts of Lilach Lerman and David Wilson in supporting my grant proposal. To Mahnaz Shahidi, Anthony Felder and Tara Nguyen, thank you for your collaboration, lab space, and for making it through the bureaucratic nightmare that is dealing with three separate IACUC committees.

I dedicate this work to my family members. Thank you for your encouragement throughout the years. None of this would have been possible without you.

## Table of Contents

ABSTRACT	2
Acknowledgements	4
List of Tables	9
List of Figures	11
Chapter 1. Introduction	17
1.1. Organization	20
Chapter 2. Background	21
2.1. Renal Anatomy and Physiology	25
2.2. Magnetic Resonance Imaging	30
2.2.1. Nuclear Magnetic Resonance	31
2.2.2. Free induction decay	33
2.2.3. Relaxation	34
2.2.4. T2* decay	35
2.2.5. Blood Oxygenation-Level Dependent (BOLD) MRI	36
2.2.6. Spin echoes	36
2.2.7. Imaging	37
2.2.8. K-space	38

	6
2.2.9. Imaging sequences	39
2.2.10. Echo planar imaging (EPI)	42
2.2.11. Gradient recalled echo (GRE) sequence	42
2.3. Phosphorescence Lifetime Imaging	43
Chapter 3. Objective Analysis of the Renal Parenchyma BOLD MRI Data	45
3.1. Introduction	45
3.2. Materials and Methods	47
3.2.1. Subjects	47
3.2.2. MRI Protocol	48
3.2.3. R2* Maps	48
3.2.4. Regions of Interest	49
3.2.5. Moment Analysis	49
3.2.6. Statistical Analysis	51
3.3. Results	52
3.3.1. Comparison of Mean Values	52
3.3.2. Moment Analysis	55
3.4. Discussion	56
3.4.1. Comparison of Mean Values	56
3.4.2. Physiological Interpretation	58
3.4.3. Multiple Moment Analysis	60
3.4.4. Limitations	60
3.5. Conclusion	61

Chapter 4. Physiologically Relevant Parameters: BOLD Derived Renal PO <sub>2</sub>	63
4.1. Introduction	63
4.2. Methods	65
4.2.1. Animals	65
4.2.2. MRI	65
4.2.3. Analysis	67
4.2.4. Statistical Analysis	68
4.3. Results	69
4.4. Discussion	70
4.4.1. Limitations	74
4.5. Conclusion	75
Chapter 5. Invasive Renal Cortical PO <sub>2</sub>	76
5.1. Introduction	76
5.2. Methods	77
5.2.1. Animals	77
5.2.2. Phosphorescence Lifetime Imaging	78
5.2.3. Statistics	79
5.3. Results	79
5.4. Discussion	79
5.4.1. Comparison to BOLD PO <sub>2</sub>	80
Chapter 6. Direct Assessment: R2' Renal Mapping	84
6.1. Introduction	84

	8
6.2. Methods	86
6.3. Discussion	88
6.4. Conclusions	91
Chapter 7. Arterial Spin Labeling Perfusion Sensitivity to Pharmacologically Induced Perfusion Changes	93
7.1. Introduction	93
7.2. Methods	94
7.2.1. Animal Preparation	94
7.2.2. Pharmacological Agents	95
7.2.3. Perfusion Study Design	95
7.2.4. Imaging Protocol and Perfusion Quantification	96
7.2.5. Data Analysis	97
7.3. Results	98
7.4. Discussion	99
7.5. Conclusion	103
Chapter 8. Conclusions	104
References	108

## List of Tables

3.1	Intra-class correlation coefficients for mean values of each region at baseline	53
3.2	Controls Baseline vs. Post-furosemide R2*. † Wilcoxon signed rank test statistic. ‡ Cohen's d measure of effect size	54
3.3	CKD Baseline vs. Post-furosemide R2*. † Wilcoxon signed rank test statistic. ‡ Cohen's d measure of effect size	54
3.4	Control vs. CKD at baseline. § Mann-Whitney U test statistic. ‡ Cohen's d measure of effect size	54
3.5	Control vs. CKD post furosemide. § Mann-Whitney U test statistic. ‡ Cohen's d measure of effect size	55
3.6	Higher parenchyma moments: Controls Baseline vs. Post-furosemide. † Wilcoxon signed rank test statistic. ‡ Cohen's d measure of effect size	56
3.7	Higher parenchyma moments: CKD Baseline vs. Post-furosemide. † Wilcoxon signed rank test statistic. ‡ Cohen's d measure of effect size	56
3.8	Higher parenchyma moments: Baseline Controls vs. CKD. § Mann-Whitney U test statistic. ‡ Cohen's d measure of effect size	57
3.9	Higher parenchyma moments: Post-Furosemide Controls vs. CKD. § Mann-Whitney U test statistic. ‡ Cohen's d measure of effect size	57

3.10	Intra-class correlation coefficients for each of the parenchyma moments.	57
------	--	----

## List of Figures

- 2.1 Urine wheel describing the possible colors, smells and tastes of urine and their corresponding disease diagnosis. Reproduced from *Epiphaniae Medicorum* by Ullrich Pinder in 1506. 23
- 2.2 Bowman's depiction of human nephron and supporting vasculature. Reproduced from [10]. 25
- 2.3 Diagram of a human kidney showing the main anatomic regions. This is a multilobar kidney. Rats and other mammals have unilobar kidneys, which are essentially a single pyramid from a multilobar kidney. 26
- 2.4 Diagram of a nephron and supporting vasculature. 28
- 2.5 Spin vector precession around the magnetic field axis.  $\omega$  is the Larmor frequency 32
- 2.6 An example sketch of a free induction decay. Magnetization is picked up in a nearby coil, oscillating at the Larmor frequency. The signal gradually decays as spins leave the excited state. 34
- 2.7 Sketch of free induction decay with T2 and T2\* relaxation. 35
- 2.8 Schematic of the connection between the BOLD signal and tissue PO<sub>2</sub>. Changes in SHb will lead to changes in the magnetic susceptibility

of blood. Blood  $PO_2$  will increase as SHb increases by the oxygen-hemoglobin dissociation curve. Blood  $PO_2$  diffuses into tissue. The standard assumption of BOLD is that tissue  $PO_2$  is roughly in equilibrium with venous capillary  $PO_2$ .

37

2.9 Layout of a typical 2D imaging experiment. The top figure shows a rectangular sample placed in a static magnetic field ( $B_0$ ). Next, the slice selection step is shown; only the region designated by the dashed line is excited by the RF pulse. The final figure shows the directions of phase encoding (PE) and frequency encoding (FE) that are used to create an image.

41

2.10 Example diagram of an Echo Planar Imaging (EPI) pulse sequence. The key novelty of the EPI sequence is its speed. By moving in a zig-zag pattern across k-space, the EPI sequence can read out an entire image in a single echo. This sequence can be modified to spin echo sequence by adding a  $180^\circ$  pulse.

42

2.11 Example diagram of a Gradient Recalled Echo (GRE) pulse sequence. This is the main sequence used for creating  $R2^*$  images.

43

3.1 An example of the variation seen in the mean  $R2^*$  depending on ROI placement. The left column shows a representative control subject and the right a CKD subject. The first echo from the mGRE images is used as an anatomical template for placing ROIs. The image appears a bit blurry as it is interpolated to this larger size for viewing purposes.

The ROI is then used to find the mean of the corresponding region on the calculated  $R2^*$  map. Three different ROIs are placed for each region (large cortical and parenchyma ROIs are difficult to see due to the overlap of each region). The mean and standard deviations of each region are shown in the plots. Variation between the ROIs is quite large in the small regions, while the larger ones are clearly not as susceptible to differences in exact placement.

50

- 3.2 Mean-difference (Bland-Altman) plots depicting the inter-rater agreement for each ROI region. The medulla shows the highest variation while the parenchyma shows the lowest. Additionally, the large cortex shows a lower level of variation than the small cortex does. 53
- 3.3 Example kernel density plots of typical cases for each of the comparisons performed in tables 3.2 to 3.10. A kernel density plot is used to estimate the empirical distribution and is not sensitive to the bin size like a histogram would be. A kernel density estimate with Gaussian kernels and automatic bandwidth calculation was used to estimate the continuous probability distribution. 55
- 4.1 MRI protocol. The MRI data acquisition was performed in three stages: baseline, LNAME and furosemide. Each MRI stage consisted of three repetitions of alternating mGRE and SE acquisitions. 66
- 4.2 Monte Carlo simulation results in cortex and outer medulla. (a) Plot shows the relationship between a measured  $R2'$  and the expected

hemoglobin saturation (SHb). (b) Plot showing the relationship between SHb and blood  $PO_2$ . See the methods section for a list of parameters used in the model. 68

4.3 Box-whisker plots for R2 (a), R2\* (b), SHb (c), and blood  $PO_2$  (d). The two regions assessed are shown (cortex and outer medulla (OM)). Each region shows three time points at which MRI was assessed: baseline, post-LNAME, post-furosemide. 69

4.4 (a) shows R2 and R2\* maps at each stage in a representative animal. (b) is the summary of cortical and outer medullary  $PO_2$  estimates from all animals at all individual time points for each stage. Typical ROIs are illustrated in (b) as well. 71

4.5 The relative values of R2, R2\* and blood  $PO_2$  between each region are illustrated here. At baseline, the mean and standard deviations of are shown for each region for R2\* and blood  $PO_2$  measurements. The relative R2\* values are hard to interpret because the low R2\* in the inner medulla would indicate higher blood oxygenation. However, it is well known that inner medulla has the least  $PO_2$  [65]. Using the same parameters as the outer medulla, the estimated  $PO_2$  appears to be closer to the outer medulla. The conversion to  $PO_2$  also facilitates identifying regions that are hypoxic, e.g. compared to systemic venous  $PO_2$ . 72

- 5.1 Example phosphorescence lifetime image. Each pixel shows the local  $\text{PO}_2$  (mmHg). The center red circle shows the region of interest used in the study. 80
- 5.2 Summary plots from this study and the previous BOLD  $\text{PO}_2$  model study. 81
- 5.3 Example of how not factoring in the blood volume change into the model could lead it to misrepresent the actual change taking place. 81
- 6.1 Example navigator gated profile. The dark region is the lung and the bright region is the liver. Yellow boxes indicate the windows of acquisition. 87
- 6.2 Example ASE echo images. (A)  $\tau = 0$  ms, (B)  $\tau = 15$  ms, (C)  $\tau = 21$  ms, (D)  $\tau = 27$  ms. 89
- 6.3 Representative  $R2'$  map for segmented and single-shot EPI readouts. (A) Single shot,  $\tau = 15$  ms (B) Single shot,  $R2'$  map (C) Segmented,  $\tau = 15$  ms, (D) Segmented,  $R2'$  map. 90
- 6.4 Example  $R2'$  decay curves for a subject at baseline and after furosemide administration. 91
- 7.1 Experimental design. Baseline and vasodilation scans were repeated to assess reproducibility. The vasoconstriction scans were repeated to study the cumulative effects of L-NAME. 96

- 7.2 Representative renal blood flow maps of rat kidneys at each experimental condition. Note the increased cortical perfusion with adenosine infusion and the decreased cortical perfusion with L-NAME injection 99
- 7.3 Comparisons of quantitative perfusion rates. Note the return to baseline perfusion values when the infusion of Adenosine was stopped. The increase in perfusion is comparable after each dose, and is statistically significant compared to the baseline. On the other hand, administration of L-NAME results in significant reduction in perfusion compared to baseline. Following the second administration, there is further significant reduction in perfusion. No significance difference was observed between the two baseline, as well as Adenosine scans. \* indicates significant difference ( $p < 0.05$ ) comparing to the corresponding baseline scans. + indicates significant difference ( $p < 0.05$ ) comparing to the first L-NAME scan 100

## CHAPTER 1

### **Introduction**

Even though renal blood flow accounts for nearly a quarter of cardiac output, the renal medulla operates on the verge of hypoxia. The reason for this apparent discrepancy is thought to be threefold. Blood flow to the outer medulla is less than 50% of that received by the cortex. Secondly, countercurrent shunting of oxygen occurs between the arterial and venous system in the vasa recta, significantly reducing the amount of delivered oxygen. Lastly, oxygen consumption ( $V_{O_2}$ ) is quite high in this region, primarily due to sodium reabsorption in the medullary thick ascending limbs. Active tubular transport processes account for around 80% of renal  $V_{O_2}$  and are highly sodium load dependent. It has been shown that the renal extraction of oxygen actually remains stable over a wide range of blood flow rates due to the blood flow dependence of renal  $V_{O_2}$ . Thus, unlike other organs, where increased blood flow improves oxygenation, an increase in renal blood flow may result in an increased renal  $V_{O_2}$  and no change in renal oxygenation. Operating in this environment subjects the renal medulla to an increased risk of hypoxic damage, making it particularly sensitive to intermittent periods of hypoperfusion or hemodilution [85].

Medullary hypoxia is known to be associated with the development of acute kidney injury (AKI) [85] and the pathophysiology of chronic kidney disease (CKD) [27, 39]. Hypertension, diabetic nephropathy, and contrast-induced AKI have also been associated with renal hypoxia [15, 23, 36, 38]. Assessing a patient's renal health early and having the opportunity to start targeted treatment can slow disease progression, reduce complications

from decreased GFR, and improve quality of life [39,51]. With eleven percent of adults in the United States aged 20 years or older stricken by CKD [52]. Mortality rates from AKI upwards of 50% for critically ill patients [6]. Understanding these disease states should be a public health priority. Our long-term goals are to establish techniques for assessing renal parenchymal oxygenation, and utilize these techniques for guiding treatment and monitoring disease progression.

Regional differences in oxygen consumption and supply within the kidney make an imaging technique very useful for assessing parenchyma tissue oxygenation. Blood oxygen level-dependent (BOLD) MRI is currently the only non-invasive method for assessing renal oxygenation; both in humans and preclinical models [112]. Generally, this has been achieved through the established method of  $R2^*$  relaxation measured with a gradient echo (GRE) sequence [79,81]. BOLD MRI has been used successfully as a non-invasive technique for assessing changes in renal oxygenation in preclinical models, healthy human subjects, and patient populations. Blood oxygenation has been shown to be a useful surrogate to assess renal tissue oxygenation. The technique has been validated across several vendor platforms and in laboratories throughout the world [19,21,35,40,45]. While efficacious,  $R2^*$  measurements cannot be directly translated into  $PO_2$  because of several confounding factors [110]. While this method has been demonstrated to be effective for monitoring changes in intrarenal oxygenation, a method for direct quantitative estimation of renal oxygenation remains as an unmet need.

$R2^*$  can be considered to be made of two components:  $R2$  and  $R2'$ .  $R2'$  is the component that is specific to changes in magnetic susceptibility associated with deoxygenated

hemoglobin. A brute force method of measuring  $R2'$  is to acquire a gradient echo sequence with multiple echo times to calculate  $R2^*$  and similarly a spin echo sequence with multiple echo times to calculate  $R2$ . Alternatively,  $R2'$  can be determined directly with an asymmetric spin echo (ASE) sequence. There are several alternative BOLD based contrast techniques; models have shown  $R2'$  to be one of the most promising methods for estimating blood  $PO_2$ .

In addition to  $R2'$ , an ASE acquisition can be used to provide an estimate of the oxygen saturation of hemoglobin (SHb) and venous blood volume. While BOLD measurements are several steps removed from actual tissue  $PO_2$ , moving from  $R2'$  to SHb is one step closer to the physiological parameters we are trying to assess in patients.

While  $R2'$  can provide an estimate of the blood  $PO_2$ , it does not provide enough information to determine the tissue  $PO_2$ . One of the key parameters to measure is regional perfusion. The medulla is known to be sensitive to hypoperfusion events. It is possible to use perfusion in a model of tissue  $PO_2$ ; but it still provides key insights into the organ's oxygenation status as an independent measure.

Renal BOLD MR images are currently assessed with a manual segmentation of the cortical and medullary regions. This method is difficult if the contrast between the regions has been significantly reduced following drug administration or in certain disease states. Assessment of BOLD images needs to be less prone to user bias, which will increase its acceptance and translation to the clinic.

We hypothesize that a set of alternative BOLD parameters that are more directly related to blood  $PO_2$ , combined with these analysis techniques, are necessary for improved acceptance of a quantitative and non-invasive measure of renal blood  $PO_2$ . With the

recent availability of phosphorimetry based measurements that can independently probe blood and tissue  $\text{PO}_2$ , a unique opportunity exists to validate the agreement between these measures and BOLD MRI derived parameters.

### 1.1. Organization

Following the Introduction, Chapter 2 describes the background of renal physiology and MRI analysis. Chapter 3 presents a technique for analyzing renal MRI data, using the entire renal parenchyma, resulting in increased objectivity in measurements. Chapter 4 looks at using a statistical model for converting BOLD MRI parameters to  $\text{PO}_2$ . In Chapter 5 a preliminary study looks at the feasibility of using phosphorimetry to validate the statistical model from Chapter 4. The model used in Chapter 4 derives the MRI parameter from two separate scans. In Chapter 6, a method for measuring the MRI parameter of interest in a single scan is examined. This technique also provides an estimate of the blood volume, another key parameter in the statistical model. Chapter 7 examines the feasibility of estimating perfusion from ASL parameters which could play a key role in estimating tissue  $\text{PO}_2$  from blood  $\text{PO}_2$ .

## CHAPTER 2

### **Background**

Despite being known as the “Father of Modern Medicine”, Hippocrates (460-355 BCE) began his work by systematizing the practice of humorism, an ancient and demonstrably false view of disease. However, his approach was remarkable for the time and he is credited with being the first person to believe that disease was caused by natural causes and not from metaphysical forces. Humorism gave a physical explanation for the primary causes of disease, and held as the predominant theory in western medicine until the 16<sup>th</sup> century. Humorism maintains that an excess or deficiency of any of the four primary bodily fluids (blood, phlegm, yellow bile and black bile) will affect a person’s temperament and health. The role of the physician is thus to rebalance the humors after a disruption, restoring health and curing disease. Hippocrates believed urine to be a filtrate of the four humors, and he placed much emphasis on its role in diagnosing diseases. While the theory has been proven false, some of his conclusions were quite prescient, despite the underlying theory.

In Hippocrates’ text, *Aphorisms*, he declared that bubbles found on the surface of fresh urine were an indicator of kidney disease. In fact, these bubbles are often due to proteinuria and can certainly indicate kidney disease or at least a urinary tract infection [3]. He also described blood in the urine as an indicator of ulceration in the kidney or bladder, which indeed is one possible etiology. Hippocrates described many other associations between the quality of urine, diseases, and their prognosis.

Galen of Pergamon began his study of medicine (129-200 CE) in an era when the system of humorism had already become well established. Galen created the first notion of systematic human physiology, which essentially held as dogma for one and one-half thousand years [25]. Primarily through vivisection and ligating various segments of the renal anatomy, Galen discovered that the primary function of the kidneys was to filter blood. Although his description was limited to the separation of the “thin” from the “thick” components of blood [26], it was still a significant departure from the humorist belief. Galen also observed that the amount of urine excreted should be equal to the amount of liquid ingested in a healthy person. We now know that a decrease in urine output can indeed be an indication of dehydration or kidney failure. Galen hypothesized and demonstrated that urine was not a filtrate of the four humors, but just that of the blood.

Galen and Hippocrates both practiced uroscopy, or the process of examining urine for symptoms of disease. Urine had long provided a glimpse into the health of a patient. Ancient doctors observed that ants were attracted to the urine of diabetics and noted its sweet taste. In the second century, Aretus, who coined the term diabetes, or “siphon”, described the disease as “a melting down of flesh and limb into the urine” [3]. The characteristic sweetness would be incorporated by Thomas Willis when he appended mellitus, meaning “of honey”, to the disease name. Uroscopy established itself as the leading diagnostic tool throughout the Middle Ages. Special holding flasks were designed for examining urine, known as matulas. Particular emphasis was placed on their shape which conformed to the geometry of the body’s own holding vessel, the bladder. The complexity of the uroscopic exam increased and simplified charts were designed to aid in

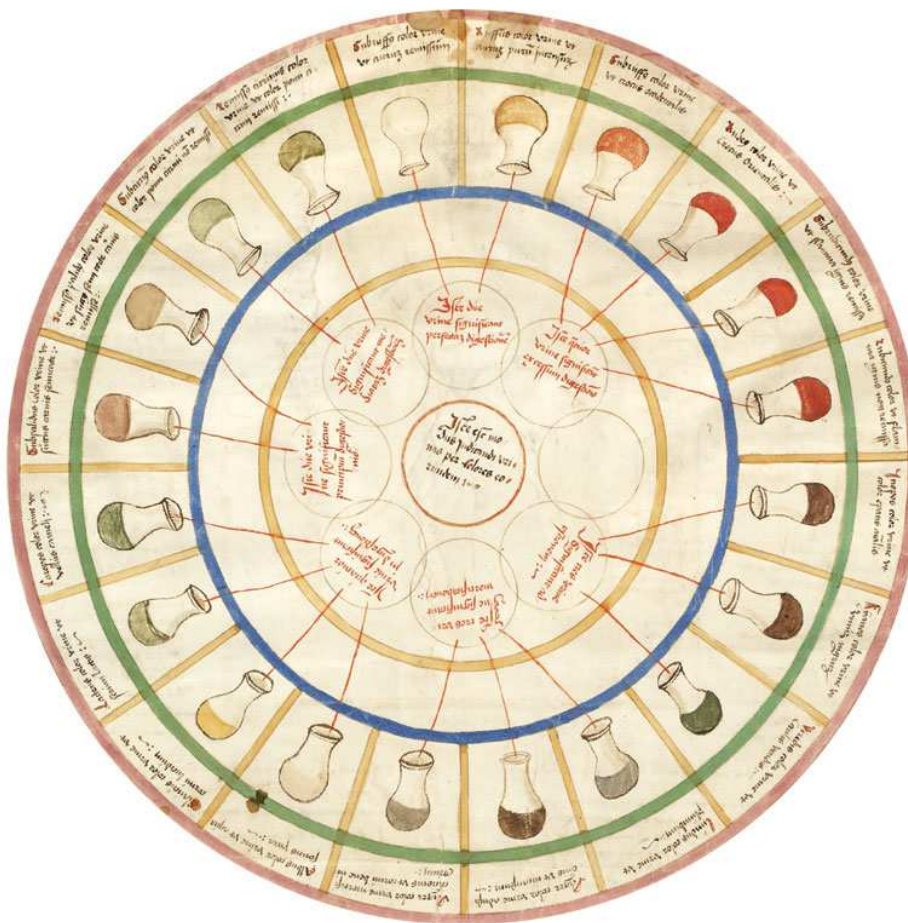


Figure 2.1. Urine wheel describing the possible colors, smells and tastes of urine and their corresponding disease diagnosis. Reproduced from *Epiphanie Medicorum* by Ullrich Pinder in 1506.

diagnosis (fig. 2.1). In uroscopy, physicians had established the first laboratory test and could accurately diagnose a subset of diseases. The matula was no longer just a tool, but also a distinguishing symbol of physicians, similar to the way stethoscopes are seen today [3].

As the emphasis on the diagnostic power of uroscopy grew, the importance on physically examining the patient began to wane—physicians started diagnosing solely based

on urine. Texts previously only available in Latin were translated and circulated outside of the University, opening the uroscopy market to amateurs. By the 17<sup>th</sup> century, the ascribed power of uroscopy had reached an absurd level. Fortune tellers and prophets claimed to be able to glimpse into the patient's future by gazing into the matula, a practice known as "uromancy". Uroscopy had swung far afield from the original diagnoses discovered by Hippocrates. Soon it received a strong backlash from the scientifically grounded side of the medical community. Following the publication of the satirical take on uroscopy by Thomas Brian in 1637, *The Pisse Prophet*, the practice began to fall out of favor. Physicians still using matulas were ridiculed, they were dubbed "Pisse Prophets".

Beyond the essential functionality described by Galen, insight into the inner workings of kidneys remained mostly stagnant for a millennium. As uroscopy was imploding, new studies were beginning to look into renal anatomy and physiology. The two major regions of the kidney, the cortex and the medulla, were identified by Nathaniel Highmore (1613-1684). The medulla was described as containing fibers directed toward the pelvis, while the cortex was free of fibers. Marcello Malpighi (1628-1694) used the recently invented microscope to describe the renal corpuscles, discovering the interface between the vascular system and urinary output. However, it was not until William Bowman's (1812-1891) publications that a complete picture of the vascular-renal interface was established. Bowman showed the inner workings of these corpuscles were the vascular glomeruli. He also described the origin of efferent arterioles and the tubular loop, literally providing the first clear and comprehensive picture of a complete nephron (see fig. 2.2). Further research was necessary to establish the physiology on a cellular level but the key groundwork had been laid.

*16 Plan - Proportions  
as in Man.*

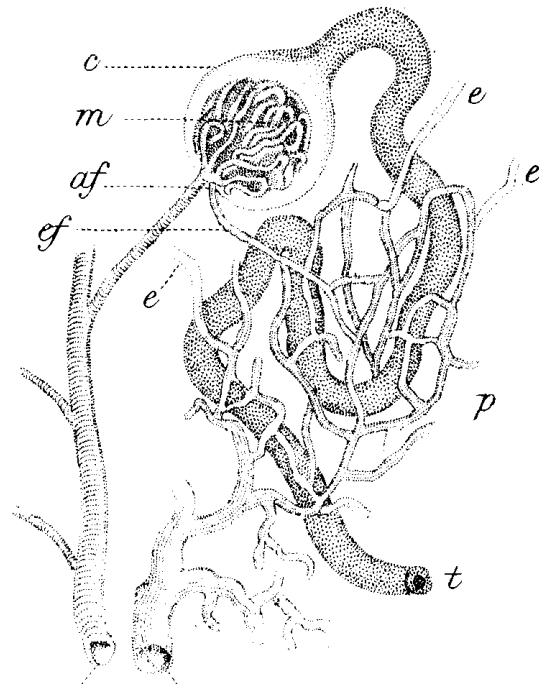


Figure 2.2. Bowman's depiction of human nephron and supporting vasculature. Reproduced from [10].

### 2.1. Renal Anatomy and Physiology

Kidneys are responsible for maintaining fluid and solute homeostasis through a wide range of environmental conditions. They must balance blood pH, water, sodium, and nitrogen while removing the waste products of metabolism. This process plays a key role in establishing arterial blood pressure and provides a physiological basis for the correlation between properly functioning kidneys and cardiovascular health.

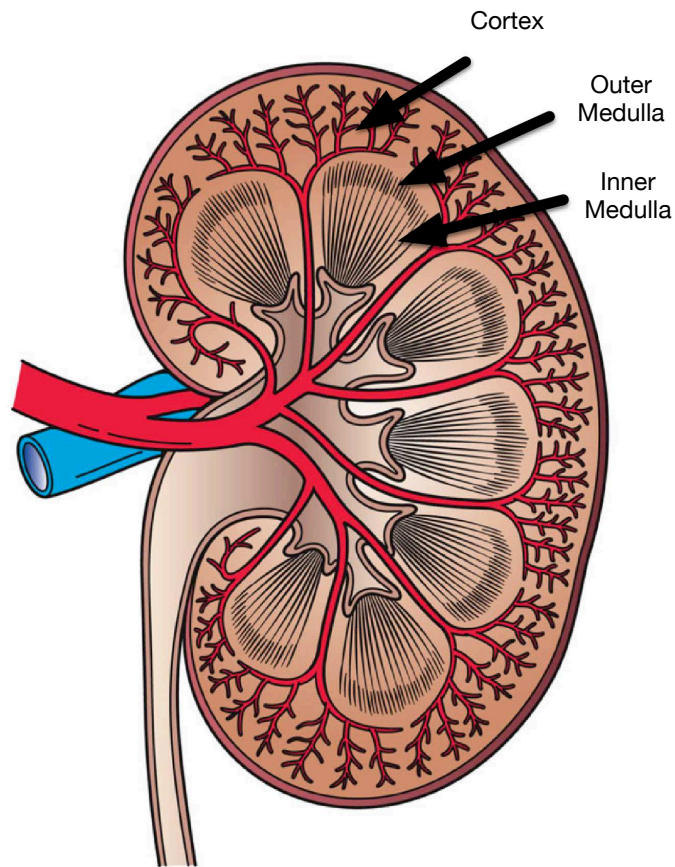


Figure 2.3. Diagram of a human kidney showing the main anatomic regions. This is a multilobar kidney. Rats and other mammals have unilobar kidneys, which are essentially a single pyramid from a multilobar kidney.

The mammalian kidney can be viewed as a series of concentric layers, with blood flowing into the outer layers and the waste products (urine) funneling towards the center before finally exiting at the renal pelvis. Figure 2.3 shows the primary anatomical

structures with three distinct regions: the cortex, the outer medulla (OM), and the inner medulla (IM). The major functional unit of the kidney is the nephron, shown previously in fig. 2.2 and schematically in fig. 2.4. Nephrons are extremely small with radii of approximately  $10\ \mu\text{m}$ , but they are very numerous; human kidneys contain approximately 1 million nephrons. Arterial blood enters Bowman's capsule as a glomerulus in the cortical region of the kidney. Small molecules in the blood—water, glucose, sodium chloride, amino acids and urea—pass freely into Bowman's space. The rate at which water filters into the nephron is expressed as the glomerular filtration rate, or GFR. GFR is determined by the difference in hydrostatic and oncotic pressure gradients between the glomerular capillaries and Bowman's capsule. This pressure difference is calculated through the Starling equation. Oncotic pressure resists hydrostatic pressure because large proteins, such as albumin, cannot pass through the endothelial walls of the glomerulus, drawing water back into the capillaries. Net GFR in a healthy human, across all nephrons, is about 125 ml/min or 180 L/day. Since the body contains only about 42 L of body fluid, the kidney must perform further processing of the filtrate to prevent loss of all fluids in less than a day.

Following filtration, nephrons begin to refine the filtrate through two means: secretion and reabsorption. The final output of the filtrate is excreted into the ureters which drain into the bladder. Urinary excretion amounts to around 1 ml/min or 1.5 L/day. This is considerably less than the 180 L/day of filtrate input to the nephron. Filtration is a passive process. To reclaim the essential sodium and glucose molecules lost during filtration, the proximal tubule of a nephron will actively reabsorb them. Reabsorption can expend a significant amount of energy. An active process is required because the ions are being

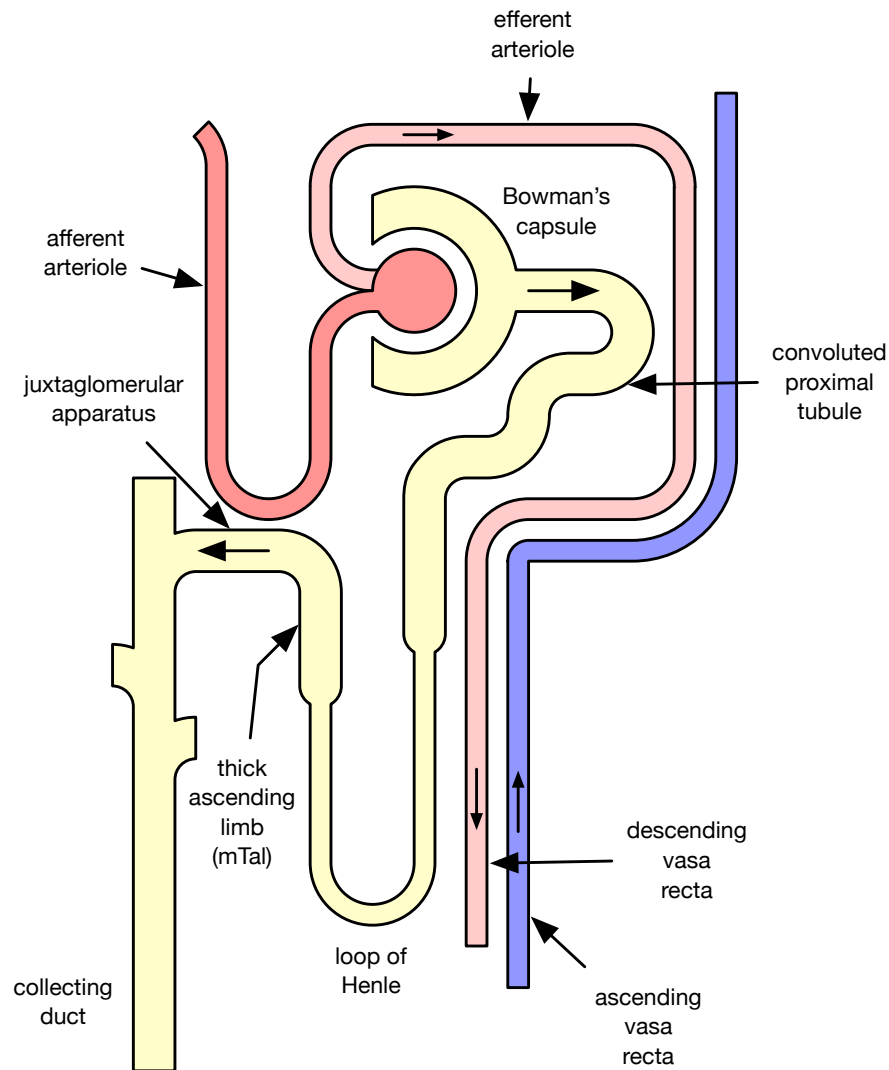


Figure 2.4. Diagram of a nephron and supporting vasculature.

pumped against their concentration gradients. Water must be reabsorbed as well, but no extra energy is required as the water molecules follow the solute concentration gradient. The convoluted proximal tubule is the main site of sodium reabsorption; however the medullary thick ascending limb (mTAL) plays a key role as well fig. 2.4. This process is targeted by pharmacological agents known as loop diuretics.

Furosemide is a highly potent loop diuretic which binds to the sodium-potassium-chloride cotransporter, present in the mTAL. This results in excretion of sodium chloride, potassium, hydrogen, calcium, magnesium, ammonium, and bicarbonate [78]. This leads to a loss of the high osmolarity present in the medulla, and prevents the kidney from reabsorbing water. The primary clinical use of furosemide is for treating hypertension as the increased excretion of fluid reduces blood pressure and edema. The decrease in active transport in the medulla increases medullary  $PO_2$  since a major determinant of intrarenal oxygenation is from tubular metabolism [11].

These solute gradients, normally maintained in the medulla, are key to the functioning of the kidney. Ascending and descending vasa recta (AVR and DVR respectively) are in a countercurrent arrangement. This arrangement is critical for maintaining the osmotic gradient between the cortex and medulla regions, and thus the urine concentrating ability of the kidney. This arrangement also results in  $O_2$  diffusing from the DVR to the AVR, shunting the  $O_2$  between them before it reaches the medulla [74]. This decreases the amount of  $O_2$  actually reaching the medulla.

Unlike other organs,  $O_2$  use varies with blood flow in the kidney. The primary metabolic demand in the kidney is due to solute reabsorption, which can increase with blood flow. While the juxta-glomerular apparatus provides a critical feedback mechanism to control GFR, it only operates over a limited range. Blood flow to the cortex normally provides oxygen far in excess of its demand. However, in the medulla the countercurrent blood flow arrangement and active solute reabsorption reduces the  $PO_2$  to around 10-25 mmHg [74], compared to 40-60 mmHg in the renal cortex [72]. This unusual arrangement

can place the medulla at risk of hypoxic injury despite the fact that the kidney receives 30% of total cardiac output.

In chronic kidney disease (CKD), this meager  $O_2$  environment may be disrupted. CKD is due to several etiologies but the common factor is reduced GFR. As GFR declines, risk of cardiovascular disease, cognitive, and physical impairment increases. Renal fibrosis is a key component of CKD, impairing oxygen diffusion and supply to tubular and interstitial cells. Hypoxia of tubular cells leads to apoptosis, which exacerbates the fibrosis leading to chronic hypoxia [70]. The final stage of this cycle is end stage renal disease (ESRD). The key to success in treating CKD is early detection [51]. Targeting inefficiencies in renal  $PO_2$  may be a key factor in determining which CKD patients will progress to ESRD.

## 2.2. Magnetic Resonance Imaging

Magnetic resonance imaging (MRI) is an extremely powerful technique that can non-invasively visualize anatomic structures and probe physiological processes of the body. MRI is remarkably good at providing high contrast between different types of tissue, both healthy and diseased. MRI researchers have also shown the sensitivity of the imaging modality to physiological processes such as brain activity, ischemia, hypoxia, and fibrosis. MRI scanners use powerful magnetic fields to excite the most abundant (by count) element found in the human body, hydrogen (specifically, bound hydrogen in water molecules). While other forms of MRI can work with other elements, the mainstay is water-bound hydrogen. The signal given off by the water-bound hydrogen atoms is sensitive to its local environment and can be used to differentiate tissue types and physiologies. This technique is known as nuclear magnetic resonance.

### 2.2.1. Nuclear Magnetic Resonance

Nuclear magnetic resonance (NMR) is a method for probing molecular structure and is fundamentally a quantum process. Every elementary particle has a set of intrinsic properties such as mass and charge. Early quantum physicists discovered that subatomic particles have intrinsic angular momentum. Originally, this was thought to originate from a charged spherical particle spinning rapidly on its axis, creating a magnetic moment. When placed in a magnetic field, this magnetic moment will experience a torque. The spin will tend to align with the field to minimize the energy in the system. Much like a spinning top, if the axis of rotation is perturbed away from this minimal energy state, it will begin to precess around it. This precession is known as Larmor precession and is dependent on the particle type and proportional to the magnetic field strength:

$$\omega = \gamma B$$

where  $\gamma$  is the gyromagnetic ratio (MHz/Tesla) of the atomic structure and  $B$  is the magnetic field strength. This precession is detectable by a nearby coil of wire and is the basis of the NMR signal (fig. 2.5). While this classical analogy is illuminating, it does not provide the complete picture and is physically impossible (i.e. the particle would need to rotate faster than the speed of light to produce the observed effects).

Quantum physics gets its name from the quantized nature of the laws of physics. The spinning sphere discussed in the previous paragraph has a continuous range of angular momentum. In reality, the subatomic particle's intrinsic angular momentum is quantized, thus it can only take on a discrete set of values. This is very different from the classical

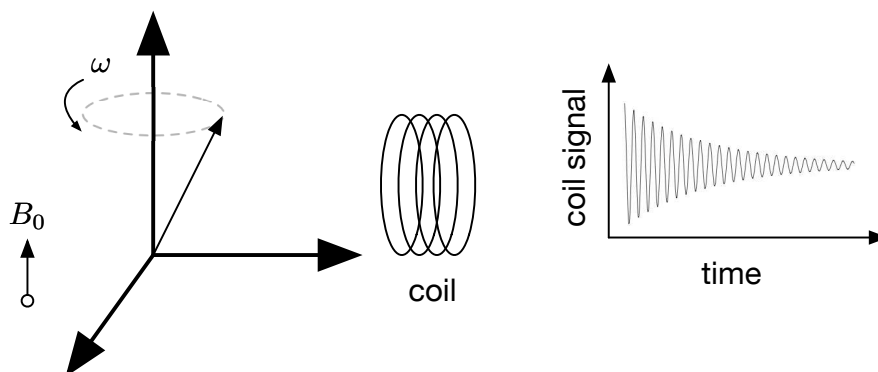


Figure 2.5. Spin vector precession around the magnetic field axis.  $\omega$  is the Larmor frequency

view of angular momentum, but due to the similarities, this quantized intrinsic angular momentum was named *spin*. The particle is not actually spinning. The Heisenberg uncertainty principle of quantum physics explains that there are limitations on what properties can be simultaneously observed. The classical spinning top violates this principle. Angular momentum and position cannot be precisely known at the same time. When a subatomic particle is placed in a magnet it will not completely align with it. Instead, it will be slightly offset and Larmor precession will kick in, keeping the uncertainty principle satisfied.

When subatomic particles are combined together their net spin is what determines the strength of the NMR signal. When protons and neutrons are combined to form a nucleus, they are arranged in such a way to minimize the energy of the combined state. When filling energy states, opposite spin states will be paired together to cancel each other out. Atoms with even numbers of both protons and neutrons will have no net spin. On the other hand, atoms with an odd count of either will have a net spin. If both the amount neutrons and protons are odd, then a net integer spin is produced. If only one of them

is odd, and the other even, then a half integer spin is produced. The net spin is used to determine the number of energy states that the atom can occupy. As long as there is a non-zero spin, an NMR signal can be produced.

### **2.2.2. Free induction decay**

The most basic NMR experiment is the free induction decay (FID). A sample of pure hydrogen atoms is placed in a strong, static, and uniform magnetic field. Hydrogen contains a single proton, so the net spin of each atom is  $1/2$ . The Zeeman effect says that when placed into a magnetic field, the hydrogen atoms, which are just protons, will occupy one of two energy states. The minimum energy state is to tend to align in parallel with the field (angle allowed by the uncertainty principle). The other state is anti-parallel to the applied magnetic field. Thermodynamic energy in the system will cause transitions between these two states, preventing all spins from being in the lower energy state. However, there will be a majority of spins in this lower state creating a net magnetization that is initially located along the field axis. A secondary oscillating magnetic field is applied at the Larmor precession frequency. This causes transitions from the lower energy state to the higher one. After excitation, these spins are initially coherent, creating a net magnetization in the plane perpendicular to the magnetic field. The magnetization continues to rotate at the Larmor frequency in this plane. Gradually, the excited spins lose energy and transition back to the lower energy state.

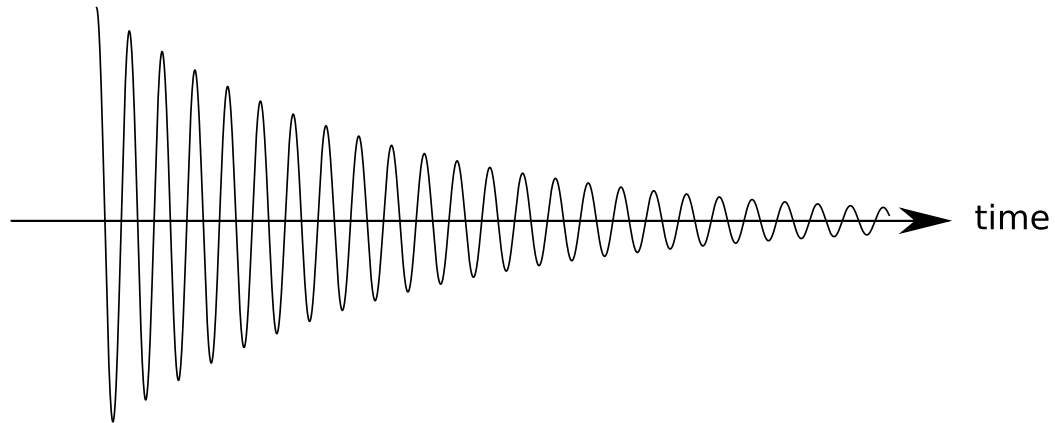


Figure 2.6. An example sketch of a free induction decay. Magnetization is picked up in a nearby coil, oscillating at the Larmor frequency. The signal gradually decays as spins leave the excited state.

### 2.2.3. Relaxation

Figure 2.6 shows a sketch of a free induction decay. While it is expected for the signal to decay due to spins leaving the higher energy state, the observed decay in the signal occurs much quicker than would be expected. Each spin in the sample will experience small non-reversible perturbations in its local magnetic field. The ensemble of spins will lose its initial phase coherence, and the transverse magnetization decays. This is referred to as  $T_2$  or  $R_2$  ( $1/T_2$ ) decay. Different tissues will have different  $T_2$ s. This property of tissues is one of the main mechanisms for creating contrast in magnetic resonance imaging. However, this is only accurate if the substance's secondary magnetic properties (e.g. paramagnetic effects) are ignored and a completely homogeneous main magnetic field is applied. Figure 2.7 shows the difference between these two decays. The faster decay

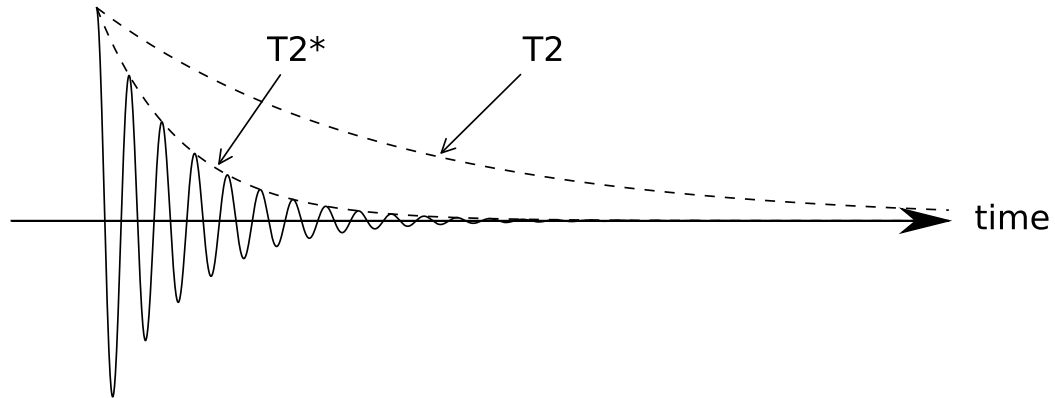


Figure 2.7. Sketch of free induction decay with T2 and T2\* relaxation.

is known as T2\* or R2\* ( $1/T2^*$ ) relaxation. This is often referred to as the apparent transverse relaxation time. It is related to R2 as  $R2^* = R2 + R2'$ . R2' can be thought of as the reversible component of R2\* and R2 as the non-reversible component.

#### 2.2.4. T2\* decay

T2\*, or R2\* ( $1/T2^*$ ), decay is caused by reversible local magnetic inhomogeneities. The reason it is referred to as reversible is because specially designed pulses can be used to reverse the phase accrued due to the magnetic field inhomogeneities. One of the most useful processes that leads to R2\* decay is the change in magnetic susceptibility of blood when oxygen binds to it.

### 2.2.5. Blood Oxygenation-Level Dependent (BOLD) MRI

Red blood cells are critical in the transport of oxygen to metabolic sites throughout the body. Only a small amount of oxygen can be directly dissolved in blood plasma. Red blood cells are rich in hemoglobin, which is a molecule that can bind oxygen and significantly increases the oxygen load that blood can carry. When no oxygen is bound to hemoglobin (deoxy-hemoglobin), the molecule is paramagnetic. This creates a local inhomogeneity in the magnetic field that can be detected as a frequency shift in the NMR signal or a decrease in  $R2^*$ . As more oxygen binds to hemoglobin molecules the effect is reduced. Changes in the saturation of hemoglobin can be measured as changes in  $R2^*$ .

### 2.2.6. Spin echoes

$R2^*$  decay causes the FID signal to decay away quite rapidly. However, the original  $R2$  signal can actually be recovered through the use of echoes. By applying another excitation pulse, this time inverting the magnetization signal such that it rotates  $180^\circ$ , the previously dephased spins will refocus and create an echo. The delay between the previous excitation and this inverting one is one half of the *echo time* (TE). By delaying for different TEs, the characteristic  $R2$  decay curve can be obtained. Using  $R2$  instead of raw values from an MRI image provides measurements that are more specific and robust to changes in certain setup parameters. The spin echo (SE) sequence is a simple method of using these spin echoes to obtain an image and produce spatial  $R2$  maps.

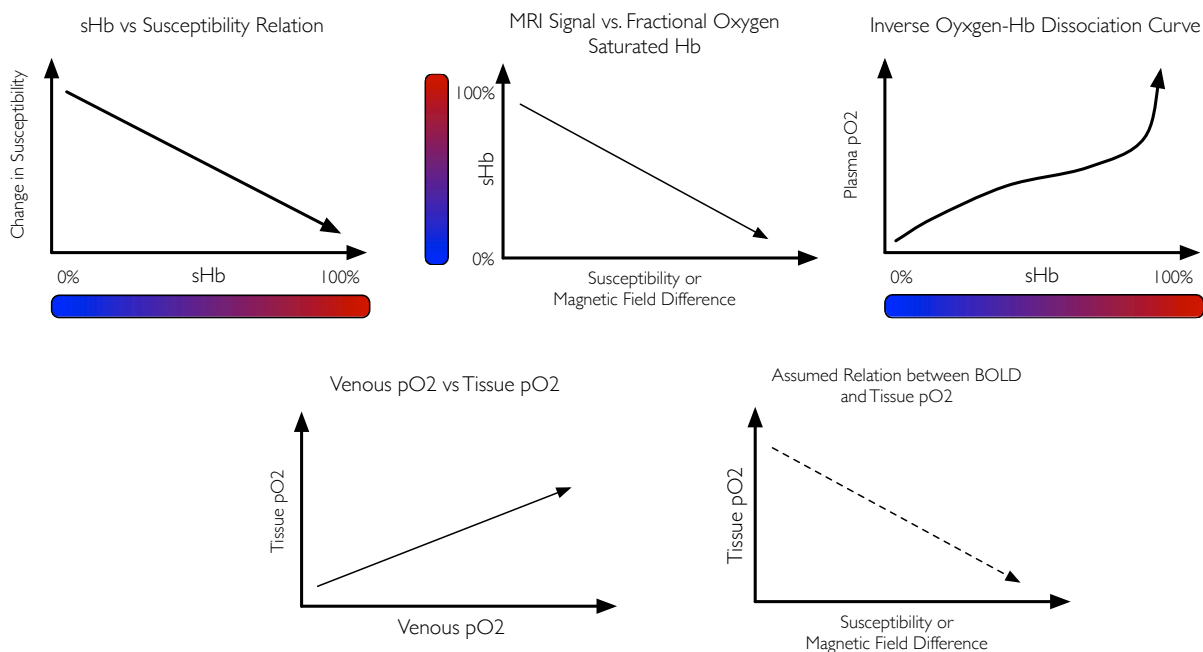


Figure 2.8. Schematic of the connection between the BOLD signal and tissue  $\text{PO}_2$ . Changes in sHb will lead to changes in the magnetic susceptibility of blood. Blood  $\text{PO}_2$  will increase as sHb increases by the oxygen-hemoglobin dissociation curve. Blood  $\text{PO}_2$  diffuses into tissue. The standard assumption of BOLD is that tissue  $\text{PO}_2$  is roughly in equilibrium with venous capillary  $\text{PO}_2$ .

### 2.2.7. Imaging

Herman Carr started his work with NMR in the 1940s. In one of his experiments he sought to understand the molecular structure of ethyl alcohol (ethanol). The FID of ethanol shows a much more complex pattern than that of the homogeneous hydrogen experiment. There is not a single Larmor frequency for the substance, as it is a relatively complex molecule. Protons are bound to carbon and oxygen atoms with different arrangements, which slightly alters the Larmor frequencies. When the frequencies are added together they form a “beating” pattern. While Carr was able to tease out the three different

frequencies from the time domain signal; he designed a simple model to show others how such a FID could be produced. He arranged three vessels with volumes in the same proportions as the ethanol peaks and spaced them to maintain the same ratio as the frequencies in the ethanol spectrum [49]. A linear magnetic gradient was then applied along the spatial axis of the vessels to create different magnetic fields at each location, thus creating different Larmor frequencies for each vessel. This arrangement mimicked the peaks seen in the ethanol NMR spectrum. This was the first instance of a one-dimensional magnetic resonance image. The key insight was to use a magnetic field that varied through space to encode spatial locations as different frequencies in the FID time course. Two-dimensional images are a simple extension of this. Another gradient is applied along an axis perpendicular to the first to encode spatial locations across a 2D grid.

### 2.2.8. K-space

Imaging takes place in k-space. This is a spatial frequency domain of the final image that is produced. K-space is characterized by the phase and frequency of each local magnetization vector in the system. Imagine a 2D grid divided into small cubic regions, or voxels. Each voxel contains its own magnetization vector that can be individually manipulated by spatial gradients. The phase accrued in one of these voxels is

$$\phi = \gamma \int_0^t B(\tau) d\tau$$

where  $B(t)$  is the local magnetic field that can arbitrarily vary with time. If a linear gradient is used such that the magnetic field at any point in the x-y plane is

$$B(x, y, t) = xG_x(t) + yG_y(t)$$

then the total phase at any point is

$$\begin{aligned}\phi(x, y, t) &= 2\pi(xk_x + yk_y) \\ k_i &= \frac{\gamma}{2\pi} \int_0^t G_i(\tau) d\tau \\ i &\in x, y\end{aligned}$$

Magnetization vectors rotating in the x-y plane can be written as phasors and the net signal is written as

$$s(t) = \int_x \int_y M_{xy}(x, y) \exp(-i2\pi(xk_x + yk_y)) d_x d_y$$

where  $M_{xy}$  is a function proportional to the density of spins at each location in space. This turns out to be the Fourier transform of the imaged object and provides a clear method from converting the acquired signal back into the actual spatial distribution.

K-space must be traversed by the imaging sequence in order to create an image. By varying  $G_x(t)$  and  $G_y(t)$  any arbitrary path can be traced out in k-space.

### 2.2.9. Imaging sequences

MR images are created by exciting ensembles of spins and then traversing k-space. The magnetization that is induced in the coil is discretely sampled and saved. This signal is the Fourier transform of the actual image. Reconstruction can thus be as simple as

applying an inverse Fourier transform. This collection of actions is known as a sequence and is typically represented in a sequence diagram. Figure 2.10 and fig. 2.11 are two examples. The diagram shows the events that take place to perform the sequence; the x-axis represents time.

Radio frequency (RF) pulses are used to excite the spins and alter their relative angle to the main magnetic field. Among other things, these pulses are used for creating various forms of contrast in the image. Without RF pulses, there is no signal for the imaging gradients to readout.

Descending down the sequence diagram, the next three rows show the imaging gradients. The two example sequences shown in this chapter both perform 2D imaging. The first step in most 2D imaging sequences is to perform a slice-selective excitation of the region of the body to be imaged.  $G_{SS}$  is the gradient time course that takes place simultaneously with the excitation RF pulse. If this gradient is not applied then the entire sample will be excited. Figure 2.9 shows an overview of the process.

The 2D imaging gradients for phase encoding and frequency encoding ( $G_{PE}$  and  $G_{FE}$  respectively) are used to traverse k-space across the previously slice selected region. In a sequence diagram, the integral of the gradient time course shown is the distance that is traversed in k-space. In fig. 2.10,  $G_{PE}$  and  $G_{FE}$  show a rasterized readout of k-space. The downward blips at the beginning of  $G_{PE}$  and  $G_{FE}$  move the initial point in k-space to the lower left corner. Each positive blip of  $G_{PE}$  then increments one row up on the y-axis of the 2D region. At the same time,  $G_{FE}$  zigzags back and forth across the x-axis. This produces the signal seen at the bottom of the sequence diagram.

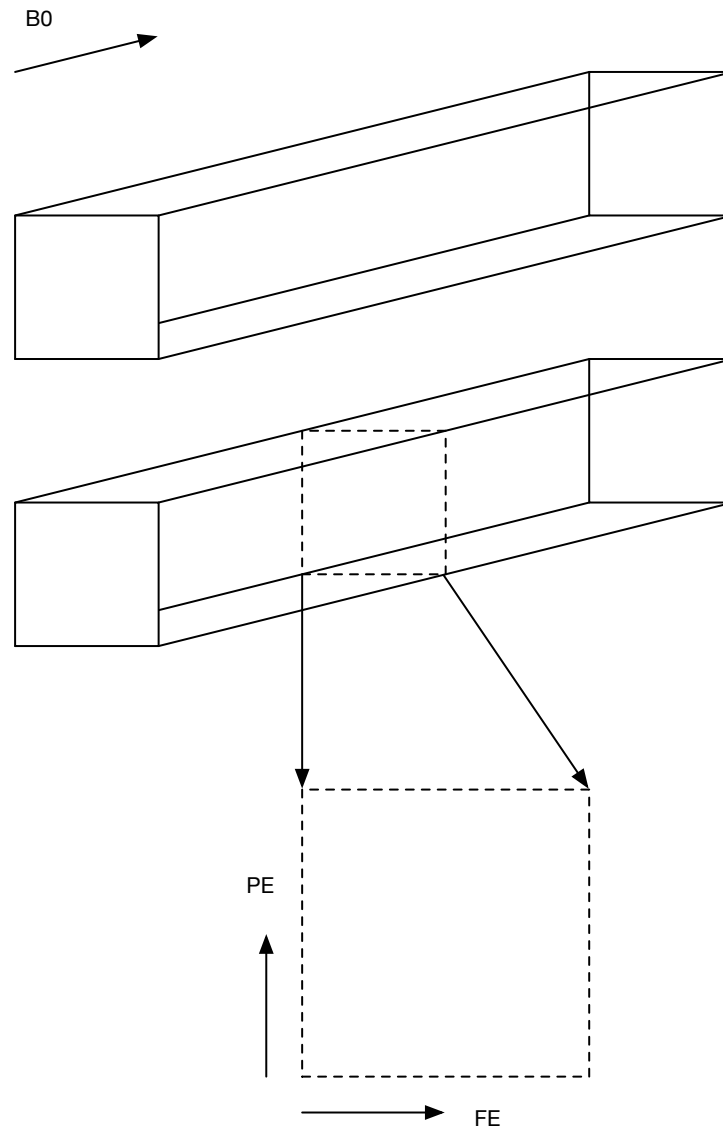


Figure 2.9. Layout of a typical 2D imaging experiment. The top figure shows a rectangular sample placed in a static magnetic field ( $B_0$ ). Next, the slice selection step is shown; only the region designated by the dashed line is excited by the RF pulse. The final figure shows the directions of phase encoding (PE) and frequency encoding (FE) that are used to create an image.

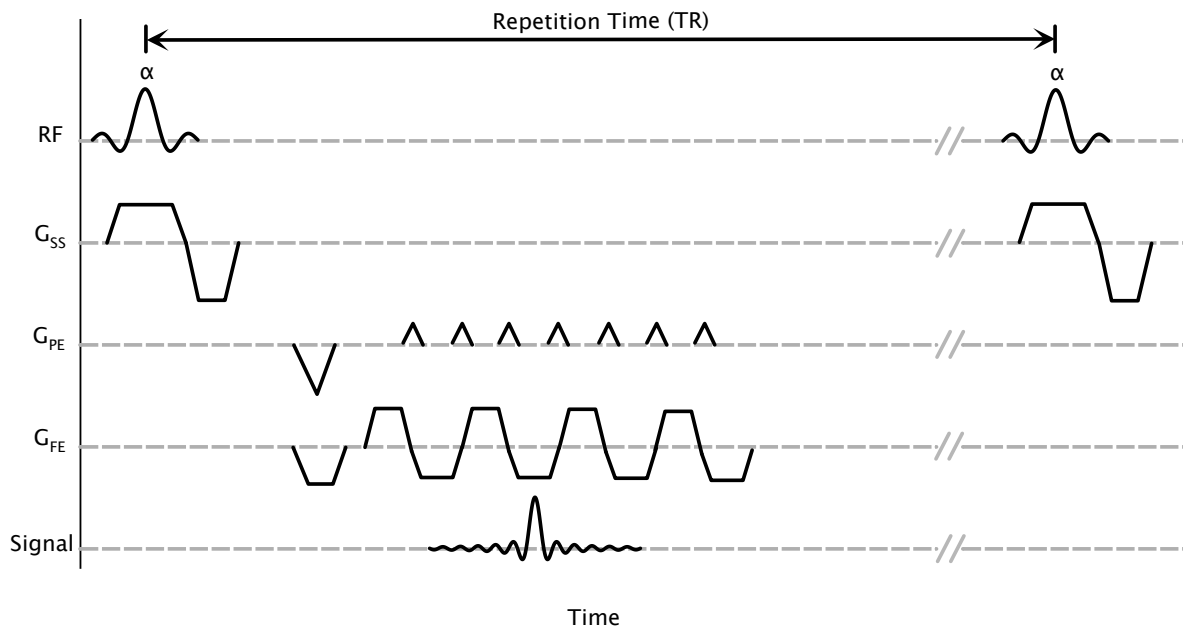


Figure 2.10. Example diagram of an Echo Planar Imaging (EPI) pulse sequence. The key novelty of the EPI sequence is its speed. By moving in a zig-zag pattern across k-space, the EPI sequence can read out an entire image in a single echo. This sequence can be modified to spin echo sequence by adding a  $180^\circ$  pulse.

### 2.2.10. Echo planar imaging (EPI)

EPI is a very fast method for traversing k-space. An example plus sequence is shown in fig. 2.10. This pulse sequence reads out an entire 2D field of view with a single excitation pulse. K-Space is rapidly traversed in a rasterized pattern (i.e. zigzagging across it). This can be split into multiple acquisitions and is known as multi-shot EPI.

### 2.2.11. Gradient recalled echo (GRE) sequence

The gradient recalled echo pulse sequence (GRE) is an extension of the single FID pulse experiment but applied to two or three dimensional imaging. GRE is the primary method for acquiring BOLD images.

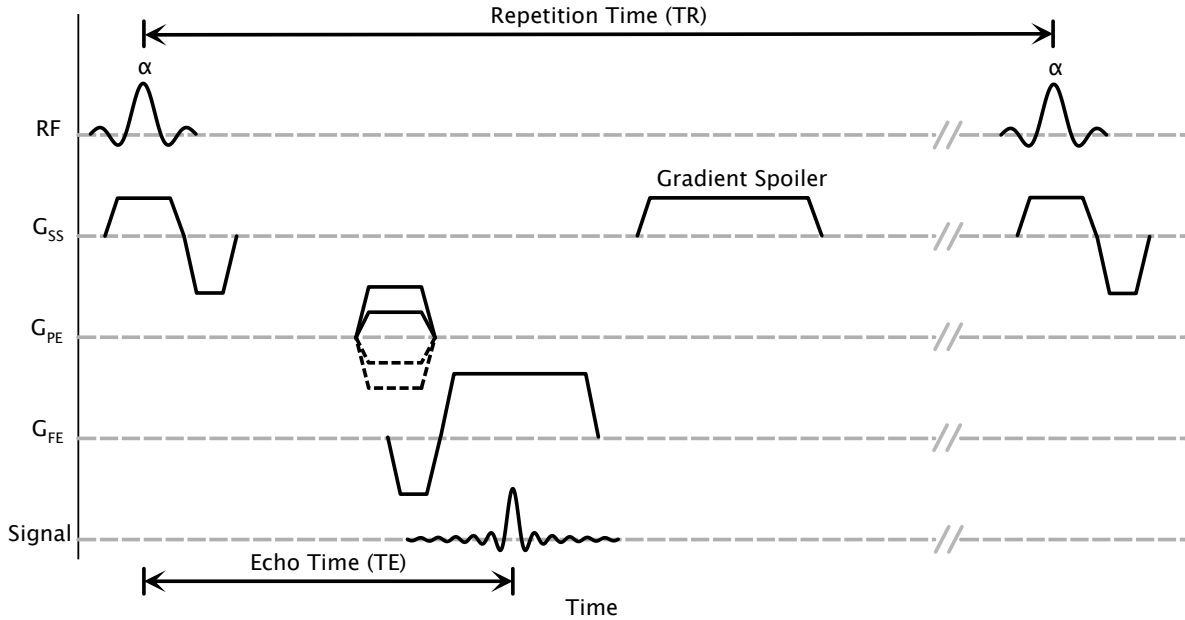


Figure 2.11. Example diagram of a Gradient Recalled Echo (GRE) pulse sequence. This is the main sequence used for creating  $R2^*$  images.

### 2.3. Phosphorescence Lifetime Imaging

Phosphorescence lifetime imaging provides a method for measuring oxygen concentrations in biological specimens. The process is an oxygen-dependent quenching of the phosphorescence of the molecule. Collisions between an excited triplet state phosphor and a ground state oxygen molecule transfer energy from the former to the latter [62]. The excited triplet state is returned to the ground state and emits light. The rate of decay of the triplet state is increased as oxygen concentrations increase.

Pd-porphyrin is an injectable oxygen-quenched phosphorescence lifetime imaging probe. It is bound to albumin, allowing it to be injected intravascularly and remains in that space. Response time to light excitation is on the order of milliseconds, allowing

real time measurements of  $\text{PO}_2$ . Calibration of the molecule is an important step in converting the phosphorescence decay rate to  $\text{PO}_2$ . However, calibration constants can be determined independently of the probed specimen because the phosphorescence is only dependent on its local molecular environment.

## CHAPTER 3

**Objective Analysis of the Renal Parenchyma BOLD MRI Data****3.1. Introduction**

Renal hypoxia is thought to play a key role in the progression of chronic kidney disease (CKD) [29,70], leading to an interest in non-invasive assessment of renal oxygenation. Renal blood oxygenation level-dependent (BOLD) magnetic resonance imaging is currently the only known non-invasive method that can be used to evaluate renal oxygenation in humans (8,9). Extensive research has shown that this technique has the ability to detect intra-subject changes following various interventions [22, 54, 56, 80]. There is a growing interest in applying this method to distinguish different groups of subjects, such as those with CKD, as compared to control subjects [41, 68, 83, 105]. However, experience to-date has led to conflicting reports on whether renal BOLD can detect differences between controls and subjects with CKD. Non-uniform hydration status between subjects, varied oxygenation due to multiple etiologies and a variation in medication among the subjects may at least in part explain some of the discrepancies [71]. Additionally, the method of analysis may play a role [83].

Renal BOLD MRI studies have predominantly used the mean value of small, manually defined ROI within the cortex and medulla. This technique is useful for cases where the renal cortex and medulla are readily discernible, such as at baseline in healthy subjects.

---

Originally published as J. M. Thacker, L. Li, W. Li, Y. Zhou, and P. V. Prasad, "Renal Blood Oxygenation Level-Dependent Magnetic Resonance Imaging: A Sensitive and Objective Analysis," *Invest. Radiol.*, vol. 50, no. 12, pp. 821827, 2015.

However, the contrast may not be sufficient to distinguish the two regions in patients with CKD or even healthy subjects following furosemide administration [22]. It is known that cortico-medullary contrast decreases in advanced CKD, making this technique sub-optimal for analyzing such cases [50]. Recent studies have indicated the subjectivity of this regional segmentation technique and a few methods to overcome the limitations have been proposed [20, 77, 88]. There is an inherent heterogeneity in the distribution of  $R2^*$  values even within each of the two different renal tissues [65]. Researchers have attempted to reduce this variation by defining several ROIs and taking the average of their means as a measure of  $R2^*$  for each region [98]. Alternately, in the cortex, it is possible to define a large ROI that acts as an average across the entire region.

A method that minimizes the subjectivity of ROI placement in renal BOLD analysis will be especially important for comparing data from different institutions and establishing renal BOLD MRI as a clinically viable technique [111]. One method of addressing these issues is through histogram analysis of the renal parenchyma. Histogram analysis has been effectively applied to diffusion maps in the cervical cord of multiple-sclerosis patients [99], diffusion images for intracranial tumor differentiation [63] and renal tumor classification [30], and more recently to arterial spin labeled images of mild CKD patients [87]. Based on this general principle, we have tested the hypothesis that a method that analyzes the  $R2^*$  distribution of the entire renal parenchyma will be able to detect quantitative changes in subjects following interventions and between groups of subjects with different levels of kidney function. Due to the mixed distribution of tissues within the parenchyma when taken as a whole entity, the renal  $R2^*$  distribution will not be normally distributed. This implies that the mean and standard deviations (first two moments) may not be sufficient

to fully represent the actual distribution. We have explored the use of two additional moments for characterizing this distribution. While our method is related to histogram analysis, it does not require a bin size and assumes nothing about the distribution of values. Furthermore, we utilize a kernel density estimate of the empirical distribution when displaying the distributions, as it does not require a bin size as well. Hence forth, our method will be referred to as moment analysis.

To determine a robust (sensitive and objective) method for analyzing renal blood oxygenation level-dependent (BOLD) MRI data, we have evaluated the ability of conventional BOLD analysis and parenchyma moment analysis to detect inter- and intra-subject differences in controls and subjects with CKD. Specifically, we have evaluated the inter-rater agreement, sensitivity to changes following administration of furosemide, and the relative sensitivity of the methods in differentiating controls from subjects with CKD.

## 3.2. Materials and Methods

### 3.2.1. Subjects

All procedures were performed with approval from the institutional review board and written subject consent. A total of 47 subjects participated: controls (n=17; age:  $41.6 \pm 12.9$  yrs; estimated glomerular filtration rate (eGFR)= $97.1 \pm 15.0$ ; 9 male/8 female), CKD (age:  $61.9 \pm 10.4$  years; eGFR in the range of 30-90 (n=20) and  $< 30$  (n=10); proteinuria =  $0.83 \pm 0.9$ ; systolic BP= $130.7 \pm 25.6$  mmHg; diastolic blood pressure= $70.7 \pm 15.5$  mmHg; average duration =  $7.6 \pm 5.2$  years; 15 male/15 female). Subjects with unilateral disease were excluded. Subjects were instructed to fast starting after midnight on the day of the study. The scanning was performed in the morning.

### 3.2.2. MRI Protocol

All experiments were performed on a 3 Tesla whole-body scanner (MAGNETOM Verio, Siemens Healthcare, Erlangen, Germany) equipped with high performance gradient coils (45 mT/m maximum gradient strength, 200 mT/m/ms slew rate). A body array coil was used for transmission and the spine and body array coils were combined for signal reception. All subjects were examined in the supine position with their feet entering the scanner first. BOLD MRI data was acquired using a breath-hold multiple gradient echo (mGRE) sequence with following parameters: field of view = 360 x 245mm, number of slices = 5, slice thickness = 5.0mm, matrix size = 256 x 176, repetition time = 62ms, number of echoes = 8 equally spaced (3.09 to 32.3ms), averages = 1, flip angle = 30°. BOLD MRI measurements were made at baseline. The patient table was moved to administer 20 mg of furosemide iv. Post-furosemide data was acquired approximately 15-minutes after the baseline scans. The action of furosemide is to inhibit reabsorptive transport along the medullary thick ascending limb which increases medullary PO<sub>2</sub> [11].

### 3.2.3. R2\* Maps

The eight images from each mGRE acquisition were used to estimate R2\* on a voxel-by-voxel basis, using an offline linear least squares regression. Magnitude images were thresholded at 20 (a.u.) to remove values where the R2\* is so high that the signal decays into the noise floor in later echoes. These occur in places with large changes in susceptibility such as regions neighboring the large intestines or areas of no signal (background). Typically this resulted in less than a mean loss of 7% (0.2% median) voxels

within a ROI.  $R2^*$  maps were created for each subject at baseline, and post-furosemide administration.

#### 3.2.4. Regions of Interest

Two observers defined ROIs in the cortex, medulla, and the entire renal parenchyma for both the left and right kidneys on the first mGRE image of the center slice. Care was taken not to include any voxels from areas near strong susceptibility changes or other artifacts. Tumors and cysts were excluded from the ROIs as well (2 cases). Additionally, macroscopic vasculature was removed when it was readily apparent to the observers. However, they represent a very small number of voxels within the whole parenchyma and are thus expected to have a minimal effect on the computed values, even when not completely removed. Cortical ROIs were drawn according to two common methods: 2-3 small ROIs ( $< 100$  voxels) and one large ROI ( $> 500$  voxels) encompassing the vast majority of the cortex (fig. 3.1). Separate ROIs were defined for each subject at baseline and post-furosemide.

After all the ROIs were defined, they were copied to the  $R2^*$  maps to compute the mean value for each region. ROIs on baseline images were matched to post-furosemide images when possible but were drawn separately. The parenchyma ROI was used for higher moment analysis in a similar fashion.

#### 3.2.5. Moment Analysis

Following manual segmentation of the renal parenchyma, the  $R2^*$  distributions were analyzed using four sample moments  $(\mu_1, \mu_2, \mu_3, \mu_4)$ . The first moment is the sample mean

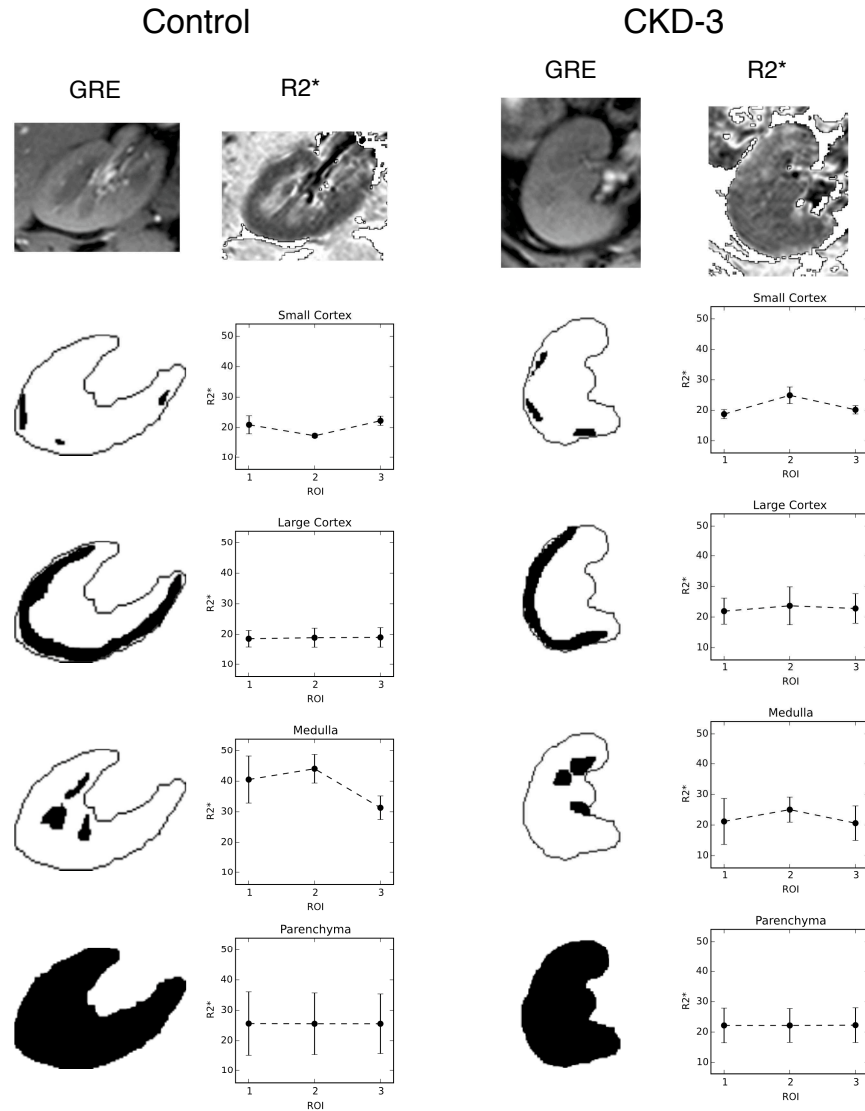


Figure 3.1. An example of the variation seen in the mean  $R2^*$  depending on ROI placement. The left column shows a representative control subject and the right a CKD subject. The first echo from the mGRE images is used as an anatomical template for placing ROIs. The image appears a bit blurry as it is interpolated to this larger size for viewing purposes. The ROI is then used to find the mean of the corresponding region on the calculated  $R2^*$  map. Three different ROIs are placed for each region (large cortical and parenchyma ROIs are difficult to see due to the overlap of each region). The mean and standard deviations of each region are shown in the plots. Variation between the ROIs is quite large in the small regions, while the larger ones are clearly not as susceptible to differences in exact placement.

$\mu_1$ , and the next three are central moments (computed around the mean). Given the mean  $\mu_1$ , for  $n > 1$ , the  $n^{th}$  central moment of an image,  $I$ , containing  $V$  voxels, is defined as

$$\mu_n = \frac{1}{V} \sum_{i=1}^V (I_i - \mu_1)^n$$

In statistics, the first three moments after the sample mean are commonly referred to as the standard deviation ( $\mu_2$ ), skewness ( $\mu_3$ ) and kurtosis ( $\mu_4$ ). These can be considered to describe the shape features of the distribution. These names generally refer to standardized moments, which are defined in relation to the normal distribution. The parenchyma distribution is not expected to be normally distributed due to the inclusion of two distinct regional distributions. We preferred to use the actual moments as parameters rather than use the standard statistical nomenclature. These methods reduce the large number of R2\* parenchyma samples to a set of numerical values summarizing the shape of the distribution. Thus, each subject had four values per stage (baseline and post-furosemide). Statistical comparisons were performed with this set of data.

### 3.2.6. Statistical Analysis

Statistically significant changes were assessed between baseline and post-furosemide R2\* measurements, separately in control and CKD groups, for each of the regions. A Wilcoxon non-parametric test was used for this matched pairs comparison. Control and CKD groups were compared in each region and at each stage for statistically significant differences with a Mann-Whitney U test. To help estimate the effect size for each comparison, we report Cohen's d. The use of effect size in addition to p values has been recommended for scientific reporting [94]. Cohen's d effectively represents the effect size in three levels:

small, medium and large corresponding to  $d$  values greater than or equal to 0.2, 0.5 and 0.8 respectively. We report values as being pragmatically significant when there is both a substantial effect size, (i.e.  $|d| \geq 0.5$ ) and statistical significance (i.e.  $p < 0.05$ ). Multiple comparisons were corrected for by applying the Holm-Bonferroni method to limit the family wise error rate in reporting false rejections of the null hypothesis. This correction was applied to each set of regional measurements. Values are reported as the mean standard deviation where applicable. All analysis was performed using Python 2.7.2 and the SciPy 0.13.3 module [44].

To assess the effects of variability in the definition of ROIs on the computed values, the intra-class correlation coefficients (ICC) were evaluated. The ICC will be high when there is little variation between the scores given to each subject by the raters. ICC values are generally stratified as poor agreement ( $< 0.75$ ), moderate agreement ( $> 0.75$ ) and good agreement ( $> 0.9$ ). ICCs were determined for the mean value of each region and between the various measures used in the multiple moment method.

### 3.3. Results

#### 3.3.1. Comparison of Mean Values

Figure 3.1 shows an example of these ROIs and the potential variation in the mean values of the individual ROIs. The mean  $R2^*$  of the small ROIs can vary considerably depending on their placement while the large cortical and parenchyma ROI show very little change based on the plots.

The renal parenchyma mean provides the highest inter-rater agreement ( table 3.1 and fig. 3.2. Small ROIs (cortex and medulla) show the least agreement between raters, and

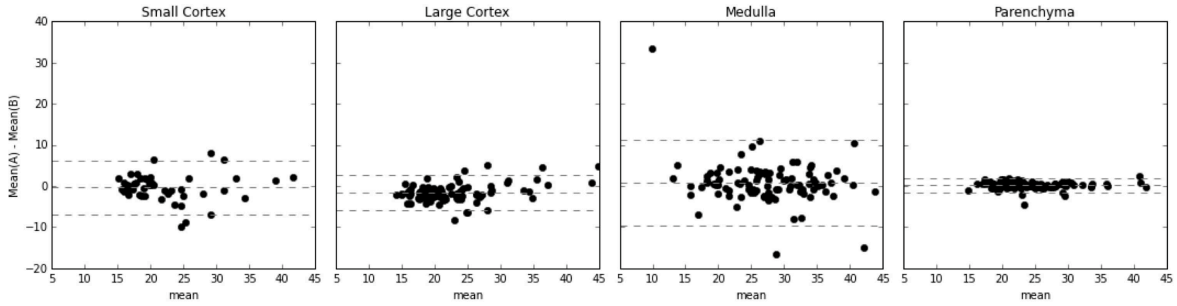


Figure 3.2. Mean-difference (Bland-Altman) plots depicting the inter-rater agreement for each ROI region. The medulla shows the highest variation while the parenchyma shows the lowest. Additionally, the large cortex shows a lower level of variation than the small cortex does.

the medulla has the lowest inter-rater agreement of all regions ( $ICC=0.76$ ). When we analyzed the control and CKD groups separately, the ICC values were not significantly different, 0.76 for CKD vs 0.80 for control (other regions not shown). Since the large cortex has a higher level of agreement than the small cortex does, it is the only region assessed outside of the comparison of intra-class correlation.

Table 3.1. Intra-class correlation coefficients for mean values of each region at baseline

Region	ICC	95% CI
Small Cortex	0.87	[0.78, 0.92]
Medulla	0.76	[0.61, 0.86]
Large Cortex	0.93	[0.88, 0.96]
Parenchyma	0.99	[0.98, 0.99]

When comparing baseline and post-furosemide mean  $R2^*$  values, the parenchyma mean shows a significant difference in control subjects ( table 3.2). Subjects with CKD also show a change in the medulla and the parenchyma ( $p < 0.05$ ), but the magnitude of the change is considerably less than in the control group as indicated by d ( table 3.3).

Table 3.2. Controls Baseline vs. Post-furosemide R2\*. † Wilcoxon signed rank test statistic. ‡ Cohen's d measure of effect size

Region	Baseline R2* ( $s^{-1}$ )	Post R2* ( $s^{-1}$ )	P-value†	d‡
Large Cortex	19.6 ± 3.6	18.7 ± 4.7	0.22	0.21
Medulla	30.9 ± 4.1	22.5 ± 5.0	0.002	1.59
Parenchyma	23.8 ± 2.7	20.6 ± 4.1	0.002	0.84

Table 3.3. CKD Baseline vs. Post-furosemide R2\*. † Wilcoxon signed rank test statistic. ‡ Cohen's d measure of effect size

Region	Baseline R2* ( $s^{-1}$ )	Post R2* ( $s^{-1}$ )	P-value†	d‡
Large Cortex	23.9 ± 7.3	22.0 ± 6.9	0.056	0.22
Medulla	29.7 ± 7.2	26.7 ± 7.0	0.039	0.35
Parenchyma	26.3 ± 6.1	24.8 ± 5.6	0.004	0.21

When comparing controls and subjects with CKD at baseline, the cortical ROI shows a significant difference between control and CKD subjects while the parenchyma mean does not (table 3.4). However, after furosemide administration, both regional and parenchyma ROIs show a significant difference, with the parenchyma showing the largest effect size (table 3.5). The cortical effect size decreased from baseline and the medulla also shows a significant difference. No significant difference was found between left and right kidneys using any of the traditional ROI analysis technique or between any of the moments (data not shown).

Table 3.4. Control vs. CKD at baseline. § Mann-Whitney U test statistic. ‡ Cohen's d measure of effect size

Region	Baseline R2* ( $s^{-1}$ )	Post R2* ( $s^{-1}$ )	P-value§	d‡
Large Cortex	19.6 ± 3.6	23.9 ± 7.3	0.015	-0.69
Medulla	30.9 ± 4.1	29.7 ± 7.2	0.28	0.18
Parenchyma	23.8 ± 2.7	26.3 ± 6.1	0.152	0.39

Table 3.5. Control vs. CKD post furosemide. <sup>§</sup> Mann-Whitney U test statistic. <sup>‡</sup> Cohen's d measure of effect size

Region	Baseline R2* ( $s^{-1}$ )	Post R2* ( $s^{-1}$ )	P-value <sup>§</sup>	d <sup>‡</sup>
Large Cortex	18.7 ± 4.7	22.0 ± 6.9	0.026	-0.51
Medulla	22.5 ± 5.0	26.3 ± 7.0	0.019	-0.61
Parenchyma	20.6 ± 4.1	24.8 ± 5.6	0.003	-0.75

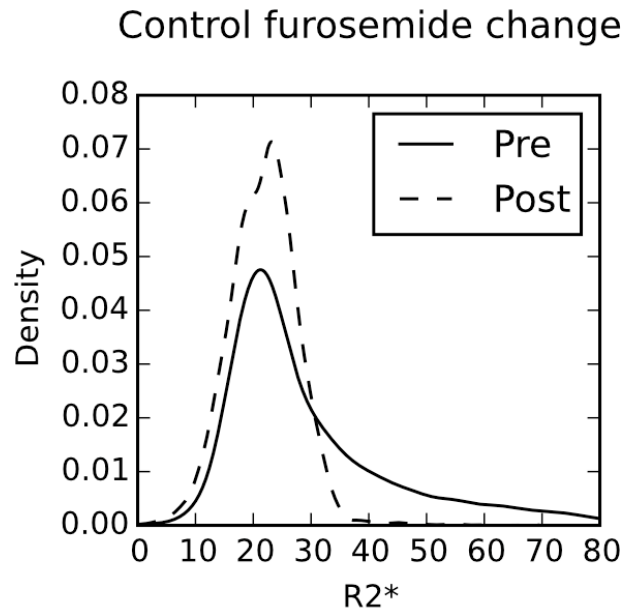


Figure 3.3. Example kernel density plots of typical cases for each of the comparisons performed in tables 3.2 to 3.10. A kernel density plot is used to estimate the empirical distribution and is not sensitive to the bin size like a histogram would be. A kernel density estimate with Gaussian kernels and automatic bandwidth calculation was used to estimate the continuous probability distribution.

### 3.3.2. Moment Analysis

Figure 3.3 illustrates a representative distribution of renal parenchymal R2\* values at baseline and after administration of furosemide in a control subject. Clearly one can

visualize differences in these distributions. Consistent with the mean value, the higher moments of the parenchyma data showed similar trends. Table 3.6 shows that all four moments are significantly different following furosemide in the control group. While there was no significant difference observed at baseline between CKD and control subjects (table 3.8), post-furosemide show that the first two and the fourth moments are significantly different (table 3.9). Additionally, ICC assessed inter-rater agreement of these moments was comparable to large cortical regions (table 3.10).

Table 3.6. Higher parenchyma moments: Controls Baseline vs. Post-furosemide. <sup>†</sup> Wilcoxon signed rank test statistic. <sup>‡</sup> Cohen's d measure of effect size

Moment	Baseline R2* ( $s^{-1}$ )	Post R2* ( $s^{-1}$ )	P-value <sup>†</sup>	d <sup>‡</sup>
$\mu_1$	$23.8 \pm 2.7$	$20.6 \pm 4.1$	0.008	0.84
$\mu_2$	$88.7 \pm 39$	$48.5 \pm 15$	0.001	1.04
$\mu_3$	$1.26 \pm 0.8 \times 10^3$	$0.59 \pm 0.3 \times 10^3$	0.007	0.83
$\mu_4$	$53 \pm 43 \times 10^3$	$22 \pm 14 \times 10^3$	0.007	0.72

Table 3.7. Higher parenchyma moments: CKD Baseline vs. Post-furosemide. <sup>†</sup> Wilcoxon signed rank test statistic. <sup>‡</sup> Cohen's d measure of effect size

Moment	Baseline R2* ( $s^{-1}$ )	Post R2* ( $s^{-1}$ )	P-value <sup>†</sup>	d <sup>‡</sup>
$\mu_1$	$26.3 \pm 6.1$	$24.8 \pm 5.6$	0.02	0.21
$\mu_2$	$79.3 \pm 26$	$73.6 \pm 30$	0.28	0.17
$\mu_3$	$0.87 \pm 0.53 \times 10^3$	$0.89 \pm 0.65 \times 10^3$	0.56	-0.02
$\mu_4$	$36.5 \pm 22 \times 10^3$	$36.8 \pm 30 \times 10^3$	0.88	-0.01

### 3.4. Discussion

#### 3.4.1. Comparison of Mean Values

Our results demonstrate that the renal parenchyma mean is highly objective in terms of inter-rater reliability and is able to detect intra-subject changes following administration

Table 3.8. Higher parenchyma moments: Baseline Controls vs. CKD. § Mann-Whitney U test statistic. † Cohen's d measure of effect size

Moment	Baseline R2* ( $s^{-1}$ )	Post R2* ( $s^{-1}$ )	P-value <sup>§</sup>	d <sup>†</sup>
$\mu_1$	$23.8 \pm 2.7$	$26.3 \pm 6.1$	0.30	-0.49
$\mu_2$	$88.7 \pm 39$	$79.3 \pm 26$	0.28	0.23
$\mu_3$	$1.3 \pm 0.8 \times 10^3$	$0.87 \pm 0.5 \times 10^3$	0.11	0.45
$\mu_4$	$53.4 \pm 43 \times 10^3$	$36.5 \pm 22.4 \times 10^3$	0.24	0.38

Table 3.9. Higher parenchyma moments: Post-Furosemide Controls vs. CKD. § Mann-Whitney U test statistic. † Cohen's d measure of effect size

Moment	Baseline R2* ( $s^{-1}$ )	Post R2* ( $s^{-1}$ )	P-value <sup>§</sup>	d <sup>†</sup>
$\mu_1$	$20.6 \pm 4.1$	$24.8 \pm 5.7$	0.003	-0.75
$\mu_2$	$48.5 \pm 15$	$73.6 \pm 30$	0.005	-1.00
$\mu_3$	$0.59 \pm 0.3 \times 10^3$	$0.89 \pm 0.7 \times 10^3$	0.11	-0.54
$\mu_4$	$22.4 \pm 14 \times 10^3$	$36.8 \pm 29 \times 10^3$	0.01	-0.59

Table 3.10. Intra-class correlation coefficients for each of the parenchyma moments.

Moment	ICC	95% CI
$\mu_1$	0.99	[0.98, 0.99]
$\mu_2$	0.94	[0.90, 0.97]
$\mu_3$	0.92	[0.86, 0.95]
$\mu_4$	0.90	[0.83, 0.94]

of furosemide, a widely used pharmacological maneuver for BOLD MRI studies. It is well known that the observed changes following furosemide are regional, with the medulla showing a large change in R2\* while the cortex shows minimal to no change. Despite not segmenting the medulla, this regional change is still detectable. Whether the same trend will be observed with other pharmacological maneuvers will require further work.

The need for including effect size in order to determine a significant result cannot be understated. Scientific literature has generally placed emphasis on a statistical significance that is based solely on the p-value, typically at a significance level of 0.05. However, does

not necessarily mean that the observed difference is of any practical consequence. Even small differences will reach statistical significance provided the sample size is large enough [94]. It is considerably more informative to determine an estimate of the magnitude of the difference and whether it is large enough to differentiate a condition of interest, e.g. healthy vs. CKD. It has been suggested that the effect size should be reported along with, or in place of, p-values [34, 94]. Previous reports have suggested that an effect size of 0.5 could be considered a medium effect and 0.8 considered as a large effect. In this report, we have used  $p < 0.05$  and  $d > 0.5$  to imply a pragmatic notion of significance. Further work may be necessary to reach consensus on what value would be optimal for specific applications.

Cortical  $R2^*$  values were significantly higher in subjects with CKD (Table 4). While the mean parenchyma  $R2^*$  values at baseline did not show a difference between the groups, when evaluated post-furosemide, all regions were found to be significantly different. The parenchyma mean actually showed a larger effect size than the cortex at this stage or at baseline. Post-furosemide data combines the differences in cortical  $R2^*$  values and the responses to furosemide in the medulla between the groups of subjects.

### 3.4.2. Physiological Interpretation

The mean  $R2^*$  value (or first moment) of the parenchyma and medulla demonstrated significant changes post-furosemide in control subjects. The observed medullary changes in healthy controls are consistent with several prior reports [22, 57, 58, 83]. The mean  $R2^*$  value of the parenchyma would be a weighted mean of the cortical and medullary compartments. This results in a smaller effect size ( $d=0.84$ ) compared to the medulla ( $d=1.59$ ).

However, the ability to detect these changes without regional segmentation indicates that the contributions (magnitude and voxel count) from the medulla are sufficiently large. While the response to furosemide in subjects with CKD also reached p values  $< 0.05$ , the effect sizes were all quite small, indicating a considerably smaller change in  $R2^*$ . This trend is consistent with a recent report [83]. The ability to detect differences based on the renal parenchyma without a priori knowledge of regional anatomy greatly simplifies image analysis and is expected to be beneficial in comparing data from different institutions.

$R2^*$  is used as a surrogate for oxygenation due to its sensitivity to the saturation of hemoglobin (sHb). However, this depends on both oxygen delivered and oxygen consumed. Furosemide provides a method to reduce the local oxygen consumption in the medulla in healthy functioning kidneys and results in a higher blood oxygenation, observed as a decrease in  $R2^*$ . Prior studies have captured these differences by evaluating  $R2^*$  following furosemide with significantly lower changes in subjects with CKD [108]. Our results with analyzing post-furosemide  $R2^*$  distributions of renal parenchyma demonstrate an alternative way of capturing the relative differences in response to furosemide. This is most probably related to the opportunistic leveraging of both the increased cortical  $R2^*$  in CKD and a lower response to furosemide in the medulla.

The chronic hypoxia model suggests that subjects with progressive CKD may exhibit higher renal hypoxia [28]. Additionally it is estimated that only 1 in 3 patients at stage 3 have progressive CKD [28]. Thus, it is possible that the differences observed between subjects with CKD and healthy controls are smaller than they would be if the group assessed in this study was restricted to just progressors. To-date, no study assessing renal oxygenation has sought to, or identified subjects with progressive CKD.

### 3.4.3. Multiple Moment Analysis

By looking at higher moments we were able to capture more changes in the shape of the  $R2^*$  distribution than would be possible with only the mean (Table 6 and Table 7). Figure 3.3 shows a typical case of how the distributions varied between baseline and post-furosemide in a control subject. The mean or first moment ( $\mu_1$ ) provides information regarding the central tendency of the distribution. The second moment ( $\mu_2$ ) indicates the spread of the distribution and may be related to the separation of  $R2^*$  values between the cortical and medullary regions (clearly the spread is lowered post furosemide). The third moment ( $\mu_3$ ) relates to the skewness of the distribution and may indicate the relative strength of each compartment (also lower post-furosemide). Lastly, the fourth moment ( $\mu_4$ ) provides information about the relative magnitude of the tails, the values far from the center of the distribution (clearly this is smaller post-furosemide). However, it is not yet clear how to interpret these additional parameters in practical terms.

### 3.4.4. Limitations

There are some limitations with our study. It is important to note that our healthy control group was not age matched to the CKD group. This was primarily due to logistical challenge of recruiting healthy elderly subjects. Earlier reports have failed to demonstrate any significant differences in cortical  $R2^*$  values with age [83]. However, contributions from age-related differences might not be ruled out in our observations. A previous paper did show that response to furosemide might be blunted in older subjects [22], possibly accounting for the difference in post-furosemide  $R2^*$  values between controls and subjects with CKD observed here. In this preliminary study, the CKD group had a heterogeneous

distribution of eGFRs, etiologies and medications. Additionally, potential movement between baseline and post-furosemide images may shift the region of the kidney being analyzed.

While the thresholds used for determining significance of our results seem to be appropriate for the context of this work, they will require independent validation to reach consensus.

Use of the renal parenchyma in place of the cortex and medulla has been used in prior reports. Ebrahimi et al modeled the distribution as a two compartment model whose applicability is not strictly feasible when there is limited contrast between cortex and medulla, e.g. subjects with CKD or in healthy subjects post-furosemide [20]. Piskunowicz et al did not assume a two compartment model, but their approach involves the use of a discrete number of layers, each adding several new parameters to the analysis [77]. Saad et al used a measure of fractional tissue hypoxia from the whole parenchyma as a replacement for individual regional measures from the cortex and medulla. This method used a fixed value of  $30 \text{ s}^{-1}$  to separate  $R2^*$  values into high and low levels of hypoxia [88]. Our approach requires no apriori assumptions. It may be more straightforward to implement, even though custom software will be necessary. Future consensus from the user community may be necessary for optimal choice among the methods for more general acceptance.

### 3.5. Conclusion

In conclusion, our results show that the mean of the renal parenchyma provides a higher inter-rater agreement when analyzing renal  $R2^*$  maps than cortical or medullary

ROIs. In addition, it shows sufficient sensitivity, in terms of the effect size, when evaluating the response to furosemide, a well-established pharmacological maneuver in renal BOLD MRI. A new finding is that post-furosemide  $R2^*$  maps may show more significant differences between controls and subjects with CKD with both a conventional regional ROI analysis and the proposed analysis using the entire renal parenchyma. In addition, by using higher moments, the sensitivity to detecting both inter- and intra-subject differences could be improved. However, the physiologic interpretation requires further studies and independent validation.

As take home messages, our data support the use of the entire renal parenchyma when analyzing  $R2^*$  maps from subjects with minimal cortico-medullary contrast. Alternately, large cortical ROIs could be used for evaluating baseline differences between different groups of subjects. Even in healthy subjects, the use of both cortical, and parenchyma analysis may be preferred for comprehensive and objective evaluation. The limitations of using only p values for significance have been known, but our data further highlight the need to use additional information such as the effect size.

## CHAPTER 4

**Physiologically Relevant Parameters: BOLD Derived Renal  $PO_2$** **4.1. Introduction**

Blood oxygen level dependent (BOLD) MRI is a non-invasive method that is sensitive to regional oxygen saturation of hemoglobin (SHb). It is currently the only non-invasive method available to evaluate relative renal oxygenation status, and it can be readily applied in humans [80]. Previous studies have established BOLD MRI as an effective and sensitive method for monitoring changes in both pre-clinical models [14, 18, 76] and in humans [9, 40, 80]. However, translation of BOLD MRI to the clinic remains challenging [71].

Two key limitations are suspected to play a role. One is the use of small region of interest (ROI) analysis. Small ROIs are subjective and may be limited by the available contrast between regions, which can be compromised under certain disease states [50]. There have been recent developments to mitigate this issue by using methods that analyze the entire renal parenchyma [20, 77, 88, 97]). Another limitation of BOLD MRI is the inability to directly compare the measurements between regions due to the fact that the  $R2^*$  (or  $T2^*$ ) measurements, the transverse relaxation rate, depend on more parameters than just the magnetic susceptibility of deoxygenated hemoglobin. These parameters include the spin-spin relaxation rate ( $R2$ ), regional blood volume, and hematocrit (Hct). Each

---

Originally published as J. Thacker, J. L. Zhang, T. Franklin, and P. Prasad, "BOLD quantified renal  $PO_2$  is sensitive to pharmacological challenges in rats," *Magn. Reson. Med.*, 2016. Reprinted with permission John Wiley and Sons, license 3966891427805.

of these may vary significantly between individuals, even regionally within a kidney, and with disease. These dependencies limit the ability to directly compare  $R2^*$  measurements between kidney regions or measurements between groups. For example, the inner medulla in rodents consistently has a lower  $R2^*$  than the cortex, and would be viewed as having a higher blood  $PO_2$  level based on the usual BOLD interpretation. However invasive measurements show the inner medulla has the lowest  $PO_2$  [5]. This discrepancy is thought to be due to the lower blood volume and lower hematocrit of the inner medulla [75]. Furthermore,  $R2^*$  cannot directly indicate hypoxic regions. An increased  $R2^*$  may show a region with decreased oxygen availability due to the measured decrease in SHb, but it does not indicate whether the tissue's oxygen demand is being met. It is known that certain regions of the kidney are operating on the verge of hypoxic conditions and the ability to convert  $R2^*$  measurements to blood  $PO_2$  could provide a means of comparing these regions to  $PO_2$  levels that may be at risk of hypoxic damage.

Recent work has demonstrated the feasibility of mapping BOLD MRI measurements to blood  $PO_2$  [110]. The method is based on  $R2'$  ( $R2^*-R2$ ) as opposed to the conventional  $R2^*$  parameter. Using Monte Carlo simulation, the model estimates  $R2'$  for a given SHb value, resulting in a look-up table from  $R2'$  to SHb, for each tissue type based on regional parameters. In this preliminary study, we applied this model to a small number of rats to find baseline blood  $PO_2$  estimates and compared the estimates to invasive measurements from the literature. We further evaluated the sensitivity of the method to changes in  $PO_2$  following pharmacological maneuvers.

## 4.2. Methods

### 4.2.1. Animals

The Institutional Animal Care and Use Committee approved all procedures and protocols in this study. Six male Sprague-Dawley rats (Charles River, Chicago, IL), weighing  $402 \pm 20$  g, were used in this study. Rats had free access to water and food prior to being anesthetized. All procedures were conducted under anesthesia using Inactin (thiobutabarbital sodium, 100 mg/kg i.p., Sigma-Aldrich, St. Louis, MO). A catheter (PE-50 tubing) was placed in the femoral vein of each rat for administration of nitric oxide synthase inhibitor (L-NAME) and furosemide (Sigma-Aldrich, St. Louis, MO). These drugs were used to modulate renal perfusion and/or oxygenation. Each drug is administered at a concentration of 10 mg/kg body weight into the femoral vein as a bolus.

Each animal's tail was connected to a peripheral oximeter to monitor any systemic changes in global blood SHb (3150 MRI Patient Monitor, Invivo Research Inc). Measurements were recorded every five minutes.

### 4.2.2. MRI

All experiments were performed on a 3-Tesla whole body scanner (Magnetom Verio, Siemens Healthcare, Erlangen, Germany), equipped with high-performance gradient coils (45 mT/m maximum gradient strength, 200 mT/m per milliseconds slew rate). Rats were placed in a right decubitus position, such that the kidneys were in the middle of a knee coil (8-channel Knee Coil, Siemens Healthcare, Erlangen, Germany). Each rat was then positioned within the MRI scanner such that the middle of the kidney being examined was at the isocenter of the magnet.

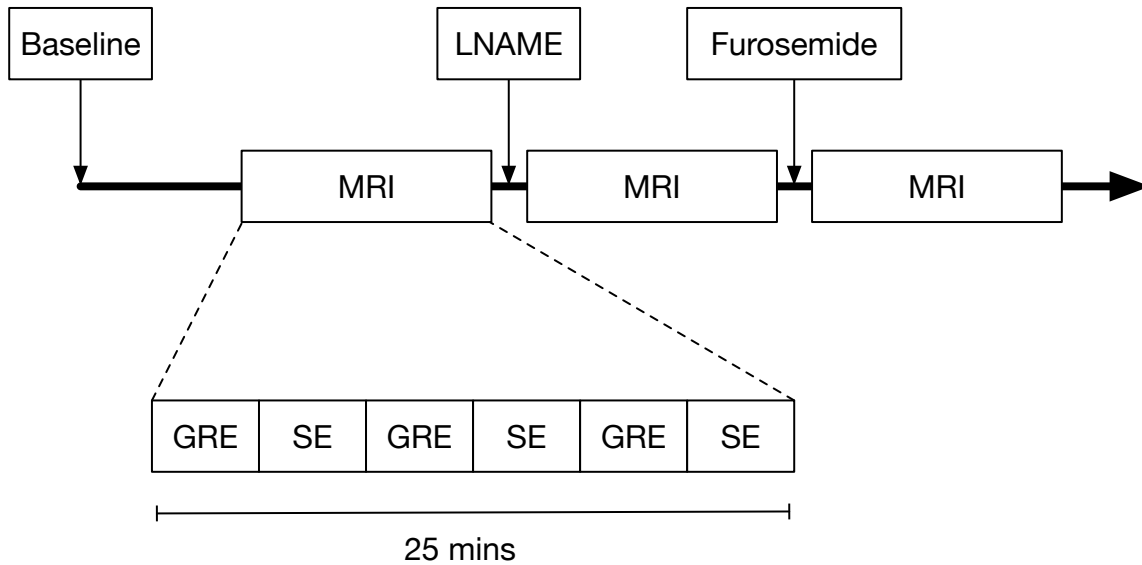


Figure 4.1. MRI protocol. The MRI data acquisition was performed in three stages: baseline, LNAME and furosemide. Each MRI stage consisted of three repetitions of alternating mGRE and SE acquisitions.

Imaging was performed in three stages: baseline, post-LNAME and post-furosemide administration. Figure 4.1 shows a schematic outline of the procedure. Each stage consisted of two sequences: a multiple gradient recalled echo sequence (mGRE, 12 Echoes: TE: 3.56 - 41.29 ms increments of 3.43 ms, TR: 69.0 ms, Matrix: 256\*128, PhaseFOV: 50%, resolution: 0.47x0.47 mm, slice thickness: 2.0 mm), and a standard spin echo sequence (SE, 8 echoes: TE: 9.9 to 79.2 ms with increments of 10ms, TR: 500ms, Matrix: 256x128). Each set of mGRE and SE acquisitions were acquired three times, leading to a total study time of approximately 75 minutes per rat.

In two additional animals, we obtained data at baseline and after administration of furosemide.

### 4.2.3. Analysis

Following MRI data acquisition, regions of interest (ROIs) were manually defined (examples shown in fig. 4.4b) in the cortex (region furthest from the renal pelvis, containing majority of glomeruli) and the outer medulla (OM) (outer portion of the closest region to renal pelvis, borders cortex) of each kidney. A suite of custom image-processing software written in Python was used for the analysis (Python 2.7, NumPy 1.10, SciPy 0.16.1 [44]).

R2\* maps were created from the 12 echoes acquired by the mGRE sequences using a linear least squares fitting method, with regions near large susceptibility artifacts removed using thresholding [97]. R2 maps were created from the eight echoes acquired by the SE sequences using a linear least squares fitting method. As each MRI stage acquired 3 pairs of mGRE and SE acquisitions, the computed maps were averaged over these repetitions. ROIs representing the two regions were applied to the R2\* and R2 maps, and the mean of each region was found. R2' was calculated by subtracting the R2 mean from the R2\* mean for each region.

A statistical model was used for estimating the oxygen saturation of hemoglobin (SHb) as well as the blood PO<sub>2</sub> of each region [110]. The model simulates the BOLD signal by modeling blood vessels as randomly oriented cylinders within a voxel and red blood cells as spheres. At the start of the simulation protons diffuse through the voxel, accumulate different phases, leading to a signal decay that is sensitive to the oxygen saturation of hemoglobin. The model was used to establish a relationship between SHb and R2' (fig. 4.2). Blood PO<sub>2</sub> was estimated from SHb using the oxyhemoglobin dissociation curve (fig. 4.2). The following parameters were assumed for each region: cortex (vascular fraction: 0.27, hematocrit: 0.4, extravascular diffusion coefficient: 1.45, intra-vascular

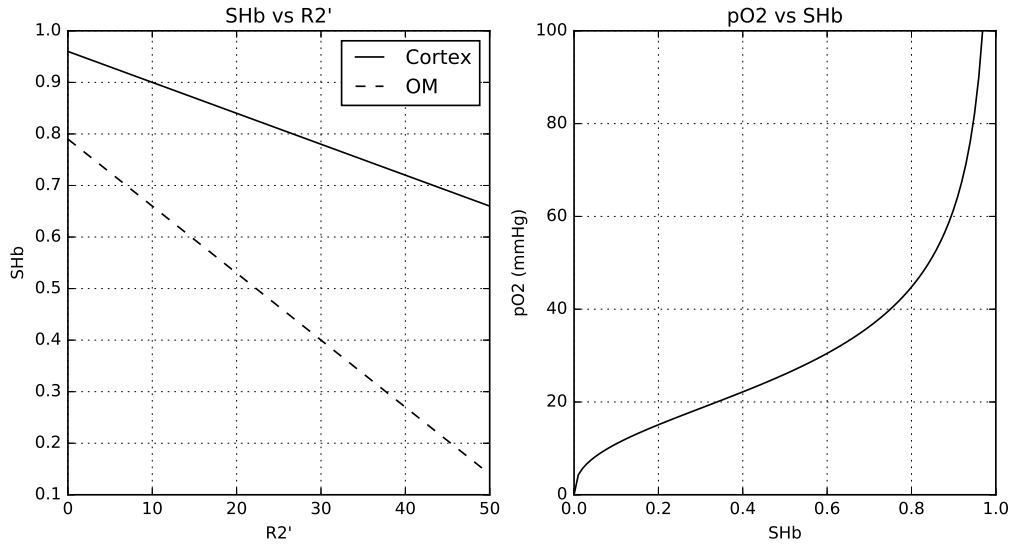


Figure 4.2. Monte Carlo simulation results in cortex and outer medulla. (a) Plot shows the relationship between a measured  $R2'$  and the expected hemoglobin saturation (SHb). (b) Plot showing the relationship between SHb and blood  $PO_2$ . See the methods section for a list of parameters used in the model.

diffusion coefficient: 1, average vesicle radius: 10 ( $\mu\text{m}$ )); outer medulla (vascular fraction: 0.18, hematocrit: 0.25, extravascular diffusion coefficient: 1.04, intra-vascular diffusion coefficient: 1, average vesicle radius: 10 ( $\mu\text{m}$ )) [31, 48, 65].

#### 4.2.4. Statistical Analysis

Statistically significant changes were assessed between each sequential stage within each region. Cohen's  $d$  was used to assess the magnitude of the change and Wilcoxon's signed-rank test was used to assess the statistical significance. While the range of  $d$  values depends on the experiment, a value of 0.8 or greater is generally considered a large effect

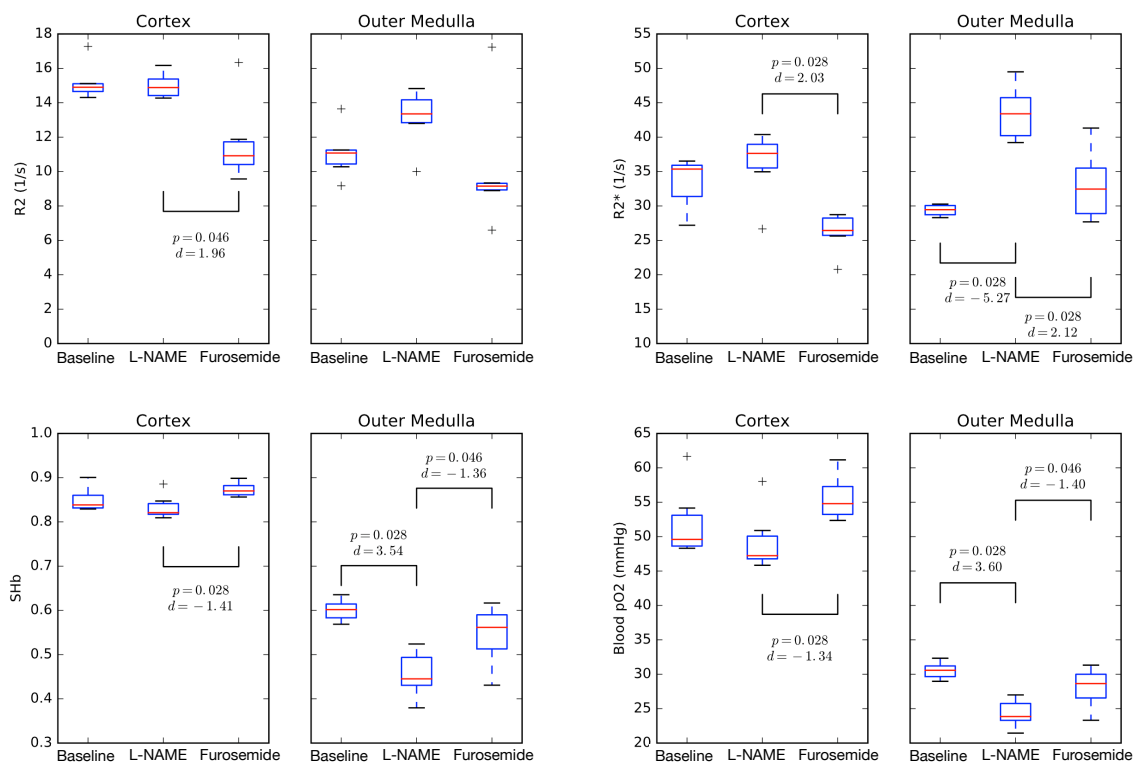


Figure 4.3. Box-whisker plots for R2 (a), R2\* (b), SHb (c), and blood PO<sub>2</sub> (d). The two regions assessed are shown (cortex and outer medulla (OM)). Each region shows three time points at which MRI was assessed: baseline, post-LNAME, post-furosemide.

[94, 97]. P-values are reported with each test as well, values below 0.05 are considered statistically significant.

### 4.3. Results

Our estimates for SHb and blood PO<sub>2</sub> showed regional responses to L-NAME and furosemide. Figure 4.3 show boxplots for each region at each of the three stages for estimated R2, R2\*, SHb, and blood PO<sub>2</sub>, respectively. At baseline, blood PO<sub>2</sub> in the outer medulla was found to be  $30.5 \pm 1.2$  mmHg and  $51.9 \pm 5.2$  mmHg in the cortex.

Statistically significant changes were observed in the outer medulla following L-NAME and furosemide. In the cortex, the change from L-NAME to furosemide was significant as well. Figure 4.3 shows box and whisker plots for each stage of the experiment. Each box extends from the lower quartile to the upper quartile, the horizontal line indicates the median. The whiskers show the range of the data to within 1.5 times the inter-quartile distance or the maximum data value. Values outside of the whisker's range are plotted as plus signs, indicating potential outliers.

Figure 4.4a shows examples of R2 and R2\* maps at each stage in one representative animal. Figure 4.4b is the summary of the mean PO<sub>2</sub> values for all rats at each time point within the stages.

Figure 4.5 shows the relative values of R2, R2\* and blood PO<sub>2</sub> in three spatial locations of the rat kidney. The differences observed in blood PO<sub>2</sub> are consistent with prior data based on invasive measurements.

No significant changes in peripheral SHb were found during the experiment in any of the rats (data not shown). In the two additional rats given just furosemide, the mean PO<sub>2</sub> change in the outer medulla was from 29.1 to 31.3 mmHg and in the cortex from 48.1 to 53.1 mmHg.

#### 4.4. Discussion

Our data supports the feasibility of applying this quantitative model to estimate renal blood PO<sub>2</sub> based on BOLD MRI data acquisitions in rat kidneys where there is a great amount of literature [5, 11, 61]. At baseline, blood PO<sub>2</sub> in the outer medulla was found to be 30.5 ± 1.2 mmHg and 51.9 ± 5.2 mmHg in the cortex, which is in line with previously

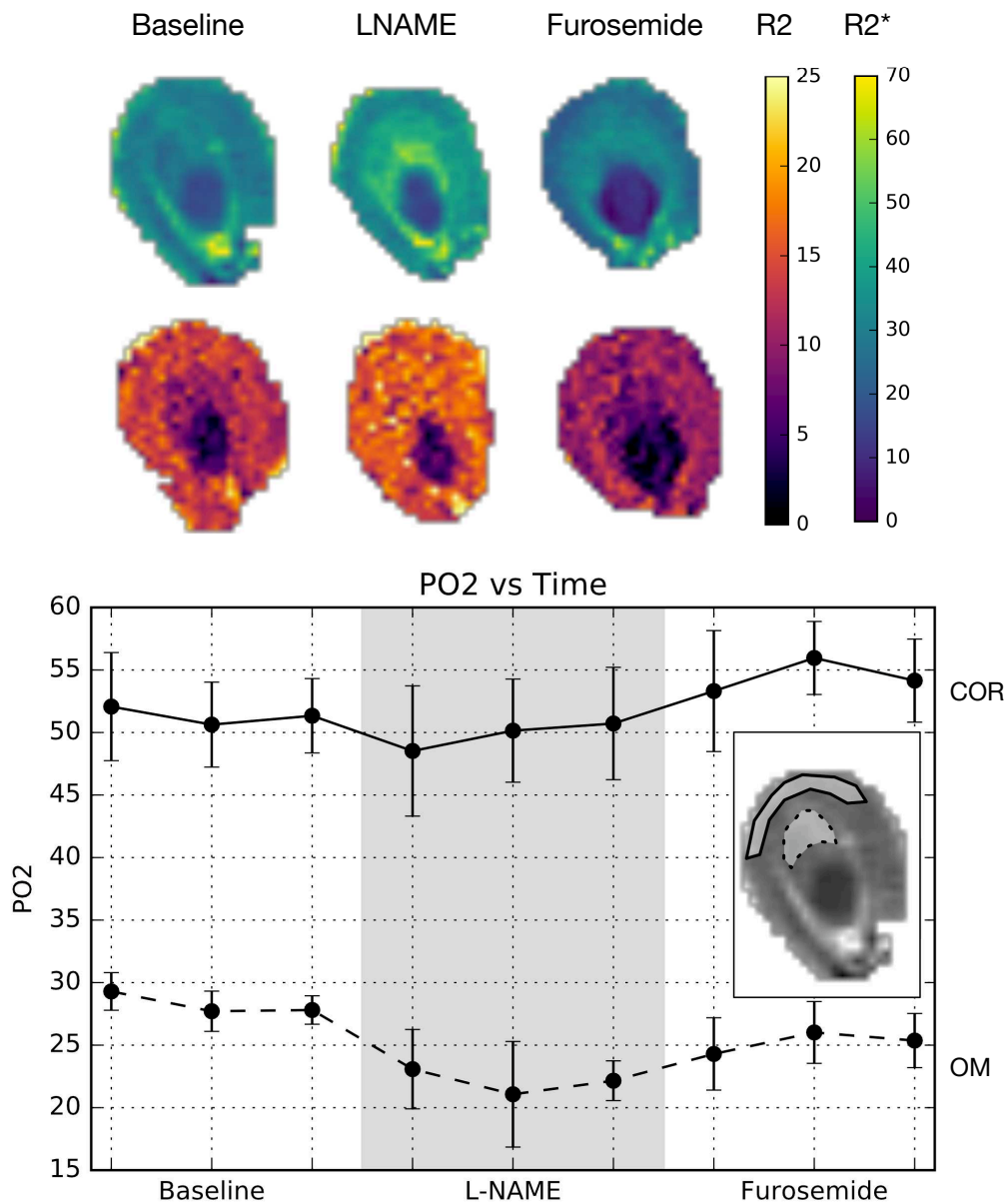


Figure 4.4. (a) shows R2 and R2\* maps at each stage in a representative animal. (b) is the summary of cortical and outer medullary PO<sub>2</sub> estimates from all animals at all individual time points for each stage. Typical ROIs are illustrated in (b) as well.

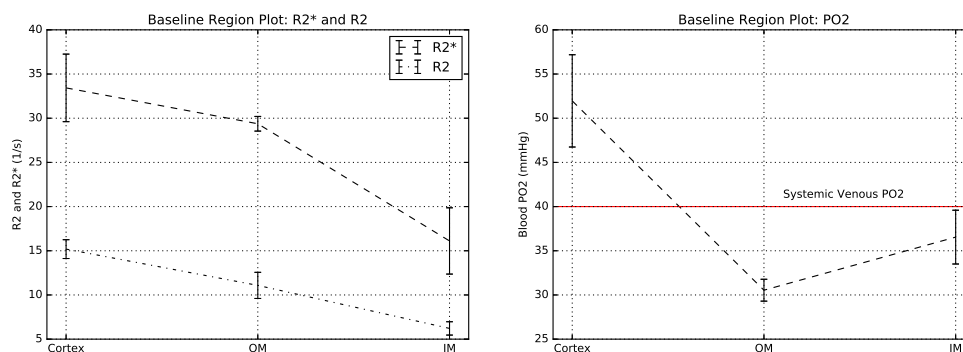


Figure 4.5. The relative values of  $R2$ ,  $R2^*$  and blood  $PO_2$  between each region are illustrated here. At baseline, the mean and standard deviations of are shown for each region for  $R2^*$  and blood  $PO_2$  measurements. The relative  $R2^*$  values are hard to interpret because the low  $R2^*$  in the inner medulla would indicate higher blood oxygenation. However, it is well known that inner medulla has the least  $PO_2$  [65]. Using the same parameters as the outer medulla, the estimated  $PO_2$  appears to be closer to the outer medulla. The conversion to  $PO_2$  also facilitates identifying regions that are hypoxic, e.g. compared to systemic venous  $PO_2$ .

measured values using microelectrodes [61]. However, as microelectrode studies are unable to differentiate between capillary blood  $PO_2$  and tissue  $PO_2$  the measurement is not entirely specific to the measurements reported here. Future studies that can differentiate between the two are necessary, e.g. using phosphometric measurements [104].

L-NAME acts as a vasoconstrictor in the renal circulatory system. Our results show that blood  $PO_2$  decreases following administration of L-NAME as expected [1]. The OM showed a significant decrease in  $PO_2$  ( $p=0.028$ ;  $d=3.60$ ). While the cortex showed downward shifts as well in blood  $PO_2$ , it was not statistically significant.

Furosemide acts to increase renal  $PO_2$  by inhibiting sodium reabsorption in the medullary thick ascending limb, and is generally confined to the medulla region [11]. As L-NAME is known to act for up to 2 hours [102], the observed post-furosemide response

is really a combined response to L-NAME and furosemide. In this preliminary study, our focus was to demonstrate sensitivity to hemodynamic changes and not to study the exact effects of each of the drugs in isolation, thus we consider this to be an acceptable compromise. From the results we see that a significant increase in  $PO_2$  is observed in both regions, with the larger change resulting in the OM ( $p=0.046$ ;  $d=-1.40$ ). However, in two additional rats, given just furosemide, an increase in  $PO_2$  was observed in outer medulla consistent with prior reports [11]. The cortex also showed an increase, probably due to the fact that cortical portion of the nephrons are a part of Henle's loops at the cortico-medullary junction and is consistent with a previous study [103].

Changes in  $R2^*$  are often discussed as being a measure of changes in oxygenation or degree of hypoxia. However, as shown in fig. 4.5, the relative values of  $R2^*$  do not strictly indicate the relative oxygenation in different regions. For the same reason, it is also not possible to define a threshold value of  $R2^*$  above which the tissue can be assumed to be hypoxic. However, by taking the differences in physiological parameters (HCT, blood volume, etc.) between the two regions into account, the estimated blood  $PO_2$  shows the well accepted gradient between the cortex and outer medulla. Further  $PO_2$  of the inner medulla (IM) is lower than the cortex, even though it is not lower than the outer medulla, as expected [5]. This is probably due to the lack of data on relative values of blood volume and Hct, specifically for IM. For this preliminary study, we assumed the same values for the entire medulla.

The primary mechanism for transporting  $O_2$  molecules in blood plasma to the mitochondria is diffusion [64]. The difference in blood  $PO_2$  and mitochondrial  $PO_2$  is what establishes this diffusion gradient and the maximum amount of  $O_2$  that can be extracted

from the blood in a given amount of time. While it is difficult to determine mitochondrial  $PO_2$  [8], one study has estimated it to be in the range of 30-40 mm Hg [69]. Thus, if blood  $PO_2$  is at or below this range, the oxygen will not be transported to the cells by diffusion and the tissue will be at risk of hypoxic injury. Interestingly, the systemic venous  $PO_2$  is also about 40 mmHg [13].

The relative  $PO_2$  values in fig. 4.5 suggest that the cortex is normoxic while both the outer and inner medulla are in the middle or below the mitochondrial  $PO_2$  range and could be classified as hypoxic. The estimates of inner medulla were based on blood volume and hematocrit estimates in outer medulla (due to lack of literature values). Whether that explains the relative higher values of  $PO_2$  requires further investigations.

#### 4.4.1. Limitations

There are limitations to this approach. The method for converting from MRI measured parameters ( $R_2$ ,  $R_2^*$ ) to physiological ones (SHb and  $PO_2$ ) requires a number of parameters that are regionally inhomogeneous and may not be readily available. This is especially true for changes in these parameters (e.g. regional hematocrit) in response to the pharmacological maneuvers. For example, following L-NAME administration, blood flow decreases and possibly a reduction in blood volume occurs as well. While a reduction in blood flow leads to a decrease in blood oxygenation, normally seen as increased  $R_2^*$ , the corresponding reduction in blood volume would serve to decrease  $R_2^*$ , possibly negating the former effect. Without an independent measure of blood volume, our model is unable to capture such a change, causing us to overestimate blood  $PO_2$  following LNAME. Similarly changes in these parameters under certain disease states could make comparisons

to healthy subjects challenging. The model makes assumptions about blood pH and the corresponding oxygen saturation curve that may not hold under certain disease conditions as well. Additionally, we did not control the water and salt intake of the animals in this preliminary study, which are known to influence  $R2^*$  [22, 82].

#### 4.5. Conclusion

In conclusion, the model for estimating blood  $PO_2$  based on BOLD MRI measurements shows promise in its ability to measure baseline  $PO_2$  in cortex and outer medulla. The validity of the changes observed following pharmaceutical maneuvers requires further work to validate against an invasive blood  $PO_2$  measurement. By taking into account the difference in hematocrit between the renal cortex and the outer medulla, the large difference in oxygenation between the two regions becomes readily apparent, this is not clear from the relative  $R2^*$  values (in fig. 4.5). The conversion of  $R2'$  to  $PO_2$  also allows for the possibility of classifying regional hypoxia. While there are several parameters that must be taken into account (blood pH, systemic hematocrit, etc.), it may be possible to calibrate these with a blood sample from each subject. By reporting physiological parameters, rather than conventional  $R2^*$  measurements, renal BOLD MRI may find a greater acceptance among physicians and an increased clinical utility.

## CHAPTER 5

**Invasive Renal Cortical PO<sub>2</sub>****5.1. Introduction**

BOLD measurements are the only non-invasive method sensitive to renal oxygenation. In chapter 4 it was shown that blood PO<sub>2</sub> could be estimated from BOLD MRI data. However, the method relies on several parameters taken from the literature. These parameters are vascular fraction, hematocrit, extravascular diffusion coefficient, intra-vascular diffusion coefficient, average vesicle radius, and p50 of blood. In order to translate this method to the clinic, it is critical to show that model can still match up with a more direct measure of blood PO<sub>2</sub>. The model is specific to blood PO<sub>2</sub> and using a method that can differentiate between blood and tissue PO<sub>2</sub> is important. While tissue PO<sub>2</sub> can be modeled as well, it requires transport constants that are not readily available in humans (2).

In this study we examine the use of phosphorescence lifetime as a potential method for refining our previous BOLD derived PO<sub>2</sub> measurements. Phosphorescence lifetime imaging is an oxygen-dependent quenching of the phosphorescence of an injectable phosphor (3). The phosphor is excited by a laser, emitting light when returning to the ground state. The rate of decay increases as oxygen concentrations increase.

Phosphorescence lifetime imaging has been used by many studies to perform PO<sub>2</sub> measurements in rats [24, 43, 90]. These studies used several different oxygen probes, but they all derive from the same family. These probes have the capability of being confined

to the vasculature or interstitium, due to either prebinding to albumin or binding to endogenous albumin. The ability to measure the difference between vascular and tissue  $PO_2$  can provide significant insight into modeling  $O_2$  diffusion and understanding the accuracy of BOLD  $PO_2$  estimates in relation to actual tissue level  $O_2$  pressures.

## 5.2. Methods

### 5.2.1. Animals

3 male Sprague-Dawley rats (Charles River, Chicago, IL), weighing  $506 \pm 94$  g, were used in this study. Rats had free access to water and food prior to being anesthetized. All procedures were conducted under anesthesia using Inactin (thiobutabarbital sodium, 100 mg/kg i.p., Sigma-Aldrich, St. Louis, MO). A catheter (PE-50 tubing) was placed in the femoral vein of each rat for administration of nitric oxide synthase inhibitor (L-NAME) (Sigma-Aldrich, St. Louis, MO). These drugs were used to modulate renal perfusion and/or oxygenation. Each drug is administered at a concentration of 10 mg/kg body weight into the femoral vein as a bolus. A 3-cm incision of the left flank is then made for access to one kidney, which was exposed and decapsulated.  $PO_2$  was measured at baseline and following L-NAME (0, 10, and 20 minutes post injection).

An oxygen sensitive molecular probe, meso-tetra (4-carboxyphenyl) porphine (Pd-porphyrin, Oxyphor R0, Oxygen Enterprises, Ltd. Philadelphia, PA), was dissolved in a bovine albumin solution (60mg/ml) at a concentration of 10 mg/ml and physiologically buffered to a pH of 7.4. It was injected through the femoral catheter at a dose of 20 mg/kg. Body temperature was maintained at  $37^\circ\text{C}$  via a copper tubing water heater. Each rat was placed such that the kidney was maintained in the imaging plane. Renal

oxygen pressure was measured at baseline and following L-NAME administration at 0, 10 and 20 minutes.

### 5.2.2. Phosphorescence Lifetime Imaging

A previously established phosphorescence lifetime imaging system [89, 90] was modified for renal  $PO_2$  imaging (r $PO_2$ ). The slitlamp biomicroscope incorporated a diode laser at 535 nm wavelength, an optical chopper, a high-pass filter with 650 nm wavelength cutoff and an intensified charge-coupled device (ICCD) camera. The laser was modulated by an optical chopper at 1.6 MHz and projected onto the renal tissue at a spot size of 4 mm to excite the oxyphor. Phosphorescence emission was selectively imaged using the high pass filter and ICCD camera. Ten phase-delayed images were acquired by incrementally delaying the gain of the ICCD camera with respect to the modulated laser. A set of three repeated phase delayed images were acquired at each time point. The phase-delayed phosphorescence intensity images were smoothed using a 3 pixel isotropic filter and used to measure the phosphorescence lifetime at each pixel by a frequency-domain approach [47]. r $PO_2$  was then calculated from the phosphorescence lifetime using the Stern-Volmer equation and an r $PO_2$  image was generated

$$PO_2 = \frac{1}{\kappa_Q} \left( \frac{1}{\tau} - \frac{1}{\tau_0} \right)$$

where  $\tau$  ( $\mu s$ ) is the phosphorescence lifetime,  $\kappa_Q$  ( $1/\text{mmHg } \mu s$ ) is the quenching constant for the triplet-state phosphorescence probe, and  $\tau_0$  is the lifetime in a zero oxygen environment.

A region of interest (ROI) of approximately 3 mm diameter centered around the imaged area was selected and the mean rPO<sub>2</sub> within the ROI was measured. Then, the mean and standard deviation (SD) of rPO<sub>2</sub> over three repeated measurements was calculated. All image processing was performed using customized image analysis algorithms developed in Matlab (Mathworks, Natick, MA).

### 5.2.3. Statistics

A two-sided dependent T test was performed between each stage across all rats. Values are reported as mean  $\pm$  standard deviation and p-values are considered significant when  $p < 0.05$ . Correction for multiple comparisons was made using a Bonferroni procedure to control the familywise error rate. Cohen's d-value is reported as well along side all statistical tests.

## 5.3. Results

rPO<sub>2</sub> across the rat cohort was found to be  $31.1 \pm 2.0$  mmHg at baseline and  $29.8 \pm 11.4$  mmHg at the first LNAME time point, and finally dropping to  $24.9 \pm 2.4$  mmHg at the final time point. A significant change was observed between baseline and the final time point of L-NAME ( $p = 0.045$ ,  $d = 2.94$ ). No significant change was observed between any other time points. Values are summarized in fig. 5.2.

## 5.4. Discussion

A significant change was observed between baseline and LNAME using this phosphorescence procedure. This method shows a significant change relative to baseline following L-NAME.

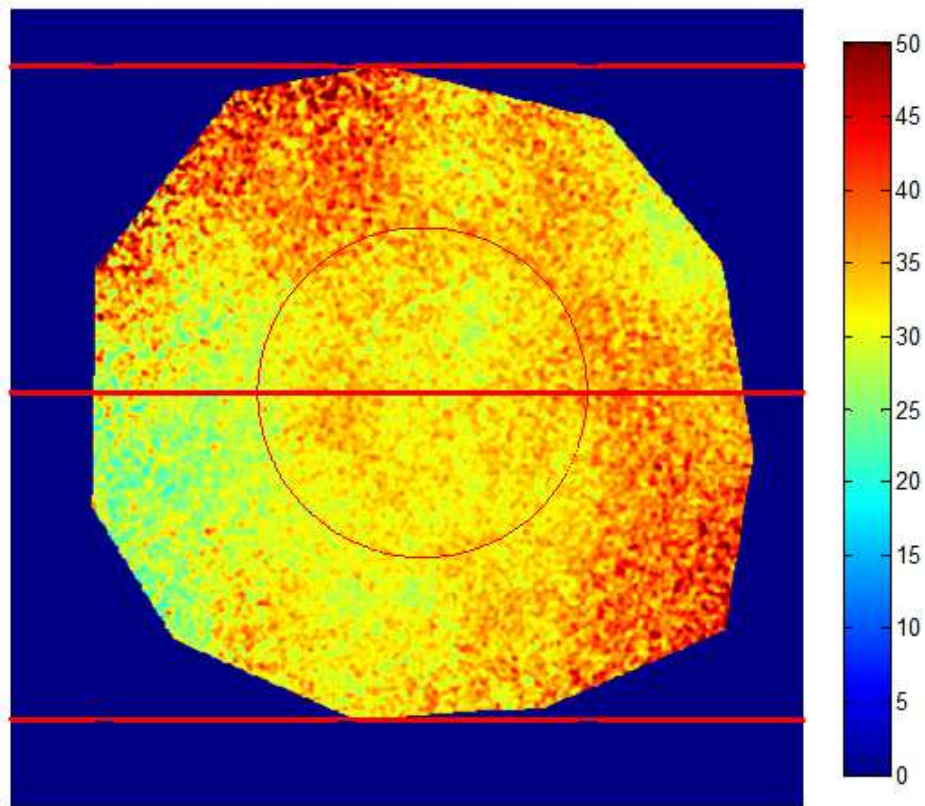


Figure 5.1. Example phosphorescence lifetime image. Each pixel shows the local  $\text{PO}_2$  (mmHg). The center red circle shows the region of interest used in the study.

#### 5.4.1. Comparison to BOLD $\text{PO}_2$

In chapter 4, a method for converting non-invasive BOLD MRI derived  $\text{PO}_2$  ( $\text{bPO}_2$ ) estimates was reported. Figure 5.2 shows the summarized data from this study next to the  $\text{bPO}_2$  estimates.  $\text{bPO}_2$  did not reach significance between baseline and LNAME, though it did show a downward trend, this may be a limitation in the sensitivity of the BOLD model. However, it was assumed that fractional blood volume does not change between baseline and following LNAME. LNAME is known to reduce fractional blood

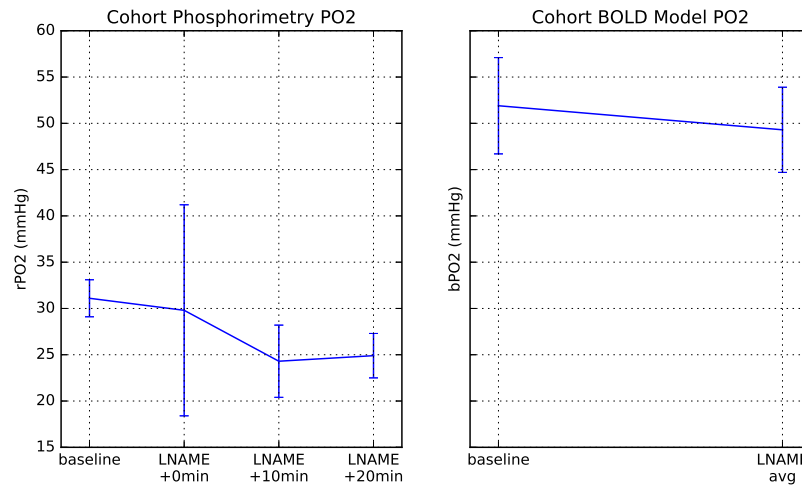


Figure 5.2. Summary plots from this study and the previous BOLD PO<sub>2</sub> model study.

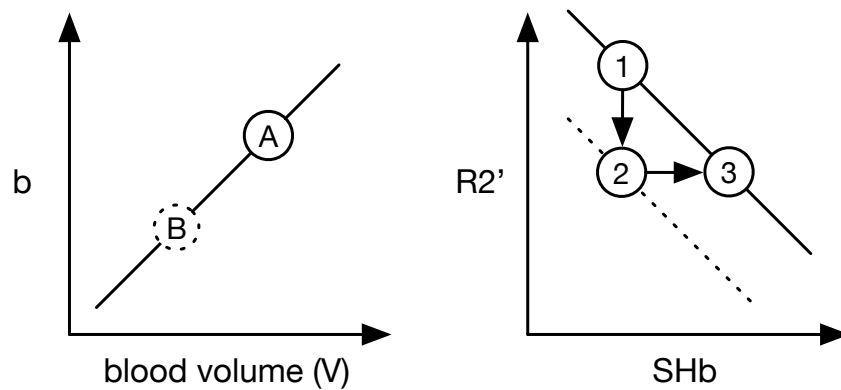


Figure 5.3. Example of how not factoring in the blood volume change into the model could lead it to misrepresent the actual change taking place.

volume through vasoconstrictive mechanisms. Decreased oxygenation will increase  $R2'$ , however decreased fractional blood volume will decrease  $R2'$ , muting the affect if blood volume changes are not accounted for. Figure 5.3 gives a more detailed explanation on the mechanism for this.

$R2'$  exhibits a linear relationship with SHb according to the statistical model. Zhang et al showed that increases in blood volume results in a roughly linear increase in expected  $R2'$  [110]. Thus, increases in blood volume can be modeled as an increase in the y-intercept of the linear  $R2'$ -SHb model. Assume a model as such

$$R2' = mSHb + b$$

A decrease in blood volume (with everything else held constant), reduces the  $R2'$  required for a given SHb (A to B in left figure and solid to dashed line in the right). If a drug is given that reduces the blood volume, but the model is not updated to account for this, then the decreased  $R2'$  will actually look like an increased SHb.

For example, at baseline  $R2'$  is measured at 1, then a drug is given that reduces blood volume but actual SHb is unchanged. The actual  $R2'$  (dotted line) that should be measured is shown at 2 since SHb has not changed. However, since the model (solid line) was not updated to account for the change in blood volume, the calculated SHb will be 3. Thus it will appear as though the drug increased SHb when in reality it had no effect on SHb.

LNAME reduces blood volume like the previous example. However, it will also lead to a decrease in SHb, since tissue  $O_2$  demand will remain relatively constant. A decrease in SHb (with everything else held constant) should result in an increased  $R2'$ . It was shown that not taking blood volume into account will appear as an increased SHb. In the case of LNAME, blood volume decreases and SHb decreases (a real increase in  $R2'$ ). The effect of the drug will be muted if the blood volume change is not factored into the model. This is due to the increase in apparent SHb from the unmodeled blood change

and the decrease in actual SHb. One method of estimating fractional blood volume is to use an intravascular contrast agent and calculate changes in relative signal and normalize them to those in blood [59].

At baseline,  $bPO_2$  was  $51.9 \pm 5.2$  mmHg, which is higher than  $rPO_2$ . Johannes et. al performed a  $FiO_2$  study using phosphorimetry and found  $PO_2$  at baseline ( $FiO_2 = 0.20$ ) varied with analysis technique but was  $45 \pm 6$  mmHg using the standard mono-exponential and  $61 \pm 9$  mmHg using a rectangular distribution. Thus, the method of analysis could potentially account for this discrepancy. On the other hand, using measured fractional blood volume and hematocrit may improve the  $bPO_2$  estimate.

The penetration depth of the laser is less than 1 mm from the surface of the kidney.  $bPO_2$  encompasses a higher depth of penetration than  $rPO_2$ . BOLD measurements are also subject to partial volume effects with the medulla, which may conflate the changes seen in the BOLD study. In order to perform a more accurate comparison between this study and the previous, it may be important to select cortical regions that match the penetration depth of this technique.

Overall, these preliminary data with phosphorescence lifetime are promising and in combination with measured fractional blood volume and hematocrit values, may provide a mechanism for calibrating BOLD derived blood  $PO_2$  estimates.

## CHAPTER 6

**Direct Assessment: R2' Renal Mapping****6.1. Introduction**

Unlike other organs, renal oxygenation does not track blood flow [85]. Increased renal blood flow (RBF) can lead to an increase in the glomerular filtration rate (GFR), which in turn leads to an increase in the sodium load in the tubules. This results in an increased demand for oxygen to support increased sodium reabsorption. Thus an increase in RBF can lead to a concomitant increase in oxygen demand, leaving the tissue oxygenation unchanged. Due to this disconnect in the relationship between blood flow and oxygenation in the kidney, direct assessment of oxygenation is highly desired. Currently there are no non-invasive methods to assess intra-renal oxygenation in humans other than blood oxygenation level dependent (BOLD) MRI.

Renal oxygenation is also not homogeneous. The renal medulla in mammals is relatively hypoxic in relation to the cortex. The medulla receives a lower amount of blood flow compared to the cortex. Additionally, a high rate of oxygen consumption required for active reabsorption of sodium in the medullary thick ascending limb and shunting between the arterial and venous system in the vasa recta render medullary  $PO_2$  at about half that of the cortical region [12]. Medullary hypoxia is now well accepted to be a key factor in the development of acute renal failure and also has been shown to play a role in the

---

Originally published as Thacker J, Tan H, Prasad PV. "R2' Renal Mapping". 2nd International Workshop on MRI Phase Contrast and Quantitative Susceptibility Mapping 2013, Ithaca, NY.

pathophysiology of hypertension, diabetic nephropathy and contrast-induced nephropathy [15, 23, 36, 38]. Renal oxygenation is an important measure of renal parenchyma health and renal hypoxia is now considered to be a key contributor to chronic kidney disease (CKD) progression [39], [27].

BOLD MRI is sensitive to the changes in magnetic susceptibility of blood (hemoglobin), depending on its oxygenation status and has been used extensively for assessing renal oxygenation [112]. Gradient echo (GRE) sequences have been widely used to measure  $R2^*$  relaxation [81], [79]. However, as recent studies have shown,  $R2^*$  measurements are not specific to oxygenation changes because of the inherent  $R2$  dependence, which is sensitive to water content [100]. This will likely result in confounded results when determining renal oxygenation status under varying hydration levels. While  $R2^*$  is effective at monitoring changes in oxygenation, it is not possible to directly translate  $R2^*$  to blood  $PO_2$ .  $R2'$  is thought to be the sum of two components:  $R2^*$  and  $R2$ , with  $R2'$  being primarily responsible for the susceptibility variation due to changes in red blood cell oxygen saturation [106]. The current method of assessing  $R2'$  in the kidney is by subtracting  $R2$  from  $R2^*$  [107], we seek to measure it directly.

Asymmetric spin echo (ASE) allows for direct assessment of  $R2'$  and has been shown to be sensitive to changes in oxygenation in human kidneys [113]. Combining ASE with a model of the magnetic properties of oxygenated and deoxygenated hemoglobin (oxy-Hb and deoxy-Hb respectively), the fractional oxygen saturation of red blood cells (sHb) as well as the venous blood volume can be estimated non-invasively [92]. This has recently been shown to be feasible in the human brain [2].

Previous studies in kidneys acquired different  $\tau$  values during a single breath-hold scan [113], which is limited for widespread application due to the long breath-hold interval. This interval also determines how many  $\tau$  values can be sampled each breath-hold. By using a navigator-gated acquisition, the constraint on the number of phase encodings and  $\tau$  values is lifted. In this study, we have implemented a navigator-gated, multi-shot (segmented) ASE sequence to facilitate free-breathing scans, improved spatial resolution and allow for an arbitrary number of values to be acquired.

## 6.2. Methods

We used a 2D navigator to trigger data acquisition based on respiration. The navigator plane was positioned over the lung-liver interface in the coronal plane to estimate kidney motion. Each 2D navigator image was reduced to a one-dimensional image, with the dark band representing the diaphragmatic level, see fig. 6.1.

ASE-EPI image acquisitions were triggered during expiration (apex of the navigator profile). We used  $\tau$  values ranging from 15 ms to 27.75 ms in steps of 0.75ms resulting in 18 images. The signal intensity was fit to the equation

$$S(\tau) = S_0 \exp(-2R_2'\tau)$$

to estimate  $R_2'$  for each voxel. An interleaved, 2-shot Cartesian EPI readout trajectory was used. Further imaging parameters are as follows: effective TE=65ms, FOV=250mm x 250mm, Matrix=128 x 112, Slice Thickness=6mm, Bandwidth =1149 Hz/Pixel. The repetition time was dependent on the breathing profile of the subject due to the gating, but it was at least 2.5s for each acquisition. Images were acquired in the axial plane

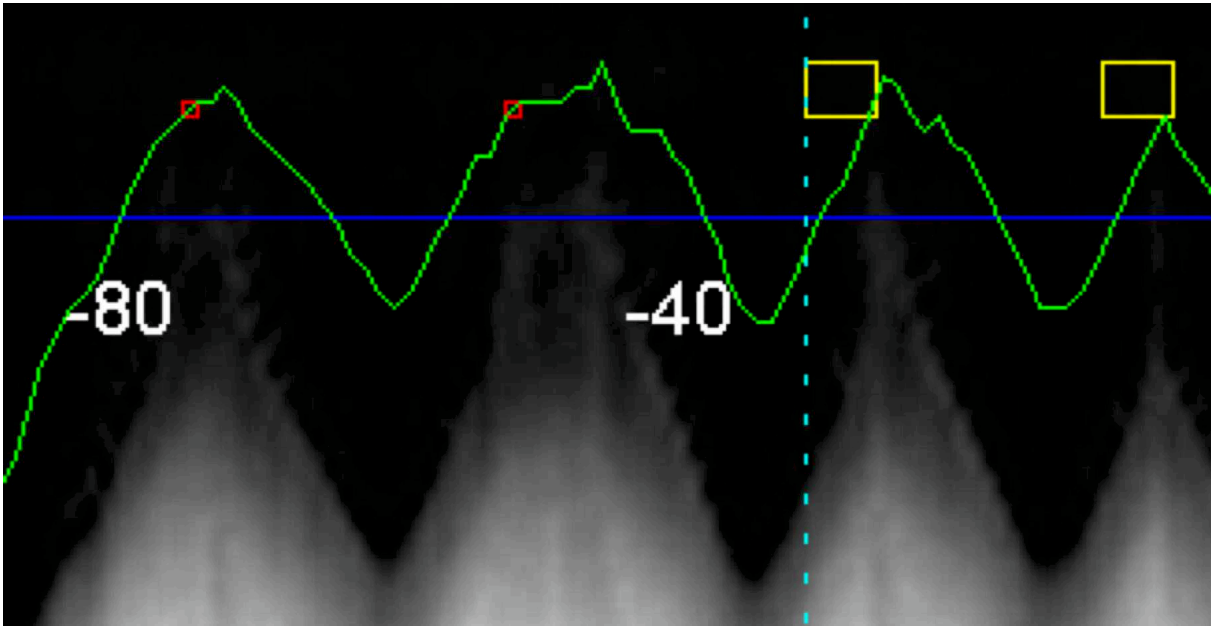


Figure 6.1. Example navigator gated profile. The dark region is the lung and the bright region is the liver. Yellow boxes indicate the windows of acquisition.

and subjects were positioned in the iso-center of the magnet to help minimize any static magnetic field inhomogeneities across the field of view.

After the data was acquired, the images were reconstructed to  $256 \times 224$  by interpolation. All experiments were performed on a 3T MRI system (MAGNETOM Verio, Siemens Healthcare, Erlangen, Germany) using the body and spine phased array coil. Regions of interest (ROI) were drawn around the cortex and medulla to extract averaged  $R2'$  values. The positioning of these was based on anatomic spin echo images ( $\tau = 0$ ). The ROI were then copied to the derived  $R2'$  maps to compute average values for the regions. This acquisition was acquired in 5 healthy volunteers.

Furthermore, three subjects were imaged before and after furosemide administration to estimate for each. Representative ROI were drawn in the cortex and medulla for each

kidney in the same manor for the non-furosemide volunteers.  $R2'$  was then estimated as  $\Delta R2' = R2'(\text{post}) - R2'(\text{pre})$ .

$R2'$  can be related to blood oxygen saturation as such

$$R2' = \lambda \delta\omega = \lambda \frac{4}{3} \pi \gamma B_0 \Delta\chi \text{Hct} (1 - \text{sHb})$$

where  $\delta\omega$  is the frequency perturbation of the partially saturated RBCs,  $\lambda$  is the blood volume with the perturbers in it,  $\Delta\chi$  is the susceptibility difference between fully deoxygenated and fully oxygenated RBCs. Once  $R2'$  is estimated,  $\lambda$  can be estimated by extrapolating the  $R2'$  curve back to the origin and taking the log difference between that point and a spin echo image [2].

Average  $R2'$  values from the 5 volunteers in the cortex and medulla were found to be  $10.09 \pm 5.41s^{-1}$  and  $17.38 \pm 8.49s^{-1}$ , respectively. These values are consistent with the previous report [113].

Figure 6.3 shows an example of an image from the same subject at both the single-shot matrix size of 64x56 and the segmented version of 128x112. Figure 6.4 show representative plots of signal vs.  $\tau$ . For the subjects undergoing furosemide administration,  $\Delta R2'$  in the cortex and medulla was found to be  $-0.23 \pm 2.58s^{-1}$  and  $7.28 \pm 1.62s^{-1}$ , respectively. A significant change was observed in the medulla ( $p < 0.05$ ) but not in the cortex ( $p > 0.05$ ).

### 6.3. Discussion

Our preliminary data presented here do support the feasibility of the proposed  $R2'$  mapping method. By employing a segmented acquisition, we were able to increase the effective resolution of the acquisition and potentially increase the discrimination between

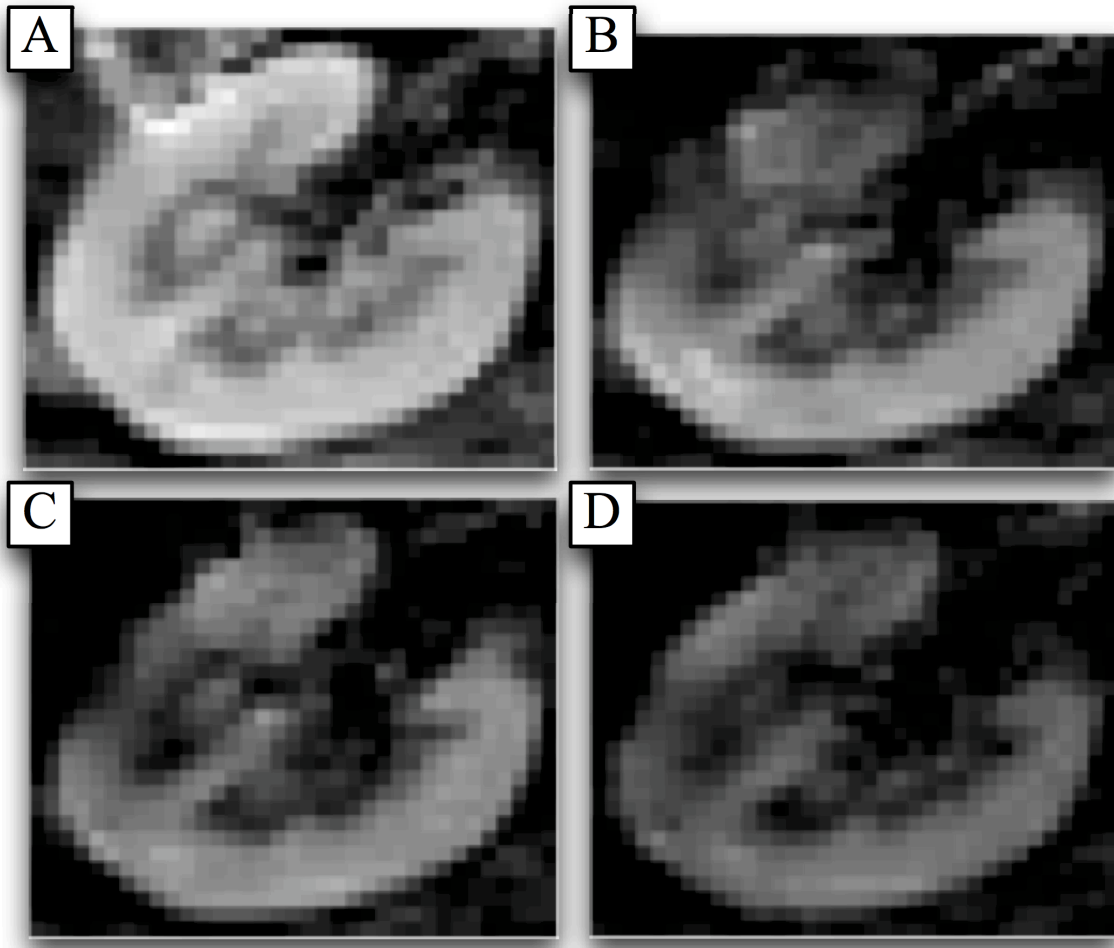


Figure 6.2. Example ASE echo images. (A)  $\tau = 0$  ms, (B)  $\tau = 15$  ms, (C)  $\tau = 21$  ms, (D)  $\tau = 27$  ms.

the cortical and medullary regions of the kidney. A segmented scan allows for flexibility in matrix size and adapting the resolution for different FOVs. The drawback of this method is that acquisition time increases and imaging all  $\tau$  values in a single breath-hold is no longer feasible.

$\Delta R2'$  was found to change in the medulla but not in the cortex which agrees with what we would expect following furosemide injection. Oxygenation is expected to increase in

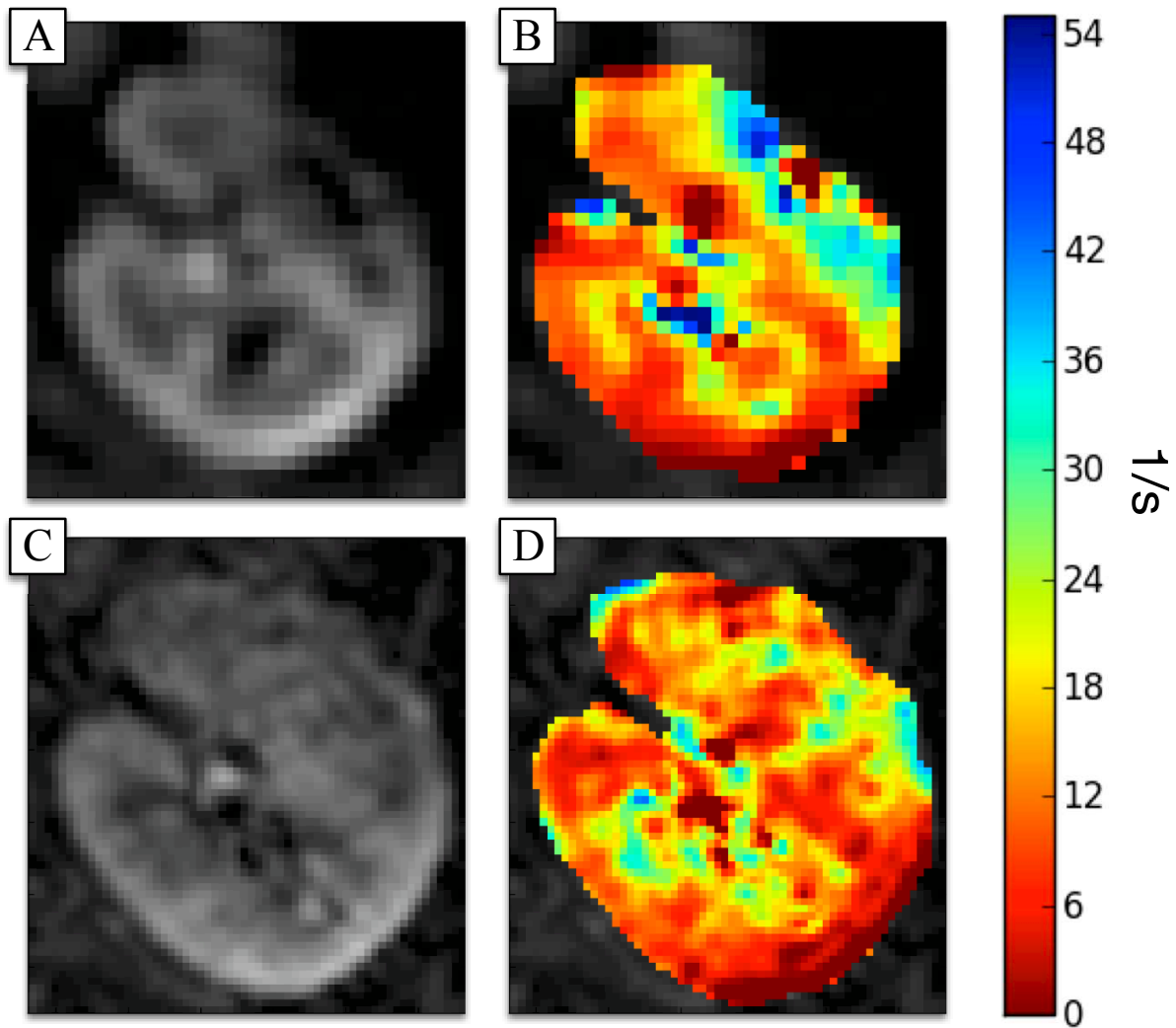


Figure 6.3. Representative  $R2'$  map for segmented and single-shot EPI readouts. (A) Single shot,  $\tau = 15$  ms (B) Single shot,  $R2'$  map (C) Segmented,  $\tau = 15$  ms, (D) Segmented,  $R2'$  map.

the medulla but not the cortex since furosemide is a loop diuretic, acting on the thick ascending limb of the loop of henle within the medulla. ASE-EPI sequences can also be used to estimate blood oxygen saturation since they can simultaneously estimate and venous blood volume. sHb also depends upon the blood hematocrit which has been shown

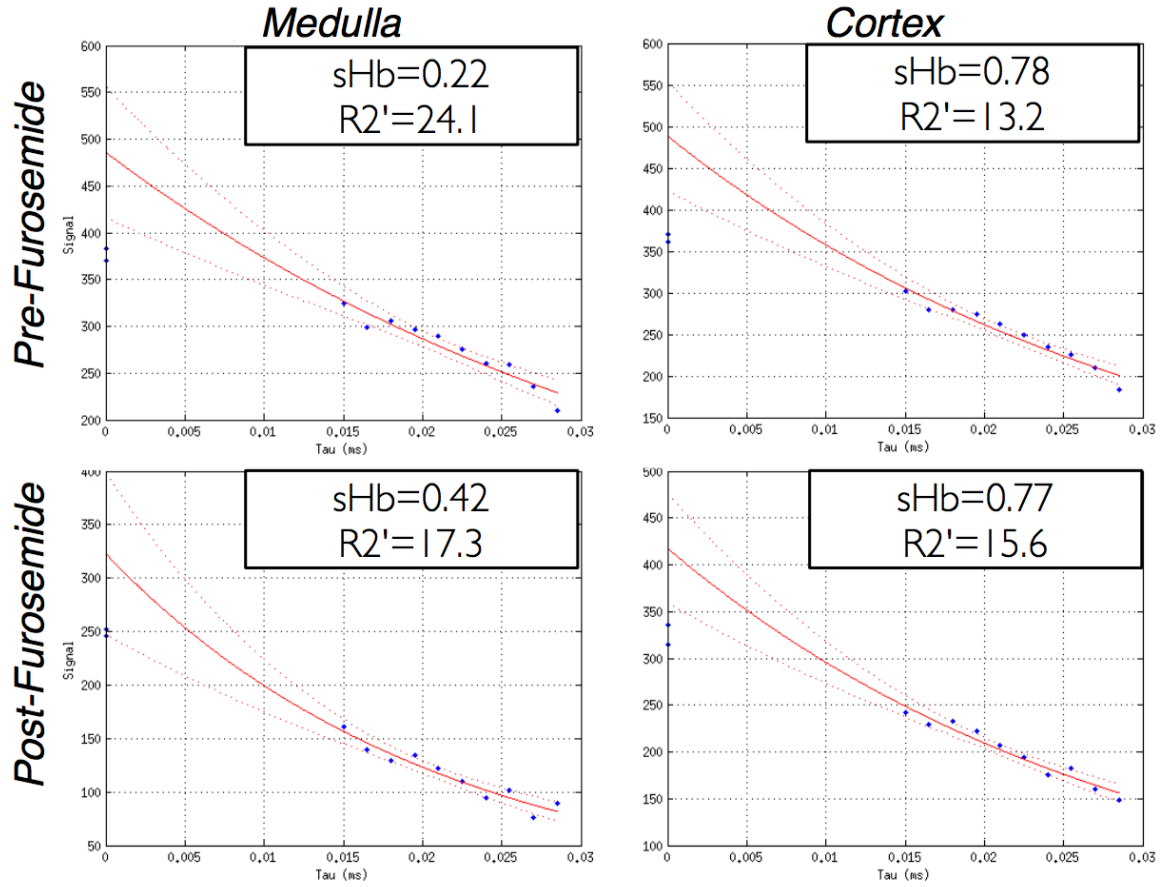


Figure 6.4. Example  $R2'$  decay curves for a subject at baseline and after furosemide administration.

to vary between the medulla and cortex [115]. This regional difference will need to be taken into account when using ASE-EPI sequences for estimating sHb.

#### 6.4. Conclusions

Navigator gated, segmented ASE-EPI sequences provide several benefits over previously demonstrated methods. Navigator gating allows for data to be acquired while subjects are freely breathing, increasing their comfort and potentially allow multi-slice

imaging. A navigator gated scan further allows for an unconstrained number of different  $\tau$  values to be acquired which should increase the quality of the  $R2'$  curve fitting. By segmenting the EPI readout train, higher spatial resolutions are achievable and allow for better differentiation between the anatomical structures of the kidney without increasing the effective TE and hence compromising SNR. Parallel imaging and partial Fourier encoding are two other techniques that can be used to improve resolution, though at the cost of SNR.

## CHAPTER 7

## Arterial Spin Labeling Perfusion Sensitivity to Pharmacologically Induced Perfusion Changes

### 7.1. Introduction

In recent years, non-contrast functional MRI approaches (e.g. BOLD, diffusion, perfusion) applied to kidneys are becoming accepted to evaluate renal structure and function [109], which now play a key role in translational research [55]. This includes arterial spin labeling (ASL), a non-invasive MRI technique that uses water molecules in blood as an endogenous tracer to assess tissue perfusion. ASL has been validated in both humans [86] and animal [4] models to provide quantitative assessment of renal tissue blood flow. Recently, perfusion estimates in human with ASL were shown to demonstrate significant differences between healthy and patients with chronic kidney disease (CKD) [95]. Reduced blood flow is implicated in the initiation and progression of CKD [29] and contrast enhanced perfusion MRI measurements are not feasible in patients with compromised renal function due to the risk of developing nephrogenic systemic fibrosis [66]. ASL thus provides a feasible solution to this problem.

Small animal models are often used to provide better understanding of the pathophysiology of the disease and its progression [16]. Compared to human and large animals, the

---

Originally published as H. Tan, J. Thacker, T. Franklin, and P. V. Prasad, "Sensitivity of arterial spin labeling perfusion MRI to pharmacologically induced perfusion changes in rat kidneys," *Journal of Magnetic Resonance Imaging* 41.4 (2015) 1124-1128.

smaller anatomical size of the kidneys in rats and/or mice makes the existing challenges in ASL such as peristaltic and respiratory motion, perfusion sensitivity, and susceptibility artifacts arising from air-tissue interface in the abdomen more severe. Despite these technical difficulties, several studies have shown the initial feasibility of ASL in small animal models. ASL was shown to detect abnormal perfusion in a rat model of acute kidney injury [114] and transplanted kidneys [101]. Recently, Rajendran et al. investigated the implementation and feasibility of ASL 7T in mice [84].

An inherent requirement of functional methods is to show acute changes following a physiological or pharmacological stimuli [60]. In this study, we investigated whether ASL perfusion imaging has sufficient sensitivity to changes induced by pharmacological stimuli at commonly used doses [93].

## 7.2. Methods

All animal handling and experiments were conducted under a protocol approved by the local Institutional Animal Care and Use Committee (IACUC) and in accordance with animal welfare regulations. A total of 7 Sprague Dawley rats were examined in this study.

### 7.2.1. Animal Preparation

Seven rats with weights ranging from 368 to 521 grams were obtained from Charles River (Chicago, IL) and housed at the institutional animal care facility. The animals were fed with standard rodent chow and water ad libitum. A catheter (PE-50) was placed in the femoral vein for administration of vasoactive drugs. All procedures were conducted under

anesthesia using Inactin (thiobutabarbital sodium, 100 mg/kg i.p., Sigma-Aldrich, St. Louis, MO).

### **7.2.2. Pharmacological Agents**

Adenosine and L-NAME (Sigma-Aldrich) were chosen in this study to induce renal blood flow changes based on prior experience with these agents [93]. Adenosine is an endogenous nucleoside known to stimulate a variety of vascular receptors in the kidneys. The effect of adenosine is vasodilation when administered as intravenous infusion [37]. The duration of action of adenosine is very short [7], and thus can be used repeatedly. L-NAME, a synthetic nitric oxide synthase inhibitor, was used for vasoconstriction [53, 56]. The duration of action for L-NAME is greater than 2 hours [102].

### **7.2.3. Perfusion Study Design**

In this study, adenosine was formulated from 200 mg/kg adenosine hemisulfate salt and dissolved in 10 mL saline. An infusion pump was used to infuse the dissolved adenosine with a rate of 0.05 mL/min resulting in a dose rate of 1 mg/kg/min. L-NAME was administered into the femoral vein as a 10 mg/kg(body weight) bolus. Due to the rapid onset and short duration of response for adenosine [7] and the long duration of action of L-NAME [102], six perfusion measurements were made in the order illustrated in fig. 7.1. The Adenosine infusion was alternated between baseline (OFF) and vasodilation (ON) to test the reproducibility of the observed response. Adenosine infusion and L-NAME injection were started 10 15 minutes prior to the start of ASL imaging.

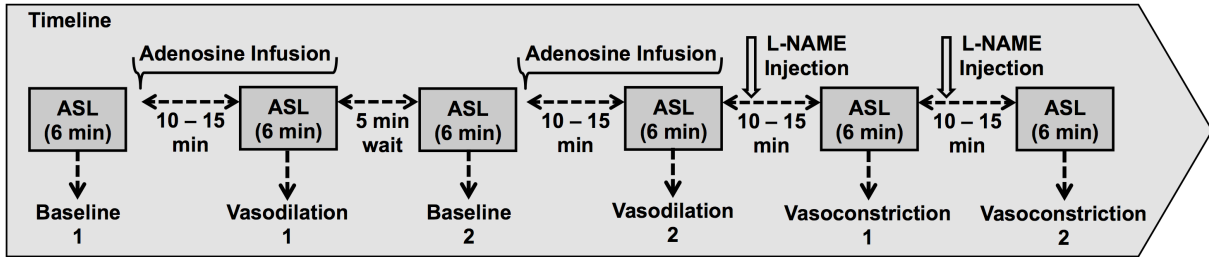


Figure 7.1. Experimental design. Baseline and vasodilation scans were repeated to assess reproducibility. The vasoconstriction scans were repeated to study the cumulative effects of L-NAME.

#### 7.2.4. Imaging Protocol and Perfusion Quantification

All imaging studies were performed on a Siemens 3T scanner (MAGNETOM Verio, Siemens HealthCare, Erlangen, Germany) with an eight-channel knee coil (Siemens HealthCare) for data collection. Each animal was placed on a cushion at the center of the knee coil in a right lateral decubitus position during imaging. ASL sequence was implemented with a flow-sensitive alternating inversion recovery (FAIR) (19) preparation and a balanced steady state free precession (TrueFISP) readout [67, 95]. Imaging parameters were: FOV/TE/TR = 83mm/2.5ms/6s; flip angle = 60; slice thickness = 4.5 mm; averages = 30; imaging matrix = 128 x 78 (frequency x phase); post labeling delay = 1.2s; labeling band thickness = 10mm; bandwidth = 651 Hz/Px. A selective inversion band thickness of 8mm was used to ensure proper tagging efficiency. A linear ramp catalyzation pulse was used for the TrueFISP readout. 30 control and label pairs were acquired in 6 minutes of scan time. A proton density weighted image was acquired with the same TrueFISP readout immediately following the FAIR-TrueFISP scan with a TR = 10s for perfusion quantification. Raw data was transferred for offline post-processing using MATLAB (MathWorks, Natick, MA). Images were first aligned using FMRIB's

Linear Image Registration Tool (FLIRT, FMRIB, Oxford, United Kingdom) [42] with the first image in the perfusion series as the reference. The difference images obtained by subtracting the control from the label images were averaged into a single perfusion weighted image. Quantitative renal blood flow maps (RBF) were then calculated using a single compartment model on voxel to voxel basis

$$f = \frac{\lambda}{2\alpha\text{TI}} \frac{\Delta M}{M_0} \exp\left(\frac{\text{TI}}{T_1}\right)$$

where  $f$  is the perfusion rate (in the unit of ml/100g/min),  $\lambda$  is the blood-tissue water partition coefficient, which is assumed to be 80 ml/100g [46],  $\alpha$  is the inversion efficiency which is assumed to be 0.95,  $\Delta M$  is the perfusion weighted image,  $M_0$  is the equilibrium magnetization of the tissue (proton density).  $\text{TI}=1.2\text{s}$  is the post labeling delay time [114].  $T_1$  of 1.14 sec is assumed for the renal cortex [17].

### 7.2.5. Data Analysis

Mean perfusion rates were calculated by manual selection of region-of-interests (ROI) on RBF maps. ROIs were defined in the renal cortex for both kidneys. Renal arteries were carefully excluded in the ROIs. Only one kidney was imaged in three rats due to the different lateral position of the kidneys. A total of 11 kidneys were used in the final analysis. The effects of Adenosine and L-NAME were analyzed using paired t-tests. A p-value of 0.05 is considered to indicate significance. The reproducibility of the baseline and Adenosine scans were assessed using coefficient of variations (CV).

### 7.3. Results

An illustration of the representative RBF map for each condition is shown in fig. 7.2. Renal cortex can be clearly distinguished from the renal medulla in baseline and vasodilation scans. Retrospective motion correction and signal averaging were sufficient to minimize motion artifacts and the final RBF maps were of sufficient quality for analysis. One rat died during data acquisition after the first L-NAME injection. The data analysis on the effects of L-NAME was hence based on only 6 animals. The mean and the standard deviation of the cortical perfusion rates are shown in Figure 3. The baseline perfusion rates for the cortical tissue were similar to reported values in previously reported studies (9,11). Vasodilation with Adenosine resulted in an average of 94 ml/100g/min increase in perfusion (26% increase) compared to baseline; and vasoconstriction with L-NAME lowered the cortical perfusion by an average of 145 ml/100g/min after the first injection of L-NAME (36% decrease) compared to baseline. The cortical perfusion further dropped an average of 40 ml/100g/min following the second L-NAME injection (46% decrease compared to the baseline). The perfusion rate drop between the first and second L-NAME injection ( $p < 0.05$ ) is consistent with the long action times. The changes in perfusion rate were significant between baseline and vasodilation ( $p < 0.05$ ), baseline and vasoconstriction ( $p < 0.01$ ), and vasodilation and vasoconstriction ( $p < 0.01$ ). The coefficients of variations were 4% and 11.6% for baseline and adenosine measurements, respectively, indicating good reproducibility.

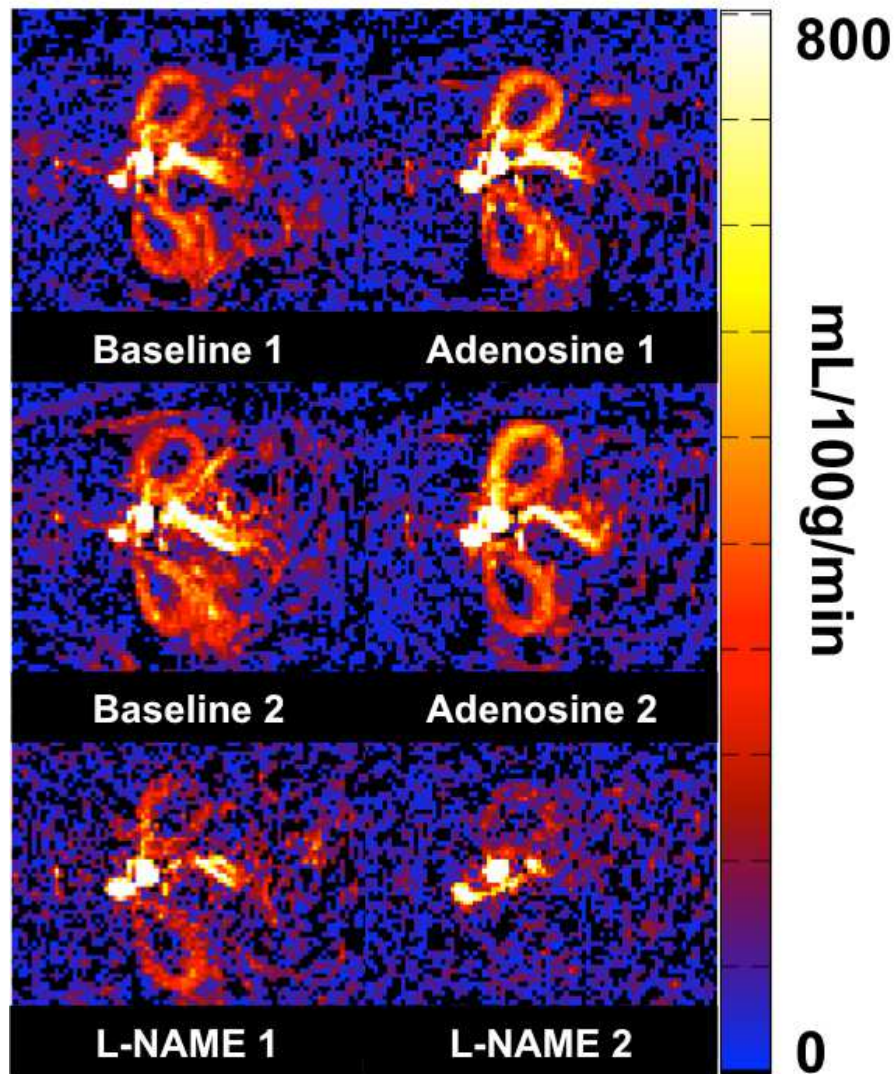


Figure 7.2. Representative renal blood flow maps of rat kidneys at each experimental condition. Note the increased cortical perfusion with adenosine infusion and the decreased cortical perfusion with L-NAME injection

#### 7.4. Discussion

In this study, feasibility of FAIR ASL to obtain quantitative renal perfusion measurement on a clinical 3T scanner in a rodent model was demonstrated. Furthermore, we

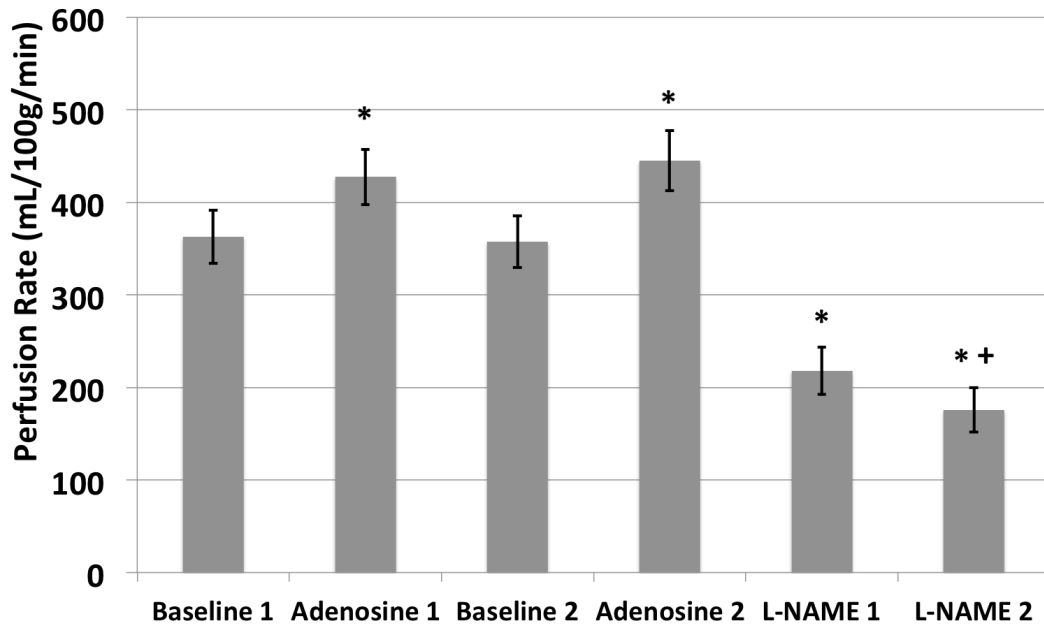


Figure 7.3. Comparisons of quantitative perfusion rates. Note the return to baseline perfusion values when the infusion of Adenosine was stopped. The increase in perfusion is comparable after each dose, and is statistically significant compared to the baseline. On the other hand, administration of L-NAME results in significant reduction in perfusion compared to baseline. Following the second administration, there is further significant reduction in perfusion. No significance difference was observed between the two baseline, as well as Adenosine scans. \* indicates significant difference ( $p < 0.05$ ) comparing to the corresponding baseline scans. + indicates significant difference ( $p < 0.05$ ) comparing to the first L-NAME scan

have shown that FAIR-ASL was sensitive to variations in renal perfusion caused by pharmacologically induced vasodilation and vasoconstriction. The findings suggest that it is feasible to use ASL to investigate various effects on renal blood flow in rodent models, such as contrast-induced acute kidney injury [54].

On average, the cortical perfusion increased by 26% during Adenosine infusion and decreased by 36% after the first L-NAME injection. In two animals, one of the two vasodilation scans during Adenosine infusion resulted in little or negative change in cortical perfusions (0.8% and -6% respectively). We do not know the exact cause for these observations, and can only speculate that it may be a consequence of pump malfunction, or a delayed response to the Adenosine. In a previous study, Granstam et. al [33] reported a 60% decrease in blood flow at similar dose using microsphere analysis following the L-NAME injection (dose), which was a larger change than we have observed. However, they have followed the bolus L-NAME injection with an infusion for 10 minutes at a rate of 10 mg/kg. In our study, the cortical perfusion decreased further by an average of 20% after the second L-NAME injection. This cumulative response was more consistent with the changes reported by Granstam et al.

The dosage of the vasoactive drugs in this study was chosen based on a previously published animal study using BOLD-MRI [93]. During our initial testing, we observed little (less than 3%) cortical perfusion change (data not shown) with an adenosine dose rate of 500 ug/kg/min [93]. Subsequently, we doubled the dosage of Adenosine to 1.0 mg/kg/min. As shown, the average increase in perfusion was 94 mL/100g/min during adenosine infusion and was comparable to the averaged standard deviation in the baseline perfusion measurements of 107 mL/100g/min (this excludes the two previously mentioned instances where adenosine infusion resulted in anomalously low level of change). The need for higher dose of adenosine is consistent with the known limitation in terms of sensitivity of ASL compared to contrast enhanced studies such as the previous report [93]. The response to L-NAME was more robust at the doses currently used [93].

While respiration is generally considered as a challenge for abdominal imaging, we observed very little image quality degradation. The post-processing co-registration technique was sufficient to minimize registration errors and no apparent subtraction artifacts were observed in the final perfusion maps. A thick labeling band (nearly twice the thickness as the imaging slice) was used to ensure the inversion efficiency [95]. Transit delay effect was neglected in this study. An adiabatic frequency offset corrected (FOCI) pulse [73] was used for selective inversion to partially compensate for this effect [67].

Medullary perfusion was not analyzed in this study due to the concern of partial volume effects and the poor sensitivity of FAIR ASL to the slow flow in the medulla. This was a limitation of the ASL implementation and the use of standard clinical scanner. Alternatively, the use of higher field strength magnets dedicated for small animal imaging may allow for measuring medullary perfusion facilitated by the elongated  $T_1$  of the blood and hence allowing for longer inflow time. Alternately, higher field strengths could facilitate increased spatial resolution. However, ASL may be more sensitive to motion errors that retrospective correction techniques may not provide satisfactory results and additional techniques such as respiratory triggering [84], navigators [84, 91, 95], and selective averaging [32, 96] may become necessary.

### 7.5. Conclusion

Data provided in this preliminary study support the feasibility of FAIR True-FISP based renal perfusion MRI in rat kidneys and demonstrate adequate sensitivity to pharmacological induced blood flow changes. This suggests feasibility of using the measurement in concert with techniques such as BOLD MRI in various models of ischemic injury [54, 101, 114]. Further studies are necessary to demonstrate similar sensitivity in human measurements of renal perfusion by ASL.

## CHAPTER 8

### **Conclusions**

Renal physiology plays a critical role in cardiovascular health. Kidneys expend a significant amount of energy removing metabolic waste from the blood stream, and maintaining homeostasis. It is thus not surprising that kidneys are primarily assessed by how well they filter and what they filter. Too little filtration or too much of the wrong substance (e.g. protein), are good indicators that something has gone wrong with the organ. CKD is stratified on these same grounds. Decreased filtration or increased proteinuria indicates progression of the disease. As the number of subjects with CKD increases worldwide, finding new ways to assess the disease earlier could play an important role in treating these patients and potentially stopping the progression of the disease.

Despite receiving nearly a quarter of the cardiac output, the inner medulla operates in a scant oxygen environment. When coupled with an acute injury, AKI, or a chronically hypoxic environment, CKD, may result in hypoxic injury. Better assessment of the regional oxygen environment in the kidney is critical to understanding prognosis and progression of these diseases. BOLD MRI is the only non-invasive technique (to-date) for assessing renal oxygenation in humans. However, the technique has struggled to find clinical relevance. Some of the primary causes may be the predominant subjective analysis techniques, reporting of non-physiological parameters, and multiple acquisitions required to get a reliable measurement. We have reported on techniques for addressing each of these items.

It was shown that by using the entire renal parenchyma, an objective analysis technique could be used that is not subjected to reduced cortico-medullary differentiation and reviewer bias. The technique used moments of the parenchyma  $R2^*$  distribution to look at changes following pharmaceutical agents. It was shown to have a higher inter-rater agreement than when  $R2^*$  maps were analyzed using cortical or medullary regions. It was sufficiently sensitive to detect changes in the parenchyma following furosemide administration. Post-furosemide  $R2^*$  maps were shown to exhibit a significant difference between controls and CKD subjects. The higher moments captured further changes in the  $R2^*$  distribution of each parenchyma, lending more information to the analysis than the typical mean values reported. While the technique does reduce the spatial acuity, for clinical cases the increased objectivity and ease of analysis may sufficiently make up for the loss.

The next step was to apply a statistical model to  $R2'$  measurements with the goal of estimating blood  $PO_2$ . A study was performed looking at changes in  $R2'$  following L-NAME and furosemide in a cohort of rats. Furosemide provides a regional change in  $PO_2$  by reducing the sodium reabsorption taking place in the medulla, resulting in a decrease in oxygen demand and hence an increase in blood  $PO_2$ . The model was able to capture this change and report the change as an estimated blood  $PO_2$ , instead of the usual  $R2^*$  parameter (1/s).  $R2'$  was used instead of  $R2^*$  as it removes the hydration-dependent effects observed in  $R2$ . The model takes blood volume, hematocrit, and several other parameters into account when estimating  $PO_2$ . This allows for direct comparison between regions and between MRI setups.  $R2^*$  and  $R2'$  are both sensitive to magnetic field strength and regional parameters such as hematocrit and blood volume. A follow

up study was performed to validate the findings in the MRI portion. Using an injectable oxygen probe, an optical experiment was done to observe blood  $PO_2$ . Unlike the standard invasive technique (microelectrodes), the oxygen probe is constrained to the vasculature. This allows measurements of this compartment separate from the tissue space. The limitation of this approach is that the penetration depth of the probe is not sufficient to reach the medulla, only allowing the cortex to be assessed. The technique was found to be sensitive to changes in  $PO_2$  following LNAME, although the absolute values were lower than expected.

$R2'$  is believed to be more specific to oxygenation changes than  $R2^*$ , as it removes the  $R2$  component that can be heavily skewed by hydration status. In the previous study,  $R2'$  was determined indirectly by subtracting  $R2$  from  $R2^*$ . Each of which was derived from a separate scan. We showed that an asymmetric spin echo sequence could be combined with a navigator to enable direct assessment of  $R2'$ . This was combined with a segmented EPI readout to enable higher spatial resolutions without increasing the effective echo time, which would reduce the SNR.

Finally a report was made on the use of ASL in rats and the effects of certain pharmacological agents. In chapter 4 the confounding factors of blood volume and hematocrit were discussed. That study only estimated the blood  $PO_2$ , but the value of critical importance is the tissue  $PO_2$ . While there are more unknown parameters that go into determining the tissue  $PO_2$  even once blood  $PO_2$  is known, blood perfusion is a key factor. Using a non-invasive technique like ASL may provide the information required to remove an assumed perfusion value, making the estimated values match closer to reality. Additionally, changes in perfusion may result from changes in blood volume (a key factor

in estimating blood  $PO_2$  from BOLD MRI data) and may be used as a surrogate for such changes. A preliminary study was done to assess the feasibility of performing FAIR True-FISP based renal perfusion MRI in rat kidneys. It was shown that the technique is sensitive to pharmaceutical agents, such as L-NAME, which was used in the previous studies. Perfusion in the medulla is quite low and this technique may not be adequate for measuring values at this extreme.

Each of the studies outlined here have worked towards making BOLD MRI a viable tool for assessing renal  $PO_2$  non-invasively and potentially increasing the clinical utility. The next step is to combine all methods together. Chapter 4 found  $R2'$  by subtracting  $R2$  from  $R2^*$ , but the ASE method can provide  $R2'$  directly. ASE also provides an estimate of blood volume, which is another assumed value in the BOLD MRI  $PO_2$  model. The whole kidney moment analysis technique could be used for analyzing the BOLD MRI derived  $PO_2$  maps. Although, this would require first creating regional maps of literature estimates for hematocrit, blood volume, and other values. Fair True-FISP based ASL can be used to estimate perfusion and get an estimate of tissue  $PO_2$ . To fully understand the effect of the parameters on the statistical model, it will be important to study each one independently. The effects of just a blood volume change as compared to the effects of a change in oxygen demand need to be independently investigated and validated against the model.

## References

- [1] AGMON, Y., PELEG, H., GREENFELD, Z., ROSEN, S., AND BREZIS, M. Nitric oxide and prostanoids protect the renal outer medulla from radiocontrast toxicity in the rat. *Journal of Clinical Investigation* 94, 3 (1994), 1069–75.
- [2] AN, H., AND LIN, W. Impact of intravascular signal on quantitative measures of cerebral oxygen extraction and blood volume under normo- and hypercapnic conditions using an asymmetric spin echo approach. *Magnetic resonance in medicine : official journal of the Society of Magnetic Resonance in Medicine / Society of Magnetic Resonance in Medicine* 50, 4 (oct 2003), 708–16.
- [3] ARMSTRONG, J. Urinalysis in Western culture: a brief history. *Kidney international* 71, 5 (2007), 384–387.
- [4] ARTZ, N., WENTLAND, A., SADOWSKI, E., DJAMALI, A., GRIST, T., SEO, S., AND FAIN, S. Comparing Kidney Perfusion Using Noncontrast Arterial Spin Labeling MRI and Microsphere Methods in an Interventional Swine Model. *Investigative Radiology* 46, 2 (2011), 124–131.
- [5] AUKLAND, K., AND KROG, J. Renal oxygen tension. *Nature* 188 (1960), 671.
- [6] BELLOMO, R., KELLUM, J. A., AND RONCO, C. Acute kidney injury. *Lancet* 380, 9843 (aug 2012), 756–66.
- [7] BIAGGIONI, I. Clinical and molecular pharmacologic characteristics of adenosine-induced vasodilation. *Clinical pharmacology and therapeutics* 75, 3 (2004), 137.
- [8] BIRO, G. P. From the Atmosphere to Mitochondrion: The Oxygen Cascade. *Hemoglobin-Based Oxygen Carriers as Red Cell Substitutes and Oxygen Therapeutics 9783642407* (2013), 27–53.
- [9] BOSS, A., MARTIROSIAN, P., JEHS, M. C., DIETZ, K., ALBER, M., ROSSI, C., CLAUSSEN, C. D., AND SCHICK, F. Influence of oxygen and carbogen breathing on renal oxygenation measured by T2\*-weighted imaging at 3.0 T. *NMR in Biomedicine* 22, 6 (2009), 638–645.

- [10] BOWMAN, W. On the Structure and Use of the Malpighian Bodies of the Kidney, with Observations on the Circulation through that Gland. *Philosophical Transactions* 32 (1842), 57–80.
- [11] BREZIS, M., AGMON, Y., AND EPSTEIN, F. H. Determinants of intrarenal oxygenation. I. Effects of diuretics. *The American journal of physiology* 267, 6 Pt 2 (1994), F1063–F1068.
- [12] BREZIS, M., ROSEN, S. N., AND EPSTEIN, F. H. The pathophysiological implications of medullary hypoxia. *American journal of kidney diseases: the official journal of the National Kidney Foundation* 13, 3 (1989), 253.
- [13] BYRNE, A. L., BENNETT, M., CHATTERJI, R., SYMONS, R., PACE, N. L., AND THOMAS, P. S. Peripheral venous and arterial blood gas analysis in adults: Are they comparable? A systematic review and meta-analysis. *Respirology* 19, 2 (2014), 168–175.
- [14] CANTOW, K., ARAKELYAN, K., SEELIGER, E., NIENDORF, T., AND POHLMANN, A. Assessment of Renal Hemodynamics and Oxygenation by Simultaneous Magnetic Resonance Imaging (MRI) and Quantitative Invasive Physiological Measurements. *Kidney Research* 1397 (2016), 129–154.
- [15] COWLEY, A. W., MATTSON, D. L., LU, S., AND ROMAN, R. J. The renal medulla and hypertension. *Hypertension* 25, 4 (1995), 663–673.
- [16] D’AGATI, V., AND SCHMIDT, A. M. RAGE and the pathogenesis of chronic kidney disease. *Nature reviews. Nephrology* 6, 6 (2010), 352–360.
- [17] DE BAZELAIRE, C. M., DUHAMEL, G. D., ROFSKY, N. M., AND ALSOP, D. C. MR imaging relaxation times of abdominal and pelvic tissues measured in vivo at 3.0 T: Preliminary results. *Radiology* 230, 3 (2004), 652–659.
- [18] DOS SANTOS, E. A., LI, L.-P., JI, L., AND PRASAD, P. V. Early changes with diabetes in renal medullary hemodynamics as evaluated by fiberoptic probes and BOLD magnetic resonance imaging. *Investigative radiology* 42, 3 (2007), 157–62.
- [19] DUNN, J. F., AND SWARTZ, H. M. Blood oxygenation. Heterogeneity of hypoxic tissues monitored using bold MR imaging. *Advances in experimental medicine and biology* 428 (1997), 645.
- [20] EBRAHIMI, B., GLOVICZKI, M., WOOLLARD, J. R., CRANE, J. A., TEXTOR, S. C., AND LERMAN, L. O. Compartmental Analysis of Renal BOLD MRI Data. *Investigative Radiology* 47, 3 (2012), 175–182.

- [21] EDLUND, J., HANSELL, P., FASCHING, A., LISS, P., WEIS, J., GLICKSON, J. D., AND PALM, F. Reduced oxygenation in diabetic rat kidneys measured by T2\* weighted magnetic resonance micro-imaging. In *Oxygen Transport to Tissue XXX*. Springer, 2009, pp. 199–204.
- [22] EPSTEIN, F. H., AND PRASAD, P. Effects of furosemide on medullary oxygenation in younger and older subjects. *Kidney international* 57, 5 (may 2000), 2080–3.
- [23] EPSTEIN, F. H., VEVES, A., AND PRASAD, P. V. Effect of Diabetes on Renal Medullary Oxygenation During Water Diuresis. *Diabetes Care* 25, 3 (2002), 575–578.
- [24] ESIPOVA, T. V., KARAGODOV, A., MILLER, J., WILSON, D. F., BUSCH, T. M., AND VINOGRADOV, S. A. Two new "protected" oxyphors for biological oximetry: properties and application in tumor imaging. *Analytical chemistry* 83, 22 (nov 2011), 8756–65.
- [25] FINE, L. G. Renal physiology from earliest times to the Renaissance. *Renal Physiology: People and Ideas*. Bethesda, Am Physiol Soc (1987), 1–30.
- [26] FINE, L. G. A 2000-year history of nephrology: 10 enduring scientific landmarks. *Journal of Nephrology* 26, SUPPL.22 (2013), S6–S17.
- [27] FINE, L. G., BANDYOPADHAY, D., AND NORMAN, J. T. Is there a common mechanism for the progression of different types of renal diseases other than proteinuria? Towards the unifying theme of chronic hypoxia. *Kidney international. Supplement* 75 (apr 2000), S22–6.
- [28] FINE, L. G., AND NORMAN, J. T. Chronic hypoxia as a mechanism of progression of chronic kidney diseases: from hypothesis to novel therapeutics. *Kidney international* 74, 7 (oct 2008), 867–72.
- [29] FINE, L. G., ORPHANIDES, C., AND NORMAN, J. T. Progressive renal disease: the chronic hypoxia hypothesis. *Kidney International* (1998), S74—S78.
- [30] GAING, B., SIGMUND, E. E., HUANG, W. C., BABB, J. S., PARIKH, N. S., STOFFEL, D., AND CHANDARANA, H. Subtype Differentiation of Renal Tumors Using Voxel-Based Histogram Analysis of Intravoxel Incoherent Motion Parameters. *Investigative radiology* (2014).
- [31] GARCIA-SANZ, A., RODRIGUEZ-BARBERO, A., BENTLEY, M. D., RITMAN, E. L., AND ROMERO, J. C. Three-Dimensional Microcomputed Tomography of Renal Vasculature in Rats. *Hypertension* 31, 1 (jan 1998), 440–444.

- [32] GARDENER, A. G., AND FRANCIS, S. T. Multislice perfusion of the kidneys using parallel imaging: Image acquisition and analysis strategies. *Magnetic Resonance in Medicine* 63, 6 (2010), 1627–1636.
- [33] GRANSTAM, S. O., AND GRANSTAM, E. Endothelin-induced changes in blood flow in STZ-diabetic and non-diabetic rats: Relation to nitric oxide synthase and cyclooxygenase inhibition. *Journal of Physiological Sciences* 61, 6 (2011), 497–505.
- [34] GREENWALD, A. G., GONZALEZ, R., HARRIS, R. J., AND GUTHRIE, D. Effect sizes and p-values: What should be reported and what should be replicated? *Psychophysiology* 33 (1996), 175–183.
- [35] HAN, F., XIAO, W., XU, Y., WU, J., WANG, Q., WANG, H., ZHANG, M., AND CHEN, J. The significance of BOLD MRI in differentiation between renal transplant rejection and acute tubular necrosis. *Nephrology Dialysis Transplantation* 23, 8 (2008), 2666–2672.
- [36] HANEDER, S., AUGUSTIN, J., JOST, G., PIETSCH, H., LENGSELD, P., KRÄMER, B. K., SCHOENBERG, S. O., MEYER, M., ATTENBERGER, U. I., AND MICHAELY, H. J. Impact of iso- and low-osmolar iodinated contrast agents on BOLD and diffusion MRI in swine kidneys. *Investigative radiology* 47, 5 (may 2012), 299–305.
- [37] HANSEN, P. B., HASHIMOTO, S., OPPERMAN, M., HUANG, Y., BRIGGS, J. P., AND SCHNERMANN, J. Vasoconstrictor and vasodilator effects of adenosine in the mouse kidney due to preferential activation of A1 or A2 adenosine receptors. *The Journal of pharmacology and experimental therapeutics* 315, 3 (2005), 1150–7.
- [38] HEYMAN, S. N., BREZIS, M., REUBINOFF, C. A., GREENFELD, Z., LECHENE, C., EPSTEIN, F. H., SCOPUS, M., AND HOSPITAL, W. Acute Renal Failure with Selective Medullary Injury in the Rat. *Journal of Clinical Investigation* 82, August (1988), 401–412.
- [39] HEYMAN, S. N., KHAMAI, M., ROSEN, S., AND ROSENBERGER, C. Renal parenchymal hypoxia, hypoxia response and the progression of chronic kidney disease. *American journal of nephrology* 28, 6 (jan 2008), 998–1006.
- [40] HOFMANN, L., SIMON-ZOULA, S., NOWAK, A., GIGER, A., VOCK, P., BOESCH, C., FREY, F. J., AND VOGT, B. BOLD-MRI for the assessment of renal oxygenation in humans: acute effect of nephrotoxic xenobiotics. *Kidney international* 70, 1 (2006), 144–150.

- [41] INOUE, T., KOZAWA, E., OKADA, H., INUKAI, K., WATANABE, S., KIKUTA, T., WATANABE, Y., TAKENAKA, T., KATAYAMA, S., TANAKA, J., AND SUZUKI, H. Noninvasive evaluation of kidney hypoxia and fibrosis using magnetic resonance imaging. *Journal of the American Society of Nephrology : JASN* 22, 8 (aug 2011), 1429–34.
- [42] JENKINSON, M., BANNISTER, P., BRADY, M., AND SMITH, S. Improved Optimization for the Robust and Accurate Linear Registration and Motion Correction of Brain Images. *NeuroImage* 17, 2 (oct 2002), 825–841.
- [43] JOHANNES, T., MIK, E. G., AND INCE, C. Dual-wavelength phosphorimetry for determination of cortical and subcortical microvascular oxygenation in rat kidney. *Journal of applied physiology* 100, 4 (apr 2006), 1301–10.
- [44] JONES, E., OLIPHANT, T., PETERSON, P., AND OTHERS. SciPy: Open source scientific tools for Python.
- [45] JUILLARD, L., LERMAN, L. O., KRUGER, D. G., HAAS, J. A., RUCKER, B. C., POLZIN, J. A., RIEDERER, S. J., AND ROMERO, J. C. Blood oxygen level-dependent measurement of acute intra-renal ischemia. *Kidney international* 65, 3 (2004), 944–950.
- [46] KARGER, N., BIEDERER, J., LÜSSE, S., GRIMM, J., STEFFENS, J., HELLER, M., AND GLÜER, C. Quantitation of renal perfusion using arterial spin labeling with FAIR-UFLARE. *Magnetic resonance imaging* 18, 6 (jul 2000), 641–7.
- [47] LAKOWICZ, J. R., SZMACINSKI, H., NOWACZYK, K., BERNDT, K. W., AND JOHNSON, M. Fluorescence lifetime imaging. *Analytical biochemistry* 202, 2 (1992), 316–30.
- [48] LEE, H. B., AND BLAUFOX, M. D. Blood Volume in the Rat. *J Nucl Med* 25 (1985), 72–76.
- [49] LEE, V. S. Herman Yaggi Carr, PhD (1924-2008): a tribute. *Journal of magnetic resonance imaging : JMRI* 29, 6 (2009), 1243–1247.
- [50] LEE, V. S., KAUR, M., BOKACHEVA, L., CHEN, Q., RUSINEK, H., THAKUR, R., MOSES, D., NAZZARO, C., AND KRAMER, E. L. What causes diminished corticomedullary differentiation in renal insufficiency? *Journal of magnetic resonance imaging : JMRI* 25, 4 (apr 2007), 790–5.
- [51] LEVEY, A. S., AND CORESH, J. Chronic kidney disease. *Lancet* 379, 9811 (jan 2012), 165–80.

- [52] LEVEY, A. S., STEVENS, L. A., SCHMID, C. H., ZHANG, Y. L., III, A. F. C., FELDMAN, H. I., KUSEK, J. W., EGGERS, P., LENTE, F. V., AND GREENE, T. A New Equation to Estimate Glomerular Filtration Rate. *Annals of Internal Medicine* 150 (2009), 604–612.
- [53] LI, L., STOREY, P., KIM, D., LI, W., AND PRASAD, P. Kidneys in hypertensive rats show reduced response to nitric oxide synthase inhibition as evaluated by BOLD MRI. *Journal of Magnetic Resonance Imaging* 17, 6 (2003), 671–675.
- [54] LI, L.-P., FRANKLIN, T., DU, H., PAPADOPOULOU-ROSENZWEIG, M., CARBRAY, J., SOLOMON, R., AND PRASAD, P. V. Intrarenal oxygenation by blood oxygenation level-dependent MRI in contrast nephropathy model: effect of the viscosity and dose. *Journal of magnetic resonance imaging : JMRI* 36, 5 (dec 2012), 1162–7.
- [55] LI, L.-P., HALTER, S., AND PRASAD, P. V. BOLD MRI of the Kidneys. *Magn Reson Imaging Clin N Am.* 16, 4 (2008), 613–viii.
- [56] LI, L.-P., JI, L., SANTOS, E. A., DUNKLE, E., PIERCHALA, L., AND PRASAD, P. Effect of nitric oxide synthase inhibition on intrarenal oxygenation as evaluated by blood oxygenation level-dependent magnetic resonance imaging. *Investigative radiology* 44, 2 (feb 2009), 67–73.
- [57] LI, L.-P., AND PRASAD, P. Evaluation of the Reproducibility of Intrarenal  $R2^*$  and  $\Delta R2^*$  Measurements Following Administration of Furosemide and During Waterload. *Journal of Magnetic Resonance Imaging* 19, 5 (2004), 610–616.
- [58] LI, L.-P., VU, A. T., LI, B. S. Y., DUNKLE, E., AND PRASAD, P. V. Evaluation of intrarenal oxygenation by BOLD MRI at 3.0 T. *Journal of magnetic resonance imaging : JMRI* 20, 5 (nov 2004), 901–4.
- [59] LIN, W., PACZYNSKI, R. P., KUPPUSAMY, K., HSU, C. Y., AND HAACKE, E. M. Quantitative measurements of regional cerebral blood volume using MRI in rats: effects of arterial carbon dioxide tension and mannitol. *Magnetic Resonance in Medicine* 38, 3 (1997), 420–428.
- [60] LIN JI, P., LI, L. P., SCHNITZER, T., DU, H., AND PRASAD, P. V. Intra-renal oxygenation in rat kidneys during water loading: Effects of cyclooxygenase (COX) inhibition and nitric oxide (NO) donation. *Journal of Magnetic Resonance Imaging* 32, 2 (2010), 383–387.

- [61] LISS, P., NYGREN, A., REVSBECH, N. P., AND ULFENDAHL, H. R. Intrarenal oxygen tension measured by a modified clark electrode at normal and low blood pressure and after injection of x-ray contrast media. *Pflugers Archiv European Journal of Physiology* 434, 6 (1997), 705–711.
- [62] LO, L. W., KOCH, C. J., AND WILSON, D. F. Calibration of Oxygen-Dependent Quenching of the Phosphorescence of Pd-meso-tetra (4-Carboxyphenyl) Porphine: A Phosphor with General Application for Measuring Oxygen Concentration in Biological Systems. *Analytical Biochemistry* 236, 1 (1996), 153–160.
- [63] LU, S., AHN, D., JOHNSON, G., LAW, M., ZAGZAG, D., AND GROSSMAN, R. I. Radiology Diffusion-Tensor MR Imaging of Intracranial Neoplasia and Associated Peritumoral Edema : Introduction of the Tumor Infiltration Index. *Neuroradiology* 232, 4 (2004), 221–228.
- [64] LUBBERS, D. W. Oxygen Delivery and Microcirculation in the Brain. *Microcirculation in Circulatory Disorders* (1988), 33–50.
- [65] LUBBERS, D. W., AND BAUMGARTL, H. Heterogeneities and profiles of oxygen pressure in brain and kidney as examples of the PO<sub>2</sub> distribution in the living tissue. *Kidney international* 51 (1997), 372–380.
- [66] MARCKMANN, P. Nephrogenic Systemic Fibrosis: Suspected Causative Role of Gadodiamide Used for Contrast-Enhanced Magnetic Resonance Imaging. *Journal of the American Society of Nephrology* 17, 9 (2006), 2359–2362.
- [67] MARTIROSIAN, P., KLOSE, U., MADER, I., AND SCHICK, F. FAIR true-FISP perfusion imaging of the kidneys. *Magnetic resonance in medicine : official journal of the Society of Magnetic Resonance in Medicine / Society of Magnetic Resonance in Medicine* 51, 2 (feb 2004), 353–61.
- [68] MICHAELY, H. J., METZGER, L., HANEDER, S., HANSMANN, J., SCHOENBERG, S. O., AND ATTENBERGER, U. I. Renal BOLD-MRI does not reflect renal function in chronic kidney disease. *Kidney international* 81, 7 (apr 2012), 684–9.
- [69] MIK, E. G., JOHANNES, T., ZUURBIER, C. J., HEINEN, A., HOUBEN-WEERTS, J. H. P. M., BALESTRA, G. M., STAP, J., BEEK, J. F., AND INCE, C. In vivo mitochondrial oxygen tension measured by a delayed fluorescence lifetime technique. *Biophysical journal* 95, 8 (2008), 3977–3990.
- [70] NANGAKU, M. Chronic hypoxia and tubulointerstitial injury: a final common pathway to end-stage renal failure. *Journal of the American Society of Nephrology : JASN* 17, 1 (jan 2006), 17–25.

- [71] NEUGARTEN, J. Renal BOLD-MRI and assessment for renal hypoxia. *Kidney international* 81, 7 (apr 2012), 613–4.
- [72] O’CONNOR, P. M. Renal oxygen delivery: matching delivery to metabolic demand. *Clinical and experimental pharmacology & physiology* 33, 10 (oct 2006), 961–7.
- [73] ORDIDGE, R. J., WYLEZINSKA, M., HUGG, J. W., BUTTERWORTH, E., AND FRANCONI, F. Frequency offset corrected inversion (FOCI) pulses for use in localized spectroscopy. *Magnetic resonance in medicine : official journal of the Society of Magnetic Resonance in Medicine / Society of Magnetic Resonance in Medicine* 36, 4 (1996), 562–566.
- [74] PALLONE, T. L., ZHANG, Z., AND RHINEHART, K. Physiology of the renal medullary microcirculation. *American journal of physiology. Renal physiology* 284, 2 (2003), F253–F266.
- [75] PAPPENHEIMER, J. R., AND KINTER, W. B. Hematocrit Ratio of Blood Within Mammalian Kidney and Its Significance for Renal Hemodynamics. *Am J Physiol – Legacy Content* 185, 2 (1956), 377–390.
- [76] PEDERSEN, M., DISSING, T. H., MORKENBORG, J., STØDKILDE-JØRGENSEN, H., HANSEN, L. H., PEDERSEN, L. B., GRENIER, N., AND FRØKJER, J. Validation of quantitative BOLD MRI measurements in kidney: Application to unilateral ureteral obstruction. *Kidney International* 67, 6 (2005), 2305–2312.
- [77] PISKUNOWICZ, M., HOFMANN, L., ZUERCHER, E., BASSI, I., MILANI, B., STUBER, M., NARKIEWICZ, K., VOGT, B., BURNIER, M., AND PRUIJM, M. A new technique with high reproducibility to estimate renal oxygenation using BOLD-MRI in chronic kidney disease. *Magnetic Resonance Imaging* 33, 3 (2015), 253–261.
- [78] PONTO, L. L. B., AND SCHOENWALD, R. D. Furosemide (Frusemide) A Pharmacokinetic/Pharmacodynamic Review (Part I). *Clinical pharmacokinetics* 18, 5 (1990), 381–408.
- [79] PRASAD, P. V., CHEN, Q., EPSTEIN, F. H., AND EDELMAN, R. R. Breath-Hold R2\* Mapping with a Multiple Gradient-Recalled Echo Sequence: Application to the Evaluation of Intrarenal Oxygenation. *Journal of Magnetic Resonance Imaging* 7 (1997), 1163–1165.
- [80] PRASAD, P. V., EDELMAN, R. R., AND EPSTEIN, F. H. Noninvasive evaluation of intrarenal oxygenation with BOLD MRI. *Circulation* 94, 12 (1996), 3271–3275.

- [81] PRIATNA, A., EPSTEIN, F. H., SPOKES, K., AND PRASAD, P. V. Evaluation of Changes in Intrarenal Oxygenation in Rats Using Multiple Gradient-Recalled Echo (mGRE) Sequence. *Journal of Magnetic Resonance Imaging* 9 (1999), 842–846.
- [82] PRUIJM, M., HOFMANN, L., MAILLARD, M., TREMBLAY, S., GLATZ, N., WUERZNER, G., BURNIER, M., AND VOGT, B. Effect of sodium loading/depletion on renal oxygenation in young normotensive and hypertensive men. *Hypertension* 55, 5 (2010), 1116–1122.
- [83] PRUIJM, M., HOFMANN, L., PISKUNOWICZ, M., MULLER, M.-E., ZWEIACKER, C., BASSI, I., VOGT, B., STUBER, M., AND BURNIER, M. Determinants of renal tissue oxygenation as measured with BOLD-MRI in chronic kidney disease and hypertension in humans. *PloS one* 9, 4 (jan 2014), e95895.
- [84] RAJENDRAN, R., LEW, S. K., YONG, C. X., TAN, J., WANG, D. J. J., AND CHUANG, K. H. Quantitative mouse renal perfusion using arterial spin labeling. *NMR in Biomedicine* 26, 10 (2013), 1225–1232.
- [85] RICKSTEN, S.-E., BRAGADOTTIR, G., AND REDFORS, B. Renal oxygenation in clinical acute kidney injury. *Critical care (London, England)* 17, 2 (mar 2013), 221.
- [86] RITT, M., JANKA, R., SCHNEIDER, M. P., MARTIROSIAN, P., HORNEGGER, J., BAUTZ, W., UDER, M., AND SCHMIEDER, R. E. Measurement of kidney perfusion by magnetic resonance imaging: Comparison of MRI with arterial spin labeling to para-aminohippuric acid plasma clearance in male subjects with metabolic syndrome. *Nephrology Dialysis Transplantation* 25, 4 (2010), 1126–1133.
- [87] ROSSI, C., ARTUNC, F., MARTIROSIAN, P., SCHLEMMER, H.-P., SCHICK, F., AND BOSS, A. Histogram analysis of renal arterial spin labeling perfusion data reveals differences between volunteers and patients with mild chronic kidney disease. *Investigative radiology* 47, 8 (aug 2012), 490–6.
- [88] SAAD, A., AND CRANE, J. Human Renovascular Disease : Estimating Fractional Tissue Hypoxia to Analyze Blood Oxygen Level dependent MR. *Radiology* 268, 3 (2013).
- [89] SHAHIDI, M., SHAKOOR, A., BLAIR, N. P., MORI, M., AND SHONAT, R. D. A method for chorioretinal oxygen tension measurement. *Current eye research* 31, 4 (2006), 357–366.
- [90] SHAHIDI, M., WANER, J., BLAIR, N. P., LITTLE, D. M., AND WU, T. Retinal tissue oxygen tension imaging in the rat. *Investigative ophthalmology & visual science* 51, 9 (2010), 4766–4770.

- [91] SONG, R., LOEFFLER, R. B., AND HILLENBRAND, C. M. Improved renal perfusion measurement with a dual navigator-gated Q2TIPS fair technique. *Magnetic Resonance in Medicine* 64, 5 (2010), 1352–1359.
- [92] STABLES, L. A., KENNAN, R. P., AND GORE, J. C. Asymmetric Spin-Echo Imaging of Magnetically Inhomogeneous Systems: Theory, Experiment, and Numerical Studies. *Magnetic resonance in medicine* 40 (1998), 432–442.
- [93] STOREY, P., JI, L., LI, L.-P., AND PRASAD, P. V. Sensitivity of USPIO-enhanced R2 imaging to dynamic blood volume changes in the rat kidney. *Journal of magnetic resonance imaging : JMRI* 33, 5 (may 2011), 1091–9.
- [94] SULLIVAN, G. M., AND FEINN, R. Using Effect Size-or Why the P Value Is Not Enough. *Journal of graduate medical education* 4, 3 (sep 2012), 279–82.
- [95] TAN, H., KOKTZOGLU, I., AND PRASAD, P. V. Renal perfusion imaging with two-dimensional navigator gated arterial spin labeling. *Magnetic resonance in medicine : official journal of the Society of Magnetic Resonance in Medicine / Society of Magnetic Resonance in Medicine* 000 (feb 2013), 1–10.
- [96] TAN, H., MALDJIAN, J. A., POLLOCK, J. M., BURDETTE, J. H., YANG, L. Y., DEIBLER, A. R., AND KRAFT, R. A. A Fast, Effective Filtering Method for Improving Clinical Pulsed Arterial Spin Labeling MRI. *Journal of Magnetic Resonance Imaging* 29, 5 (2009), 1134–1139.
- [97] THACKER, J. M., LI, L.-P., LI, W., ZHOU, Y., AND PRASAD, P. V. Renal Blood Oxygenation Level-Dependent Magnetic Resonance Imaging: A Sensitive and Objective Analysis. *Investigative Radiology* 50, 12 (2015), 821–827.
- [98] TUMKUR, S., VU, A., LI, L., AND PRASAD, P. V. Evaluation of Intrarenal Oxygenation at 3 . 0 T Using. *Investigative radiology* 41, 2 (2006), 181–184.
- [99] VALSASINA, P., ROCCA, M. A., AGOSTA, F., BENEDETTI, B., HORSFIELD, M. A., GALLO, A., ROVARIS, M., COMI, G., AND FILIPPI, M. Mean diffusivity and fractional anisotropy histogram analysis of the cervical cord in MS patients. *NeuroImage* 26, 3 (jul 2005), 822–8.
- [100] VIVIER, P.-H., STOREY, P., CHANDARANA, H., YAMAMOTO, A., TANTILLO, K., KHAN, U., ZHANG, J. L., SIGMUND, E. E., RUSINEK, H., BABB, J. S., BUBENHEIM, M., AND LEE, V. S. Renal Blood Oxygenation Level-Dependent Imaging: Contribution of R2 to R2\* Values. *Investigative Radiology* 48, 7 (2013), 1–8.

- [101] WANG, J.-J., HENDRICH, K. S., JACKSON, E. K., ILDSTAD, S. T., WILLIAMS, D. S., AND HO, C. Perfusion quantitation in transplanted rat kidney by MRI with arterial spin labeling. *Kidney international* 53, 6 (1998), 1783–1791.
- [102] WANG, Y. X., POON, C. I., AND PANG, C. C. Vascular pharmacodynamics of NG-nitro-L-arginine methyl ester in vitro and in vivo. *The Journal of pharmacology and experimental therapeutics* 267, 3 (1993), 1091–1099.
- [103] WARNER, L., GLOCKNER, J. F., WOOLLARD, J., TEXTOR, S. C., ROMERO, J. C., AND LERMAN, L. O. Determinations of renal cortical and medullary oxygenation using blood oxygen level-dependent magnetic resonance imaging and selective diuretics. *Investigative radiology* 46, 1 (2011), 41–7.
- [104] WILSON, D. F., LEE, W. M. F., MAKONNEN, S., FINIKOVA, O., APRELEVA, S., AND VINOGRADOV, S. A. Oxygen pressures in the interstitial space and their relationship to those in the blood plasma in resting skeletal muscle. *Journal of applied physiology (Bethesda, Md. : 1985)* 101, August 2006 (2006), 1648–1656.
- [105] XIN-LONG, P., JING-XIA, X., JIAN-YU, L., SONG, W., AND XIN-KUI, T. A preliminary study of blood-oxygen-level-dependent MRI in patients with chronic kidney disease. *Magnetic resonance imaging* 30, 3 (apr 2012), 330–5.
- [106] YABLONSKIY, D. A., AND HAACKE, E. M. Theory of NMR Signal Behavior in Magnetically Inhomogeneous Tissues : The Static Dephasing Regime. *Magnetic resonance in medicine* 32 (1994), 749–763.
- [107] YANG, X., CAO, J., WANG, X., LI, X., XU, Y., AND JIANG, X. Evaluation of renal oxygenation in rat by using R2' at 3-T magnetic resonance: initial observation. *Academic radiology* 15, 7 (jul 2008), 912–8.
- [108] YIN, W.-J., LIU, F., LI, X.-M., YANG, L., ZHAO, S., HUANG, Z.-X., HUANG, Y.-Q., AND LIU, R.-B. Noninvasive evaluation of renal oxygenation in diabetic nephropathy by BOLD-MRI. *European journal of radiology* 81, 7 (jul 2012), 1426–31.
- [109] ZHANG, J. L., MORRELL, G., RUSINEK, H., SIGMUND, E. E., CHANDARANA, H., LERMAN, L. O., PRASAD, P. V., NILES, D., ARTZ, N., FAIN, S., AND OTHERS. New magnetic resonance imaging methods in nephrology. *Kidney international* 85, 4 (2014), 768–778.
- [110] ZHANG, J. L., MORRELL, G., RUSINEK, H., WARNER, L., VIVIER, P.-H., CHEUNG, A. K., LERMAN, L. O., AND LEE, V. S. Measurement of renal tissue

- oxygenation with blood oxygen level-dependent MRI and oxygen transit modeling. *American journal of physiology. Renal physiology* 306, 6 (mar 2014), F579–87.
- [111] ZHANG, J. L., MORRELL, G. R., AND LEE, V. S. Blood oxygen level-dependent MR in renal disease: moving toward clinical utility. *Radiology* 268, 3 (sep 2013), 619–21.
- [112] ZHANG, J. L., RUSINEK, H., CHANDARANA, H., AND LEE, V. S. Functional MRI of the kidneys. *Journal of magnetic resonance imaging : JMRI* 37, 2 (mar 2013), 282–93.
- [113] ZHANG, X., ZHANG, Y., YANG, X., WANG, X., AN, H., ZHANG, J., AND FANG, J. Feasibility of noninvasive quantitative measurements of intrarenal  $R_2'$  in humans using an asymmetric spin echo echo planar imaging sequence. *NMR in biomedicine*, December 2011 (jun 2012).
- [114] ZIMMER, F., ZÖLLNER, F. G., HOEGER, S., KLOTZ, S., TSAGOGIORGAS, C., KRÄMER, B. K., AND SCHAD, L. R. Quantitative Renal Perfusion Measurements in a Rat Model of Acute Kidney Injury at 3T: Testing Inter- and Intramethodical Significance of ASL and DCE-MRI. *PLoS ONE* 8, 1 (2013).
- [115] ZIMMERHACKL, B., ROBERTSON, C. R., AND JAMISON, R. L. The microcirculation of the renal medulla. *Circulation Research* 57, 5 (nov 1985), 657–667.